

THESIS

THE SPATIAL SCALE OF CONVECTIVE AGGREGATION  
IN CLOUD RESOLVING SIMULATIONS  
OF RADIATIVE-CONVECTIVE EQUILIBRIUM

Submitted by

Casey Patrizio

Department of Atmospheric Science

In partial fulfillment of the requirements

For the Degree of Master of Science

Colorado State University

Fort Collins, Colorado

Summer 2017

Master's Committee:

Advisor: David Randall

Co-Advisor: David Thompson

Allan Kirkpatrick

Copyright by Casey Patrizio 2017

All Rights Reserved

## ABSTRACT

# THE SPATIAL SCALE OF CONVECTIVE AGGREGATION IN CLOUD RESOLVING SIMULATIONS OF RADIATIVE-CONVECTIVE EQUILIBRIUM

A three-dimensional cloud-resolving model (CRM) was used to investigate the preferred separation distance between humid, rainy regions formed by convective aggregation in radiative-convective equilibrium without rotation. We performed the simulations with doubly-periodic square domains of widths 768 km, 1536 km and 3072 km over a time period of about 200 days. The simulations in the larger domains were initialized using multiple copies of the results in the small domain at day 90, plus a small perturbation. With all three domain sizes, the simulations evolved to a single statistically steady convective cluster surrounded by a broader region of dry, subsiding air by about day 150. In the largest domain case, however, we found that an additional convective cluster formed when the simulation was run for an extended period of time. Specifically, a smaller convective cluster formed at around day 185 at a maximum radial distance from the larger cluster and then re-merged with the larger cluster after about 10 days.

We explored how the aggregated state was different in each domain case, before the smaller cluster formed in the large domain. In particular, we investigated changes in the radial structure of the aggregated state by calculating profiles for the water, dynamics and radiation as a function of distance from the center of the convective region. Changes in the vertical structure were also investigated by compositing on the convective region and dry, subsiding region at each height. We found that, with increasing domain size, the convective

region boundary layer became more buoyant, the convective cores reached deeper into the troposphere, the mesoscale convective updraft became weaker, and the mesoscale convective region spread out. Additionally, as the domain size was increased, conditions in the remote environment became favorable for convection. We describe a physical mechanism for the weakening of the mesoscale convective updraft and associated broadening of the convective region with increasing domain size, which involves mid-level stable layer enhancement as a result of the deeper convection.

Finally, a simple analytical model of the aggregated state was used to explore the dependency of the convective fractional area on the domain size. The simple model solutions that had net radiative cooling and surface evaporation in the convective region were consistent with the simulation results. In particular, the solutions captured the broadening of the convective region, the weakening of the convective region updraft, as well as the positive and declining gross moist stability (GMS) that occurred with increasing domain size in the simulations. Furthermore, the simple model transitioned from positive to negative GMS at a domain length of about 7000 km because the convective region boundary layer became progressively more humid with increasing domain size. This suggests that the spatial scale of the aggregated RCE state in the simulations would be limited to a length scale of about 7000 km, as convectively-active areas are commonly observed to have positive GMS. This work additionally suggests that the processes that influence the water vapor content in the convective region boundary layer, such as convectively-driven turbulent water vapor fluxes, are important for determining the spatial scale of the aggregated RCE state.

## ACKNOWLEDGEMENTS

I would like to thank my advisor, Dave R., and co-advisor, Dave T., for their continual support, guidance and insight throughout my education at Colorado State University and throughout the preparation of this thesis. I would like to thank Allan Kirkpatrick for his willingness to serve on my committee as an outside member on such short notice. I would also like to thank Don Dazlich for providing code that is used in the initialization of the large domain simulation runs. Finally, I would like to thank my mom, Michelle, for her support throughout the years, my friends, for keeping me grounded, and my partner, Rachel, who has inspired me in so many ways.

This work has been supported by the National Science Foundation Science and Technology Center for Multi-Scale Modeling of Atmospheric Processes, managed by Colorado State University under cooperative agreement No. ATM-0425247, by the National Aeronautics and Space Administration under Grant No. NNX13AQ04G, and by the National Science Foundation under Grant No. AGS-1547003. I would also like to acknowledge high-performance computing support from Cheyenne (doi:10.5065 /D6RX99HX) provided by NCAR's Computational and Information Systems Laboratory, sponsored by the National Science Foundation.

## TABLE OF CONTENTS

|   |      |
|---|------|
| ABSTRACT.....   | iii  |
| ACKNOWLEDGEMENTS.....   | iv   |
| LIST OF TABLES.....   | viii |
| LIST OF FIGURES.....  | ix   |
| 1. Introduction.....  | 1    |
| 1.1. Radiative-Convective Equilibrium.....                            | 1    |
| 1.2. Convective Aggregation.....                                      | 4    |
| 1.3. Multiple Equilibria of Radiative-Convective Equilibrium.....     | 7    |
| 1.4. Organized Convection in More Realistic Atmospheres.....          | 8    |
| 1.4.1. Observations of Organized Convection.....                      | 9    |
| 1.4.2. Organized Convection in More Realistic Simulations of RCE..... | 12   |
| 1.4.3. Convective Aggregation in Observations.....                    | 14   |
| 1.5. Convective Aggregation Mechanisms.....                           | 16   |
| 1.6. Effects of Organized Convection.....                             | 20   |
| 1.7. Convective Aggregation Domain Size Dependency.....               | 22   |
| 1.8. Objective of Thesis.....   | 26   |
| 2. Methods.....   | 28   |
| 2.1. Simulation set-up.....   | 28   |
| 3. Evolution to Steady-State.....                                     | 31   |
| 3.1. Convective Merging.....  | 35   |
| 4. Radial Profiles.....   | 47   |

|        |   |     |
|--------|---|-----|
| 4.1.   | Time Averaging Methodology .....                        | 47  |
| 4.2.   | Clouds & Water Vapor .....                              | 48  |
| 4.3.   | Circulation .....                                       | 53  |
| 4.4.   | Stability & Buoyancy .....                              | 56  |
| 4.5.   | Vertical Velocity .....                                 | 64  |
| 5.     | Convective Region and Subsiding Region Composites ..... | 70  |
| 5.1.   | Compositing Methodology .....                           | 70  |
| 5.2.   | Convective Fractional Area .....                        | 72  |
| 5.3.   | Convective Region Composites .....                      | 74  |
| 5.4.   | Convection-Free Region Composites .....                 | 81  |
| 6.     | Summary of Domain Size Dependencies .....               | 88  |
| 6.1.   | Size of Convective Region .....                         | 88  |
| 6.2.   | Convective Region and Dry Region Statistics .....       | 89  |
| 7.     | Discussion & Interpretations .....                      | 91  |
| 7.1.   | Discussion of the Simulation Results .....              | 91  |
| 7.2.   | Simple Model of the Aggregated RCE State .....          | 96  |
| 7.2.1. | Description .....                                       | 96  |
| 7.2.2. | Equations .....   | 99  |
| 7.2.3. | Analysis .....  | 120 |
| 7.2.4. | Solutions .....   | 128 |
| 8.     | Conclusions & Future Direction .....                    | 157 |
| 8.1.   | Comparing the Simple Model to the Simulations .....     | 157 |
| 8.1.1. | Spatial Scale of Aggregated RCE .....                   | 157 |

|  |     |
|--|-----|
| 8.1.2. Vertical Structure .....              | 159 |
| 8.1.3. Understanding $\Delta h_{trop}$ ..... | 160 |
| 8.1.4. Sensitivity to SST .....              | 162 |
| 8.2. Comparison To GCMs .....                | 163 |
| 8.3. Oscillation of Aggregated RCE .....     | 164 |
| 9. References .....                          | 165 |
| 10. Appendix .....                           | 175 |

LIST OF TABLES

|     |   |     |
|-----|---|-----|
| 6.1 | Convective Region Size .....  | 89  |
| 6.2 | Convective Region and Dry Region Vertical Velocity, Stability, & Buoyancy<br>Statistics ..... | 89  |
| 7.1 | Coupled Simple Model Equations .....  | 119 |
| 7.2 | Uncoupled Simple Model Equations .....  | 119 |
| 7.3 | Simple Model Prescribed Variables .....   | 129 |
| 7.4 | Dry and Moist Static Energy in Simulated Convective Region .....                              | 152 |

## LIST OF FIGURES

|      |   |    |
|------|---|----|
| 1.1  | Example of Convective Aggregation from Wing & Emanuel (2013) .....  | 6  |
| 1.2  | Examples of Global-Scale Convective Aggregation) .....  | 24 |
| 3.1  | Time series of domain-mean precipitable water .....   | 32 |
| 3.2  | Hourly maps of PW during convective merging .....   | 33 |
| 3.3  | Maps of PW at end of simulation, re-mapped onto the large domain grid .....   | 33 |
| 3.4  | Time-height cross section of horizontal mean water vapor mixing ratio, $q_v$ and<br>relative humidity, RH .....       | 35 |
| 3.5  | Time-height cross section of horizontal mean $q_v(z, t) - q_v(z, t = \text{day } 90)$ .....                           | 36 |
| 3.6  | Hourly maps of cloud top height (km) for 3072 x 3072 km domain case, day 180<br>to 220 .....                          | 37 |
| 3.7  | 200 hPa and surface wind field maps during convective merging .....   | 38 |
| 3.8  | Surface wind speed maps during convective merging .....   | 39 |
| 3.9  | Schematic of surface wind radial velocity during convective merging .....   | 40 |
| 3.10 | Time series of the domain mean FMSE variance during convective merging and<br>the aggregated state .....              | 43 |
| 3.11 | Time series of the domain mean FMSE variance budget terms during convective<br>merging and the aggregated state. .... | 44 |
| 4.1  | Radial profiles ( $z-\hat{r}$ ) of non-precipitating condensate, $q_n$ .....  | 48 |
| 4.2  | Temperature profiles .....  | 49 |
| 4.3  | Radial profiles of precipitation, P, and evaporation, E. ....   | 50 |

|      |  |    |
|------|--|----|
| 4.4  | Cloud fraction profiles .....  | 51 |
| 4.5  | Radial profiles ( $z-\hat{r}$ ) of relative humidity, RH.....  | 51 |
| 4.6  | Radial profiles of precipitable water, PW.....   | 52 |
| 4.7  | Radial profiles ( $z-\hat{r}$ ) of the streamfunction, $\psi$ , and water vapor mixing ratio, $q_v$ ...                        | 54 |
| 4.8  | Radial profiles ( $z-\hat{r}$ ) of the radial velocity $u_r$ .....   | 55 |
| 4.9  | Johnson cloud schematic.....   | 57 |
| 4.10 | Radial profiles ( $z-\hat{r}$ ) of the buoyancy frequency, $N^2$ .....   | 57 |
| 4.11 | Time-height cross section of the radiative heating rate, $Q_r$ and the stability, $\frac{\partial s}{\partial z}$ ...          | 59 |
| 4.12 | Radial profiles ( $z-\hat{r}$ ) of the buoyancy .....  | 61 |
| 4.13 | Radial profiles ( $z-\hat{r}$ ) of the buoyancy flux.....  | 63 |
| 4.14 | Time series of domain-mean buoyancy flux.....  | 63 |
| 4.15 | Radial profiles ( $z-\hat{r}$ ) of the tropospheric mean buoyancy .....  | 64 |
| 4.16 | Radial profiles ( $z-\hat{r}$ ) of the vertical velocity $w$ .....   | 65 |
| 4.17 | Radial profiles ( $z-\hat{r}$ ) of the horizontal temperature anomaly $T - \bar{T}$ .....                                      | 66 |
| 4.18 | Radial profiles ( $z-\hat{r}$ ) of the $-w\frac{\partial s}{\partial z} + Q_r$ .....   | 66 |
| 4.19 | Radial profiles ( $z-\hat{r}$ ) of the radiative heating rate, $Q_r$ .....   | 67 |
| 4.20 | Radial profiles of tropospheric averaged $w$ .....   | 68 |
| 5.1  | Maps of precipitable water, $w$ at 500 hPa, and precipitation for the small domain case, with and without block averaging..... | 72 |
| 5.2  | Relative humidity binned by time-averaged vertical velocity .....  | 73 |
| 5.3  | Vertical profiles of the convective fractional area, with and without block averaging.   | 73 |

|      |  |     |
|------|--|-----|
| 5.4  | Vertical profiles of vertical velocity composited on the convection region. ....   | 75  |
| 5.5  | Frequency distribution of time-averaged vertical velocity .....  | 75  |
| 5.6  | Frequency distribution of daily-average 500 hPa vertical velocity .....  | 76  |
| 5.7  | Vertical profiles of the buoyancy frequency, $N^2$ , composited on the convection<br>region and convection-free region. ....     | 77  |
| 5.8  | Vertical profiles of the horizontal mass flux out of the convective region. ....   | 78  |
| 5.9  | Time series of maximum cloud top height .....  | 79  |
| 5.10 | Time series of vertically-integrated precipitating condensate .....  | 80  |
| 5.11 | Time series of surface precipitation, $P$ .....  | 81  |
| 5.12 | Time series of high cloud fraction .....   | 82  |
| 5.13 | Vertical profiles of vertical velocity composited on the convection-free region. ....  | 83  |
| 5.14 | Vertical profiles of the sum of adiabatic warming and radiative cooling composited<br>on the convection-free region. ....        | 83  |
| 5.15 | Vertical profiles of the radiative heating rate, $Q_r$ , composited on the convection<br>region and convection-free region. .... | 85  |
| 5.16 | Vertical profiles of the relative humidity, $RH$ , composited on the convection region<br>and convection-free region. ....       | 86  |
| 7.1  | Geometry of the simple model .....   | 98  |
| 7.2  | Variables of the simple model .....  | 100 |
| 7.3  | The convective fractional area of the simple model, $\sigma$ , plotted in $\alpha$ - $RH_c$ space ....                           | 125 |
| 7.4  | Prescribed temperature profile for simple model .....  | 130 |
| 7.5  | Solutions of the simple model, $\hat{Q}_c < 0$ .....   | 132 |

|      |  |     |
|------|--|-----|
| 7.6  | Solutions of the simple model, $\hat{Q}_c > 0$ .....   | 134 |
| 7.7  | $RH_c$ for large scale simple model solutions.....   | 136 |
| 7.8  | Solutions of the simple model, varying $\hat{Q}_c < 0$ .....   | 140 |
| 7.9  | Solutions of the simple model, varying $\hat{Q}_c > 0$ .....   | 141 |
| 7.10 | $\Delta h_{trop}$ for the simple model solutions.....  | 143 |
| 7.11 | Radial profiles of the sum of net radiative heating, surface latent heat flux, and<br>sensible heat flux $Q_{r,net} + LHF + SHF$ ..... | 144 |
| 7.12 | Physical solutions of the simple model.....  | 146 |
| 7.13 | Radial profiles of the sum of net radiative heating and surface latent heat flux<br>$Q_{r,net} + LHF$ .....                            | 147 |
| 7.14 | Radial profiles of the surface latent sensible flux $SHF$ .....  | 148 |
| 7.15 | $l_d - l_c$ for the simple model solutions, varying $\alpha$ .....   | 150 |
| 7.16 | Vertical profiles of MSE in the convective region from simulations.....  | 151 |
| 7.17 | Solutions of the simple model for $\hat{Q}_c > 0$ and $\hat{Q}_c < 0$ .....  | 153 |

## 1. INTRODUCTION

### 1.1. RADIATIVE-CONVECTIVE EQUILIBRIUM

Radiative-convective equilibrium (RCE) is a simplified equilibrium state of the atmosphere in which there is a balance between energy input by uniform incoming solar radiation and energy output by longwave radiative emission, while energy is transported vertically by convection. An equilibrium state of the atmosphere simply means that atmospheric variables (e.g. temperature, water vapor, pressure) are not changing with time. It is natural for atmospheric scientists to attempt to model such a state because the globally averaged time-mean temperature profile of the atmosphere is unchanging over long time periods. It is important to note that RCE is not a realistic equilibrium model in the sense that it does not account for energy transport by large-scale circulations (e.g. the Hadley Cell), as well as the non-uniformity of incoming solar radiation, both of which are highly important properties of the real atmosphere. However, atmospheric scientists have studied RCE in an attempt to unravel the complexities of the atmosphere because RCE is conceptually simple, yet can yield a temperature profile that is consistent with observations (Manabe & Wetherald, 1967; Stone & Carlson, 1979). The details of some early studies of the atmosphere in equilibrium will be discussed in the following.

An even more idealized model of the equilibrium state of the atmosphere is pure radiative equilibrium, in which energy input to the atmosphere (solar radiation) is equal to energy output by the atmosphere (longwave radiation), without accounting for fluid-dynamical energy transport within the system. However, an early seminal study of pure radiative equilibrium by Manabe & Strickler (1964) found that, without considering the effects of convection, the resulting equilibrium temperature profile would never occur in nature in the long-term

mean sense because it was unstable. An unstable temperature profile refers to a situation in which the environmental lapse rate (rate of decrease of the temperature with height) is greater than the lapse rate a moist parcel of air would experience as it ascends adiabatically in the atmosphere. This lapse rate is referred to as the moist adiabatic lapse rate. In other words, when the temperature profile is unstable, parcels of air are positively buoyant with respect to their surroundings. In the real atmosphere, under unstable conditions, parcels of air will rise due to their positive buoyancy, while transporting energy and water in the process. The convection persists until enough energy has been transported such that the parcel of air becomes neutrally buoyant (i.e. the environment lapse rate is equal to moist adiabatic lapse rate). In other words, the temperature profile corresponding to pure radiative equilibrium can not be an equilibrium state of the real atmosphere because convection would actively adjust the temperature profile to a neutral state. These studies were among the first which showed that the vertical transport of energy via convection is an important piece of the equilibrium state of the real atmosphere.

In early studies of RCE, the state of a single column of the atmosphere was simulated with parameterized convection (Manabe & Strickler, 1964; Manabe & Wetherald; 1967, Schneider, 1972). Parameterized convection means that the convection is calculated by a series of equations and not simulated with the coupled equations of motion. This makes the calculation of convection much less computationally expensive, hence the ubiquity of parameterizations in early studies of the atmosphere. In these studies, the convective flux was typically calculated as the flux of energy required to reduce instability in the temperature profile, without accounting for the direct vertical transport of moisture. For example, the seminal study of RCE by Manabe & Strickler (1964) used a simple convective adjustment

parameterization in which the convective flux was given by the flux of energy required to adjust the temperature profile to neutral, moist adiabatic conditions. Additionally, the water vapor profile was often calculated by fixing the absolute humidity or relative humidity to a climatological mean (e.g. Manabe & Wetherald (1967)). In fixing the relative humidity profile, convection could only change the absolute humidity indirectly by changing the temperature. Overall, a fixed relative humidity profile resulted in a more realistic temperature profile as compared to a fixed absolute humidity profile, which showed that the transport of water vapor by convection has important radiative effects in the real atmosphere. This highlights the importance of accounting for vertical transport of moisture by convection, but it is important to note that convection does not always transport moisture in such a way to conserve relative humidity in the real atmosphere. Additionally, in these single-column studies of RCE, the convective flux was thought of as being horizontally uniform, or similarly, that the mean convective flux in the domain is simply proportional to the sum of the individual convective plume fluxes. In reality, convective plumes interact with their environment in ways that can feedback onto the convection itself. In the following, we describe one such feedback which would have important effects on the RCE state.

To illustrate an example of the type of feedback that would not be present in the previously discussed single-column models of RCE, consider the effect of a single convective plume on the atmospheric column in a more realistic three-dimensional simulation of the atmosphere. In particular, consider a simulation in which convection transports both energy and moisture directly and the convection is not completely horizontally uniform throughout the model domain. In this case, the convective plume would be associated with a tendency

to moisten the column, which would reduce outgoing long-wave radiation (OLR) in the column (as water vapor is a strong absorber of infrared radiation). This would tend to have a heating effect in the column, and could potentially drive further convection in the column through an increase in column buoyancy. This would be an example of a positive feedback on convection because the presence of convection led to changes to the environment that favored additional convection. Considering the domain-mean effect of such an interaction, one might imagine that if the OLR is decreased in one column it should be increased in another column in order to maintain the state of radiative equilibrium at the top of the atmosphere. An increase in OLR in a column could be accomplished via drying of the column (driven by compensating subsidence), or an increase in sea-surface temperature (driven by horizontal energy transport in the ocean). Thus, it is important to realize that these feedbacks can not only have local effects on convection, but can also have effects on the remote environment. It is also important to note that in a more realistic model of RCE, both negative and positive feedbacks are occurring simultaneously. Therefore, considering the net effect of all feedbacks at any moment in time is a complex problem and provides motivation for more realistic simulations of RCE, which utilize two or three spatial dimensions and/or explicitly resolved convection (i.e. calculation of convection without parameterization).

## 1.2. CONVECTIVE AGGREGATION

To this end, studies of RCE in which moist convection is simulated more realistically in a two or three-dimensional domain, have shown that convection will transition from a state of homogeneity to a state of heterogeneity under certain conditions. In other words, convection is initially spread out with respect to the model domain, and then becomes

clustered as time progresses. This phenomenon is referred to as *convective aggregation* in the literature. It is important to note that although convection is simulated more realistically in these studies, the conditions imposed in these simulations are not necessarily realistic, and often include no large-scale forcing, no rotation, uniform incoming solar radiation, and uniform sea-surface temperature (SST). Note that a large-scale forcing refers to any weather phenomenon that exists at scales larger than the simulated domain, and hence must be prescribed. Therefore, the simulated atmosphere in these experiments should be thought of as an idealized representation of the atmosphere. It should be noted, however, that these conditions are not altogether unreasonable in certain geographic locations. In particular, the conditions used in these simulations are most consistent with atmospheric conditions near the equator (e.g. west Pacific warm pool), where the Coriolis force and large scale forcing are both weak, and SSTs and incoming solar radiation are both relatively uniform.

Convective aggregation was first reported by Held et al. (1993) in 2D cloud-resolving model (CRM) simulations of RCE with explicitly resolved convection, wherein convection was randomly distributed throughout the domain initially but then became localized to a distinct region of the domain over a period of about 25 days. A cloud-resolving model refers to a model with sufficiently fine horizontal grid spacing (usually  $< 3$  km) such that individual convective cores are resolved by the model. In this case, the convective fluxes are directly calculated by the governing moisture and momentum equations, without parameterization. Convective aggregation has also been reported in 3D CRM simulations in which convection becomes clustered into a quasi-circular patch over about 50 to 60 days (Tompkins & Craig, 1997; Tompkins, 2001; Bretherton et al., 2005; Muller & Held, 2012; Jeevanjee & Romps,

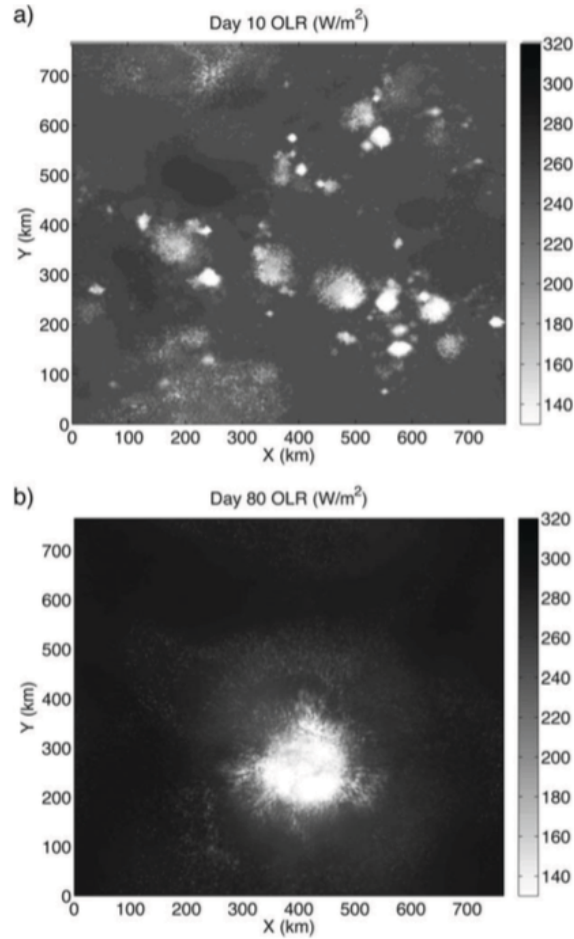


FIGURE 1.1. The outgoing longwave radiation (OLR) from an RCE CRM experiment by Wing & Emanuel (2013), at the beginning of the simulation (a), and end of simulation, (b). Low OLR indicates areas of deep convection. Figure from Wing & Emanuel (2013).

2013; and Wing & Emanuel, 2013). More recent studies have shown that convective aggregation can occur in a variety of model set-ups, including a slab-ocean with varying SST and a diurnal cycle (Hohenegger et al. 2016), and with parameterized convection in GCM simulations (Su et al., 2000; Coppin & Bony, 2015; Reed et al., 2015; Bony et al., 2016). See Figure 1.1 for an example of what convective aggregation typically looks like in a CRM.

### 1.3. MULTIPLE EQUILIBRIA OF RADIATIVE-CONVECTIVE EQUILIBRIUM

The discovery of an aggregated state in CRM simulations of RCE is important because it shows that the equilibrium state of RCE is not necessarily unique when considering more realistic interactions between convection and its environment. The hypothesis that RCE has multiple equilibria is one that has been explored extensively in the literature. A study by Renno (1997) showed that two RCE equilibria exist when including an explicit hydrological cycle (i.e. water vapor transport by convection is accounted for) in a single-column model: one in which the atmosphere had high moisture content, and one in which the atmosphere had low moisture content. Similarly, Nilsson & Emanuel (1998) found multiple equilibria in a two-column model of RCE with explicit hydrological cycle and clear-sky radiative-convective code from Renno et al. (1994a), which, in effect, included feedbacks between the dynamics, water vapor, and radiation. One equilibrium solution consisted of the presence of a large-scale circulation and dry mean state, and the other without large-scale circulation and wet mean state. Raymond & Zeng (2000) similarly showed that a circulation develops in a two-column model of the tropical atmosphere which included the radiative effects of clouds, with enhanced precipitation occurring in the updraught column. It is important to note that the RCE state associated with a large-scale circulation which was found in these theoretical studies is similar to the aggregated RCE state in the CRM simulations. It is interesting that CRM simulations frequently evolve to a wet RCE state (both aggregated and homogeneous) and not the dry RCE state as seen in these theoretical studies of RCE (e.g. Renno (1997)). Further research is needed in the area of investigating the dry RCE state in CRM simulations. A discussion of the mechanisms behind the aggregated RCE state

in CRM simulations and the effects of organized convection on the domain mean state is found in Section 1.5 and 1.6, respectively.

#### 1.4. ORGANIZED CONVECTION IN MORE REALISTIC ATMOSPHERES

The aggregated state of RCE is an example of organized convection that arises in highly idealized modeling studies, but there are various processes that organize convection in the real atmosphere as well. “Organized convection” simply refers to convection which is not randomly distributed throughout a spatial domain. For example, a tropical cyclone would be considered organized convection because it a localized region of strong convection, surrounded by a region that has little or no convective activity. Likewise, with this definition, a region of shallow cumuli in the subtropics might be considered less organized if there is no pattern associated with the cloud field. Thus, a measure of convective organization could simply be the number of convective clusters in the domain, or the degree of clustering in the domain as measured by the mean separation distance between cloud clusters, for example. It is important to note that any definition for the degree of convective organization in an observational dataset is subjective. Alternate measures of the degree of convective organization may be valid, and may also yield different, yet important, information about how the convection is organized in a domain. Results from an observational study of convective aggregation by Tobin et al (2012) are discussed later, however we emphasize that we do not intend to relate the results of this work to observations of organized convection. In the following, we only briefly introduce some important processes that contribute to convective organization in both observations of the atmosphere and more realistic simulations of the atmosphere, to give a realistic context to the highly idealized framework of this study.

1.4.1. *Observations of Organized Convection.* Often, in the real atmosphere, the scale at which convection is organized depends on the geographic location. In many cases, the convection becomes organized by an external forcing. We use the term “external forcing” to refer to conditions of the atmosphere (or topography) which act to organize convection in some way. Some examples of an external forcing include a large scale forcing, a gradient in wind or air temperature, Earth’s rotation, or a boundary like a mountain or the equator. A large scale forcing is a rate of change of an atmospheric variable that exists at length scales that are larger than the domain of interest. For example, in the Subtropics, the synoptic scale ( $> 1000$  km) forcing is mean subsidence due to the descending branch of the Hadley Cell. The drying that accompanies subsidence organizes clouds into patch-like fields of shallow cumuli. Another example of an external forcing would be in the mid-latitudes where both the Coriolis parameter and horizontal gradients in air temperature are large. Here, it is well known that baroclinic instability (instability that arises from horizontal temperature gradients in the presence of rotation) gives rise to extratropical cyclones with a length that scales with the Rossby radius of deformation,  $L_R$ . The Rossby radius of deformation is the horizontal length scale at which the effects of Earth’s rotation become appreciable. For example, at higher latitudes  $L_R$  will be relatively small because the Coriolis force is relatively large. In essence, this means that the length scale of cyclones must decrease with increasing latitude, as commonly observed. Convection can also be organized on smaller scales. In areas where strong vertical wind shear is present (e.g. along a cold front), convection may organize into a mesoscale convective system (MCS) or a squall line (Houze 2004). This often occurs in the Great Plains of the United States.

Although the Coriolis parameter,  $f$ , is small near the equator and so the Coriolis force is small, the rate of change of  $f$ ,  $\beta$ , has important dynamical effects when considering wave solutions to the equations of motion. A seminal study of equatorial waves by Matsuno (1966) showed that there are multiple wave solutions to the shallow-water equations on a  $\beta$  plane (where  $f$  is a linear function of latitude and  $\beta$  is the rate of change of  $f$  with latitude): westward propagating Rossby waves, inertio-gravity waves (waves that have both the Coriolis and buoyancy force as restoring forces), eastward propagating Kelvin waves, and mixed Rossby-gravity waves (aka Yanai waves). Since the waves are associated with pressure anomalies, there is a circulation that follows the wave propagation. It is therefore reasonable to expect that convection will be favorable where there is large scale rising motion caused by the wave-driven circulation. Thus, in the tropical atmosphere, we might expect that convective systems would be organized on length scales that are comparable to the wavelength of the most dominant equatorial wave modes.

The coupling of convection with waves in the tropical atmosphere has been studied extensively in the literature. For example, Wheeler & Kilidas (1999) performed a frequency-wavenumber spectrum analysis of satellite-observed outgoing longwave radiation (a good proxy for deep convection) in the tropical atmosphere, and found that the peaks in power agreed quite well to the dispersion relations of equatorial wave modes of the shallow wave theory. Additionally, the peak in power on the Kelvin wave dispersion relation found by Wheeler & Kilidas (1999) corresponded quite well to previous studies of satellite observations of tropical super clusters, eastward propagating ensembles of clouds with horizontal scale of several thousand kilometers (Nakazawa, 1988). An important point is that while convection tends to be organized on the length scale of equatorial waves predicted by shallow

water theory, the heating anomaly associated with the convection itself can generate waves. For example, Gill (1980) used a simple analytical model to show that a heating anomaly centered on the equator can produce a westward propagating Rossby wave and an eastward propagating Kelvin wave with cyclonic flow to the north-west and south-west of the heating source. We only briefly introduce this idea to illustrate that there is a two-way feedback between convection and waves, which makes the organization of convection by waves a complex problem.

An additional important finding by Wheeler & Kilidas (1999) was a low-frequency, low-wavenumber peak in power that did not correspond to any of the dispersion relations given by equatorial wave theory. This peak corresponds to perhaps the largest scale organized convective phenomena known as the Madden-Julian Oscillation (MJO), first discovered by Madden & Julian (1971, 1972). The MJO is a planetary scale envelope ( $\sim 12,000$  to  $20,000$  km) of convection that initiates in the Indian Ocean and slowly propagates to the east, dissipating in the western/central Pacific over a time period of about 30 to 90 days. The MJO consists of a deep, convective center with a region of weak convection to the east and west. A large overturning circulation couples the convective center to the surrounding regions, with anomalous westerly winds to the west and anomalous easterly winds to the east. The slow propagation speed and the planetary scale of the MJO are the primary features that make this convectively organized phenomenon quite different than the previously discussed convectively coupled waves. The MJO has been extensively studied in the literature (for a comprehensive review, see Zhang, 2005) and many mechanisms behind the maintenance and propagation of the MJO have been proposed. Although consensus for a theory of the MJO

does not yet exist, numerical models can simulate MJO-like disturbances of varying realism. We discuss some of those simulations in the following section.

1.4.2. *Organized Convection in More Realistic Simulations of RCE.* Convective organization has also been studied in slightly more realistic CRM simulations of RCE in which some of the idealizations used in the CRM simulations of convective aggregation are relaxed. These are important studies because they can potentially form connections between theory, idealized simulations, and real world observations of the tropical atmosphere. For example, Tompkins (2000, 2001a) studied convection in a CRM with imposed SST gradient and found that convectively active areas tend to migrate from low to high SST over time, while new warm anomalies developed away from the convective region. This finding is consistent with 2D CRM experiments conducted by Grabowski (2000), and consistent with observed SST patterns in the Tropics. Since low SSTs act to suppress deep convection, Tompkins hypothesized that a feedback between water vapor and deep convection helped maintain the convection over low SST, while migrating to regions of high SST. These studies showed that although SST gradients do indeed affect how convection organizes in a domain, feedbacks between convection and its environment are important in convective organization as well. We discuss such feedbacks in the context of convective aggregation in Section 1.5.

There have also been studies of organized convection in CRM simulations of RCE with rotation (Bretherton et al., 2005; Nolan et al. 2007; Khairoutdinov & Emanuel, 2013; Davis, 2015). In these studies, it has been shown that moist vortices can be produced in highly idealized environments (e.g. fixed SST, no large-scale forcing, no wind-shear) that have properties consistent with observations of tropical cyclones. For example, Khairoutdinov & Emanuel (2013) showed that the size of the cyclones produced in fixed SST CRM simulations

of rotating RCE scale with  $\frac{V_p}{f}$ , where  $V_p$  is the potential intensity of the cyclone, which is consistent with theory by Emanuel (1986) and an observational study by Chavas (2013). Furthermore, the spacing between cyclones was shown to scale with the Rossby radius of deformation,  $L_R$ , a well-observed property of tropical cyclones. A recent study Zhou et al (2016) relaxed the fixed-SST constraint used in previous studies of rotating RCE, and coupled a slab ocean model to a lower resolution hydrostatic model with GCM physics from the High Resolution Atmospheric Model (HiRAM). It was found that tropical cyclones could still be produced and maintained under this set-up for a variety of slab ocean depths. Finally, Davis (2015) performed rotating RCE experiments with a CRM, which were particularly important in bridging a connection between studies of convective aggregation and tropical cyclogenesis. In particular, it was found that the mechanisms that were responsible for initiation of convective aggregation in simulations of RCE without rotation were important for the genesis of tropical cyclones in simulations of rotating RCE.

Organized convection has also been studied on global scales in the idealized RCE framework with the use of general circulation models (GCMs) and super-parameterized GCMs. Super-parameterization refers to the embedment of a high-resolution two-dimensional CRM into a GCM grid box. As standard GCMs typically have coarse horizontal resolution ( $\sim 100$  km) and require extensive parameterization to represent the mean effects of convection, the advantage of a super-parameterized GCM is that the finer resolution of the embedded CRM allows convection to be explicitly resolved. For example, Grabowski (2003) and Grabowski & Moncrieff (2004) found that MJO-like structures would develop in a super-parameterized GCM on an aquaplanet (fixed SST with no continents) in RCE. They hypothesized that a feedback between moisture and convection, as similarly hypothesized by

Tompkins (2000, 2001a) was responsible for the organization of the large-scale MJO-like structures. More recently, Arnold & Randall (2015) showed that MJO-like structures can develop in the super-parameterized Community Atmosphere Model (SP-CAM) with similar idealized model set-up as in Grabowski (2003, 2004). The MJO-like structures were found to be less pronounced with homogenized longwave radiation, suggesting that a radiation-convection-moisture feedback, as observed in the CRM studies of convective aggregation, was also an important aspect of the MJO.

1.4.3. *Convective Aggregation in Observations.* The mechanisms that are responsible for organized convection in idealized RCE simulations are distinct from the external forcings which may give rise to organized convection in the real atmosphere or more realistic simulations of the atmosphere. This is because the idealized RCE simulations have no external forcing by design, and hence the mechanisms behind organized convection in these simulations must be entirely due to feedbacks that are internal to the system. It is important to note, however, that we cannot yet conclude that the convective organizing mechanisms that are present in the idealized RCE simulations are not important in the real atmosphere. More observational studies in the context of convective aggregation are required to make such conclusions. However, because of the highly idealized nature of the CRM studies of convective aggregation, observational studies of convective aggregation have been limited. Even in the Tropics, the conditions are not necessarily consistent with those imposed in these idealized RCE simulations. For example, in the Tropics there is large-scale forcing by the Hadley Cell. In the following, we discuss a couple of studies that attempt to understand the role that convective aggregation has in the real atmosphere.

Tobin et al. (2012) made an important step in bridging the gap between convective aggregation in CRM simulations and observations of organized convection in the tropical atmosphere. Using satellite observations, they found correlation between the degree of convective aggregation, free-tropospheric humidity, and OLR using a ‘simple convective aggregation index’ (SCAI) to measure the degree of convective clustering in a given domain ( $10^\circ$  by  $10^\circ$  box). The SCAI takes accounts for the mean separation distance between convective clusters, as well as the number of clusters in the domain. For example, low values of SCAI correspond to low separation distance and low numbers of convective clusters in the domain, which can be interpreted as a highly aggregated state. They found that as the degree of convective aggregation increased (the SCAI decreased), the free-tropospheric humidity decreased and the OLR increased. This is a well-known and easily reproducible correlation that is present in the CRM simulations of aggregation. However, not all of the effects of organized convection were consistent with results from the CRM simulations of convection aggregation. For example, in in the CRM simulations, the reflected shortwave radiation at the top of the atmosphere was unchanged, or increased, as the convection became more aggregated, whereas Tobin et al (2012) found that reflected shortwave radiation was reduced with higher SCAI (see Section 1.6 for more details on effects of organized convection in simulations and in observations). This was hypothesized to be due a larger fraction of low clouds in the dry region in the CRM simulations, as compared to observations. It is important to note that this study made no conclusions about the mechanisms that gave rise to the observed organized convection.

Although convective aggregation has been hypothesized to account for specific phenomena in the real atmosphere, such as tropical cyclogenesis (Davis, 2015) or the MJO (Arnold

& Randall, 2015) the mechanisms that contribute to organized convection in the Tropics may not be similar to the mechanisms that give rise to convective aggregation in these idealized simulations. A study by Bretherton et al. (2015) in which near-global CRM simulations on an aquaplanet were performed, concluded that the mechanisms that contribute to convective aggregation in the smaller scale CRM simulations are too slow to contribute to organization of convection in a more realistic setting. However, the study also concluded that larger-scale circulations, such as tropical cyclones or the MJO, may be an exception to this because their induced wind fields may be strong enough to enhance surface fluxes and produce a positive feedback effect on organization as has been often observed in the idealized numerical studies of convective aggregation.

### 1.5. CONVECTIVE AGGREGATION MECHANISMS

Initiation of convective aggregation is largely due to a positive feedback that acts on anomalously dry columns of the simulated atmosphere (Bretherton et al., 2005; Wing & Emanuel, 2014). The positive feedback is explained in the following.

In clear-sky areas (areas that are devoid of convection), there is a balance between adiabatic warming by subsidence, and longwave radiative cooling by the air. This is a well-established balance that holds remarkably well in the real atmosphere and in CRM simulations. Since water vapor is a strong absorber of longwave radiation, a column that is anomalously dry (low water vapor content) tends to have anomalous longwave radiative cooling. This is because drying of the atmosphere tends occur aloft, such that the warmer, wetter underlying atmosphere near the surface is more “exposed”. It is important to note that this is not always necessarily the case. A patch of the atmosphere that has less water

vapor will also *emit* less radiation, so that we might expect the column to cool *less* under certain circumstances. For example, if the drying occurred uniformly throughout the entire atmospheric column, the entire column would emit less and hence would have anomalous longwave radiative heating. This illustrates the importance of the vertical structure of the water vapor in the column in influencing the radiative cooling of the entire column. For a more detailed description of the effects of the vertical structure of water vapor on the radiative cooling of the column in the context of convective aggregation, see Wing & Emanuel, (2013).

In any case, during initiation of convective aggregation, the drying tends to occur aloft such that there is anomalous radiative cooling of the atmospheric column. According to the previously discussed balance, the anomalous longwave radiative cooling must be balanced by anomalous subsidence in the column, which has a further drying effect (Emanuel et al., 2014). Subsidence has a drying effect because the water vapor mixing ratio decreases roughly exponentially with height, and so subsidence will advect dry air from aloft. Drying of the column will then lead to even more longwave radiative cooling of the column, and in turn, more subsidence. This is a positive feedback because dry columns will become more dry under this process. Indeed, in animations of convective aggregation it is clear that dry patches initially become more dry and expand, eventually confining the convection to a smaller fraction of the domain.

As the drying persists and the longwave radiative cooling reaches lower levels, the subsidence becomes enhanced in the lower levels. This leads to enhanced vertical mass convergence in the lower levels, and by continuity, enhanced horizontal mass divergence in the dry columns and enhanced horizontal convergence in the humid columns (Wing & Emanuel,

2013). Eventually, a bottom-heavy circulation develops, which transports moisture from dry columns to humid columns (Bretherton et al., 2005; Wing & Emanuel, 2013). The final state is often found to be a single humid, deep convective region surrounded by a dry region of subsiding air, connected by a circulation that has strong inflow at the lower levels ( $< 2$  km), and outflow at the tropopause (Bretherton et al., 2005, Muller & Held, 2012, Muller & Bony 2015, Holloway et al., 2016).

Other processes such as enhanced surface fluxes in the convective region due to enhanced gustiness, longwave radiative warming by high clouds, and longwave radiative cooling by low clouds have been found to be important in contributing to initiation and maintenance of the convective aggregation as well (Tompkins & Craig, 1997, Stephens et al. 2008, Muller & Held 2012, Wing & Emanuel 2013). The surface latent heat fluxes were typically found to be a positive feedback in the beginning stages of convective aggregation, but then a negative feedback during the mature stage. During the beginning stages, enhanced gustiness at the sea surface enhances evaporation in convective areas, but then during mature stages, evaporation becomes very strong in the dry region. This is because the air-sea water vapor disequilibrium becomes increasingly large in the dry region as the air become significantly more dry in the aggregated state. Maintenance of the aggregated state seems to be mostly due to positive feedback processes driven by high clouds in the convective region (Muller & Bony 2015). More specifically, reduced longwave cooling (i.e. anomalous warming) due to high clouds in the convective region must be balanced by adiabatic cooling (upward motion), which further contributes to moistening of the convective region. Low clouds in the dry region are important for the development of the bottom-heavy circulation in the beginning stages of convective aggregation (Muller & Held 2012). This is because low clouds

are associated with strong longwave radiative cooling at the cloud tops, which in turn leads to strong low-level subsidence.

Studies have also identified the most important mechanisms which contribute to both the initiation and maintenance of convective aggregation via mechanism denial experiments. For example, Bretherton et al. (2005) showed that convection would remain in a disorganized state if the longwave radiative cooling was homogenized (i.e. the domain mean radiative cooling was applied to every grid point). This eliminates the previously discussed drying feedback on the system because this feedback requires spatial variability of longwave radiative cooling. Muller & Held (2012) and Tompkins (1998) also found that convective aggregation would not initiate with homogenized longwave radiative cooling. Furthermore, Muller & Held (2012) found that delaying the homogenization of longwave radiative cooling until after the convection aggregated still resulted in disorganized convection after about 20 days. While it is known that the spatial variability of longwave radiative heating is important throughout all stages of convective aggregation, studies have suggested that the spatial variability of surface fluxes only favors initiation of convective aggregation. Convective aggregation may still initiate with homogenized surface fluxes (Muller & Held, 2012, Tompkins, 1998). Finally, Muller & Held (2012) investigated the contribution of low clouds to longwave cooling by eliminating all liquid water at low-levels ( $> 700$  hPa). It was found that while low clouds were necessary for initiation of aggregation, they were not necessary for maintenance of the aggregated state. A follow-up study by Muller & Bony (2015) found that the aggregated state could be maintained with only low-level clear sky cooling in the dry regions and a mid-level radiative warming anomaly caused by high clouds in the convective region.

## 1.6. EFFECTS OF ORGANIZED CONVECTION

The degree of convective organization has been shown to have significant effects on the mean state of the atmosphere. For example, the mean state is more dry when convection is more organized. This has been shown in both the simulations (Bretherton et al., 2005) and in observational studies of aggregated convection in the Tropics by Tobin et al. (2012, 2013). Furthermore, numerous modeling studies of convective aggregation have shown that the domain mean outgoing longwave radiation (OLR) increases as a result of the drying (Emanuel & Khairoutdinov, 2010, Muller & Held, 2012, Wing & Emanuel, 2014, Holloway et al. 2016). OLR has been shown to increase with the degree of aggregation in observations as well (Tobin et al., 2012, 2013). Both the domain mean precipitation and the precipitation efficiency have also been shown to increase relative to the homogeneous RCE state in simulations (Bretherton et. al., 2005) and in observations (Tobin et al. 2012).

There is inconsistency among the numerical studies and the observations in terms of the effect that aggregation of convection has on cloudiness, (the mean cloud fraction) and the radiative effects associated with those changes in cloudiness. Most numerical modeling studies of convective aggregation have reported negligible or slight increases in cloudiness, however the observational studies of aggregated convection by Tobin et al. (2012), observed reduced low-level cloudiness and an associated reduced reflected shortwave radiation and increased OLR. The increased OLR with the degree of convective organization is consistent with what is observed in the simulations of convective aggregation, however the reduced cloudiness and the increased shortwave convergence effect does not seem to be present in these simulations. In particular, the cloudiness has often observed to be unchanged, along with the shortwave convergence. However, it is important to note that the simulations are

not necessarily expected to successfully simulate low clouds because the model resolution is often too coarse ( $\sim 3$  km).

The relationship between the degree of convective organization and cloudiness has implications on climate change studies. If the degree of convective organization and related changes in cloudiness are sensitive to a warming climate, this could have important feedback effects on climate change because clouds have important radiative effects on the atmosphere. In particular, if a higher degree of convective organization leads to an increase in OLR in excess of the increase in absorbed solar radiation by the atmosphere and surface, this could be a negative feedback on global warming. Here, a negative feedback refers to any change in the climate which opposes further warming of the climate. Lindzen et al. (2001) first proposed such an idea, and termed this the “iris effect”, forming an analogy with the pupil, which contracts and expands in response to the amount of incoming sunlight. With warmer SSTs, Lindzen et al. observed the high cloud fraction to decrease (the contracting pupil), and hypothesized that this would lead to an increase in OLR in excess of the increase in absorbed solar radiation by the surface. This is because more of the warmer surface is exposed to space with less high clouds, (the exposed iris), which would lead to an increase in OLR and potentially have a cooling effect on the Earth. Although the simplicity of such an analogy is appealing, a follow-up study by Lin et al. (2001) found that the increase in shortwave absorption accompanied by the decrease in cloud fraction exceeded the decrease in OLR, such that the decrease in high cloud fraction was actually a positive feedback on the climate. This highlights the importance of multiple competing radiative effects when considering changes in cloudiness in global warming experiments. For example, the decrease in high cloud fraction in global warming experiments is also robustly associated with an

increase in high cloud height so as to maintain a fixed temperature at the cloud top (e.g. Bony et al. 2016). This is referred to as the *fixed-anvil temperature* (FAT) hypothesis, first hypothesized by Hartmann & Larson (2002). This is a *positive* feedback on global warming because the atmosphere has warmed while the amount of radiation emitted from the atmosphere has remained the same. Thus, in this case, the radiative effect of the increase in cloud top height opposes the radiative effect of the decrease in high cloud fraction. Importantly, however, a recent study by Hohenegger & Stevens (2016) has shown that the occurrence of convective aggregation in a CRM is necessary for the climate reaching an equilibrium state and avoiding a run-away greenhouse effect. Here, a run-away greenhouse effect refers to a climate which continues to warm. This was thought to be due to the fact that convective aggregation effectively generates large regions of dry, clear air which more effectively emit radiation to space. This idea is reminiscent of a study by Pierrehumbert (1995), wherein a simple model was used to show that the tropical climate effectively cools via the dry subtropics, much like radiator fins. These studies present future research questions on the topic of convective aggregation and climate sensitivity.

### 1.7. CONVECTIVE AGGREGATION DOMAIN SIZE DEPENDENCY

Convective aggregation can occur with a variety of domain sizes and geometries. In most cases, the square domain CRM studies of RCE have been limited to width less than about 1536 km, which resulted in the formation of a single convective in the domain. In these limited-area CRM experiments, it is known that convective aggregation will not occur with side length less than 200 km (Muller & Held, 2012, Jeevanjee & Romps, 2013). This is

thought to be due to more efficient domain-scale mixing of water vapor by convection-induced cold pools at smaller domain sizes (Jeevanjee & Romps, 2013).

In more recent large-scale studies of RCE, however, it has been shown that convection can organize into multiple convective clusters in the domain. For example, in a global-scale study of RCE on an aquaplanet with explicitly resolved convection by Arnold & Randall (2015), convection organized into multiple clusters across the globe over time. Similarly, GCM simulations of RCE with parameterized convection on an aquaplanet without rotation have shown some level of aggregation occurring, with more than one convective region forming in the domain over time (Su, 2000, Coppin & Bony, 2015, Reed et al. 2015, Bony et al., 2016). See Figure 1.2 for examples of what convective aggregation looks like in these studies. Additionally, Wing & Cronin (2015) simulated convective aggregation using a long-channel domain geometry ( $\sim 12,000$  km x 200 km) which resulted in multiple convective bands forming along the channel. Wing & Cronin also developed a theory for the length scale of the dry regions in these simulations, which was based on the distance a parcel of air must travel in the boundary layer before becoming saturated. The theory could not robustly reproduce the simulation results.

It should be noted that there is still a significant gap between our understanding of organization of convection in small-scale CRM simulations and large-scale GCM simulations of the atmosphere in RCE. Although convective aggregation appears to occur in GCMs in RCE with parameterized convection, more research is needed in the area of describing the mean aggregated state and the mechanisms that give rise to this state. On this very subject, a recent study by Coppin & Bony (2015) investigated the mechanisms that give rise to organization of convection in a GCM in aquaplanet configuration. They found that cloud-radiative

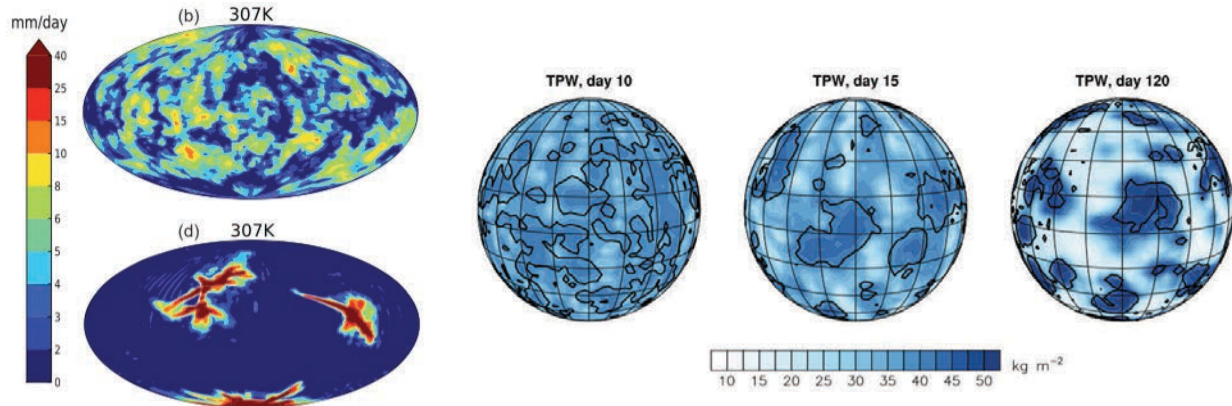


FIGURE 1.2. Left: Global snapshots of precipitation (mm/day) from non-rotating RCE experiments conducted with a GCM (IPSL-CM5A-LR) with fixed SST of 302 K (top: day 290, bottom: day 650). Figure reproduced from Coppin & Bony (2015). Right: Daily average total precipitable water ( $\text{kg m}^{-2}$ ) on days 10, 15 and 120 from non-rotating RCE experiments conducted with a super-parameterized GCM (SP-CAM). Black contours indicate where 500 hPa vertical velocity is zero. Figure reproduced from Arnold & Randall (2015).

feedbacks were important in initiation and maintenance of convective aggregation, similar to previous CRM studies of convective aggregation (Muller & Held, 2012, Muller & Bony, 2015). In particular, convective aggregation would not occur without a radiative warming anomaly in the mid to upper troposphere in the deep convective region, accompanied by low-level cooling (caused by either low clouds, or a dry free troposphere) in the convection-free region.

A recent study by Silvers et al (2016) explored how the mean state of a GCM in RCE with idealized model set-up similar to the CRM studies of convective aggregation varies with domain sizes which span multiple orders of magnitude. Organization of convection occurred with all domain sizes, but convergence in the mean state occurred at the 4000 km domain length scale. Likewise, a study by Reed et al. (2016) investigated convective organization in a GCM in RCE with varying planetary radius. In this study, the horizontal resolution was systematically reduced while maintaining spherical domain geometry and the same number

of grid points, which, in effect, reduced the planetary radius and hence reduced the domain size. It was found that convection would organize into ribbon like structures with the larger domain size, while only a single convective cluster would form in the smaller domains. It was additionally found that the mean RCE state in the reduced radius planet run with 28 km horizontal resolution was similar to that of an Earth-sized planet with 28 km horizontal resolution, suggesting that effects of organized convection on the mean RCE state converge at some length scale. These studies are important in bridging the gap between GCM and CRM simulations of RCE because it is not clear which domain size should be utilized when comparing the aggregated RCE in a CRM to the RCE state in a GCM. Based on this work, a particularly useful series of questions could be posed: does the aggregated state in a CRM simulation show this type of sensitivity to domain size, and does the aggregated state converge at some domain size? In the case that convergence occurs at a similar domain size in both a CRM and a GCM in RCE, then we may be confident that the parameterization of convection in the GCM accurately accounts for the mechanisms responsible for convective aggregation in the CRM simulations. On the other hand, if the results converge at different domain sizes, this might suggest that certain aspects of the convective parameterization do not accurately capture certain aspects of convective aggregation. Likewise, it should also be mentioned that even if the mean state converges at similar domain size, it is not guaranteed that the mean states themselves will be similar. This highlights the need for more detailed description of the mean RCE state across a variety of domain sizes in both CRMs and GCMs.

## 1.8. OBJECTIVE OF THESIS

Overall, the previously discussed studies suggest that the domain artificially constrains the spatial scale of convective aggregation. Specifically, in small scale CRM studies of aggregation, in all cases there is only one convective cluster, however in large scale studies of aggregation (with and without explicitly resolved convection) there are multiple convective clusters. This suggests that convective aggregation acts on a preferred scale, however a theory for the natural spatial scale of convective aggregation (i.e. the spatial scale of convective aggregation without domain constraint) remains unknown. This particular point serves as motivation for the current study. The previously discussed studies also motivate the need for a detailed description of the aggregated state across a variety of domain length scales in a CRM. This work could set the stage for more detailed comparison between the aggregated RCE state in a CRM and that of a GCM, which can be thought of as the next level of complexity in the hierarchy of models of the atmosphere. Therefore, we simulate convective aggregation in a CRM with doubly-periodic square domains of width: 768 km, 1536 km, and 3072 km in order to investigate the preferred separation distance between convective clusters. We also analyze differences in the aggregated state between the three domain cases. We argue that the square domain is preferable to the long-channel domain used in Wing & Cronin (2015) in investigating the natural spatial scale because we believe that a proportionally smaller domain side length may artificially force the convection to organize into band-like structures.

The details of the simulation set-up are outlined in the Methods section. We then show the differences in the aggregated state across the three different domain cases in proceeding

sections, and give a physical interpretation of the results along in the Discussion & Conclusions section. We also introduce a simple mode of the aggregated state in the Discussion & Conclusions section in order to better understand the simulation results and explore the dependency of the spatial scale of the aggregated state on the domain size. We conclude by discussing the future direction of this work.

## 2. METHODS

### 2.1. SIMULATION SET-UP

A cloud-resolving model, the System for Atmospheric Modeling (SAM) (Khairoutdinov and Randall, 2003), is used to simulate convective aggregation on doubly-periodic square domains of width 768 km, 1536 km, and 3072 km. In all cases, we use a 1-moment microphysics package, and the solar insolation is constant and equal to a value of  $413.98 \text{ W/m}^2$  with a zenith angle of 50.5 degrees. This is higher than the globally averaged solar constant of  $340 \text{ W/m}^2$ , but is consistent with previous studies of convective aggregation (Bretherton et al. 2005, Wing & Emanuel, 2013, Arnold & Randall, 2015). Radiative fluxes are calculated every 200 s using the RRTM scheme (Mlawer et al., 1997). The model grid is a fully staggered Arakawa C-type grid with a uniform horizontal resolution of 3 km and a stretched vertical grid with 64 levels. The lowest model level is at 25 m with grid spacing of 50 m near the surface, and increasing to 500 m above 4.5 km.

For all simulations, the sea-surface temperature (SST) is fixed at 302 K (29 °C), which is quite warm but still below the maximum observed tropical SST of 32 °C. This SST is mainly used because previous studies have shown that convective aggregation may not occur if the SST is lower than approximately 300 K. The sensitivity of convective aggregation to SST is a subject of ongoing research, but will not be further discussed in this study.

We initialize the 768 x 768 km domain with domain-averaged water vapor and temperature profiles from a 96 x 96 km RCE simulation. The 96 x 96 km simulation is initialized with an SST of 302 K and a fixed temperature lapse rate of 6.5 K/km up to about 150 hPa, where the temperature is set to be vertically uniform. The water vapor profile is given by the relative humidity in the TOGA-COARE field project (Webster & Lukas, 1992). The 96 x 96

km domain is too small to allow aggregation to occur, so that the initial profiles correspond to a state of homogeneous RCE. The 96 x 96 km simulations is run until equilibrium. The resulting temperature and water vapor profiles, which are not significantly different than the initialization of the 96 x 96 km domain, are then used to initialize the 768 x 768 km domain simulation. The mean winds are nudged to zero in order to prevent a QBO-like oscillation from developing (Held et al. 1993). Although convective aggregation occurs without nudging (Holloway et al., 2016), this simplifies the analysis of the dynamics.

In all cases, both 2D fields (x-y) and domain mean variables are output every hour, whereas 3D (x-y-z) fields are output every 6 hours. In the case of the largest domain (3072 x 3072 km), a given sample of a 3D field is made up for approximately 67 million grid points, whereas the small domain (768 x 768 km) has 16x less grid points at around 4 million.

The small domain (768 x 768 km) simulation is run until aggregation occurs, at which point we initialize the larger domain simulations with copies of the steady-state aggregation from the small domain simulation, plus a small low-level temperature perturbation. This initialization method is consistent with doubly-periodic boundary conditions. Other than introducing a small perturbation, the mean state of the atmosphere is not changed in any way by doubling the domain and initializing in this manner. Another justification for this initialization technique is that we assume the the simulation will evolve to either a homogeneous or aggregated equilibrium state, regardless of the specific details of the initial state. The idea that the aggregated convection state is an alternate equilibrium state of RCE is consistent with previous theoretical studies of RCE (as discussed in Section 1.3). We run the larger domain simulations until steady-steady is achieved. We believe that this method

of initialization will decrease the amount of time needed to reach steady-state, and hence decrease the computational cost.

### 3. EVOLUTION TO STEADY-STATE

The small domain (768 x 768 km) simulation aggregates at around day 70, with a steady decline in domain mean precipitable water (PW) preceding this (see Figure 3.1). Note that although the small domain case aggregates around day 70, it reaches steady-state at around day 150 with small fluctuations in PW ( $< 5\%$  mm) about a mean value of approximately 28.0 mm. The significant drying of the domain up until around day 70 is consistent with previous studies of convective aggregation (see Bretherton et al., 2005, Muller & Held, 2012, Wing & Emanuel, 2013) and is primarily because the fraction of the domain occupied by subsiding air increases as convection aggregates. A secondary reason for the drier domain is because precipitation efficiency increases as convective cores become more clustered.

Note that the short time scale ( $< 1$  day) oscillations in the PW time series are thought to be the combined effects of a convective “recharge-discharge” mechanism by convectively-generated cold pools, and by gravity wave propagation (Wing & Cronin, 2015; Naegel, 2016). By visible inspection, there are longer time-scale quasi-periodic fluctuations ( $\sim 25$  to 30 day) present as well. Additionally, these fluctuations seem to be higher amplitude with increasing domain size. For example, in the small domain case the amplitude of oscillation is about 0.5 mm, whereas in the large domain case the amplitude of oscillation is about 3 mm.

The larger domains are initialized with the small domain state at day 90 (denoted by the blue line in Figure 3.1a). In both cases, the convective clusters merged in a pair-wise fashion, eventually forming a single convective cluster surrounded by a dry, subsiding region (see Figure 3.2a,b and Supplementary Materials 1; animation of precipitable water during convective merging for the large domain case). Figure 3.3 shows the final single cluster in

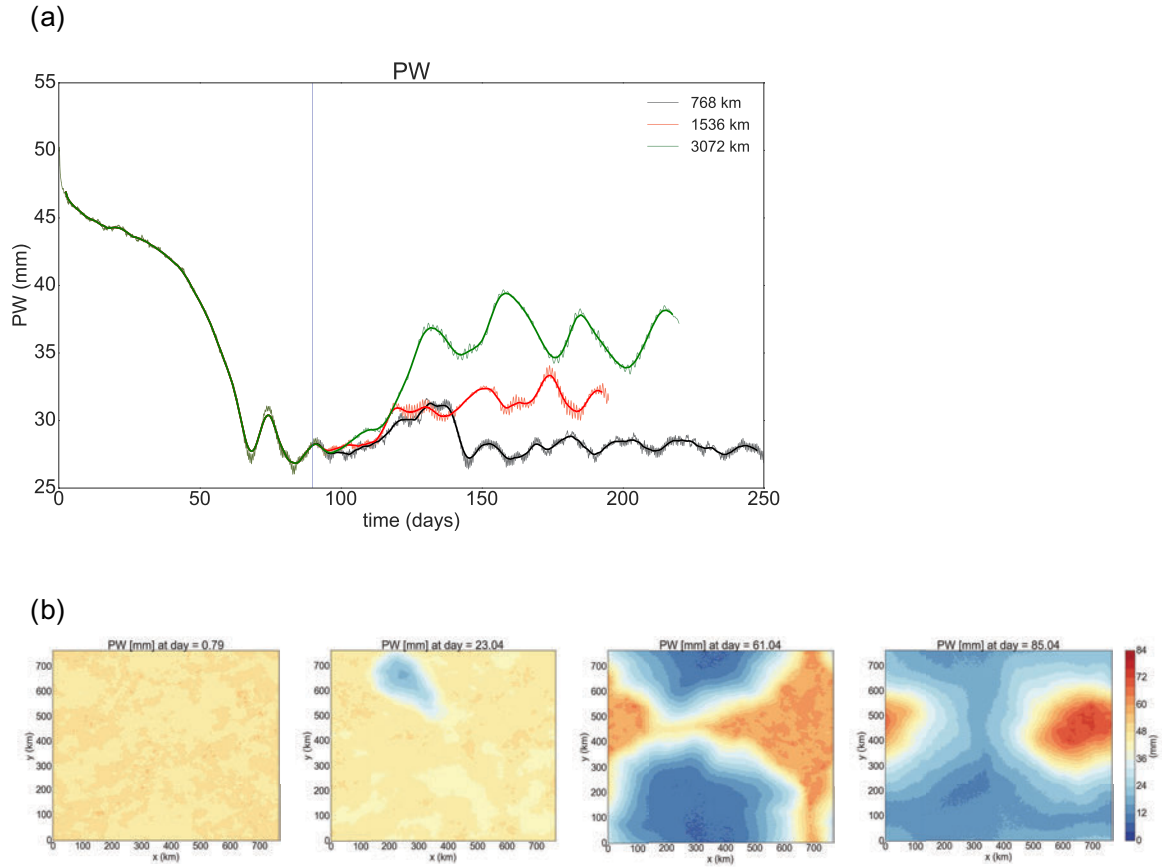


FIGURE 3.1. The domain-mean precipitable water for small domain, medium domain, and large domain case in black, red, and green, respectively is shown in (a). The vertical blue line marks the time at which the larger domain cases were initialized. The thin line is an hourly time series, and the thick line is a 5-day running mean. (b) Hourly maps of PW during convective aggregation for the small domain case (768 x 768 km).

each case on the same grid as the large domain case so that the size of the convective region can be more easily compared between the cases. In the medium domain case, the convective clusters re-organized into a single convective cluster around 30 days after initialization, and in the large domain case the convective clusters re-organized around 40 days after initialization. The domain-mean PW is higher with larger domain size, with an upward trend during

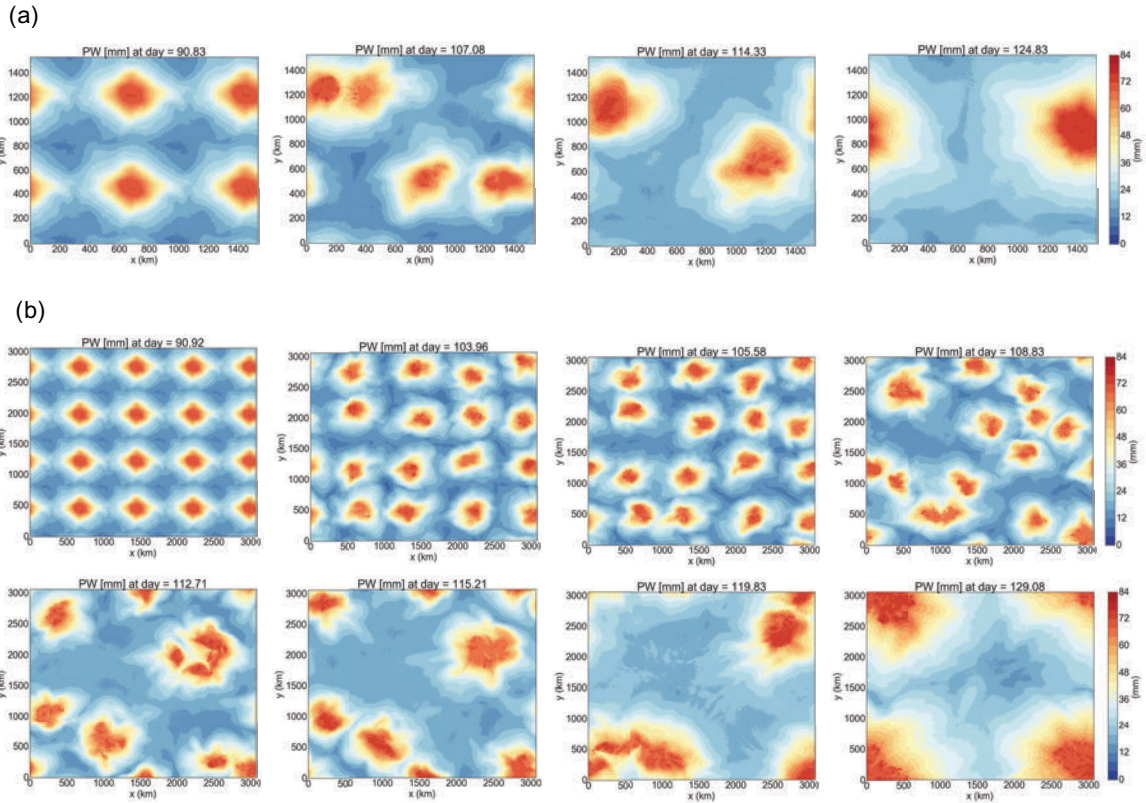


FIGURE 3.2. Hourly maps of PW throughout the convective merging process (a): medium domain case (1536 x 1536 km) and (b): large domain case (3072 x 3072 km).

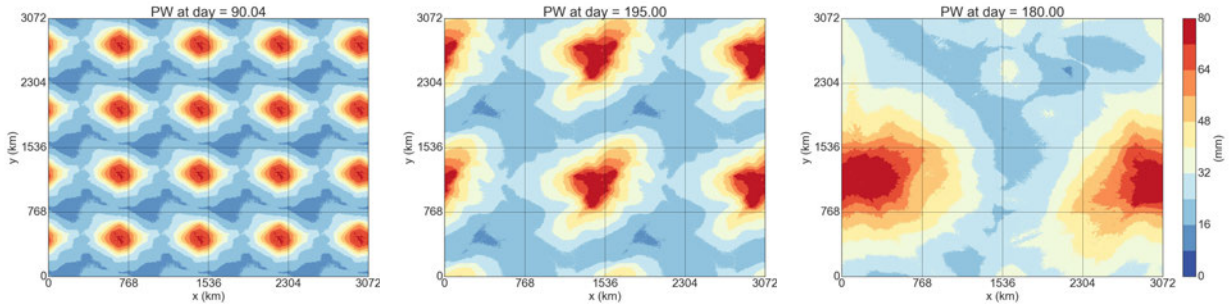


FIGURE 3.3. Maps of PW at the end of simulation re-mapped onto the large domain grid for the small (768 x 768 km), medium domain (1536 x 1536 km) and large domain case (3072 x 3072 km) (left to right, respectively). Grid lines are drawn every 768 km to facilitate comparison between the cases.

the convective merging process (see Figure 3.1a). The increase in domain-mean water vapor mixing ratio occurs primarily in the lower troposphere/boundary layer and in the mid troposphere (see Figures 3.4 and 3.5). In Figure 3.5, we have plotted the difference between water vapor mixing ratio (in mm) before and after the domain doubling, to see where the largest increase in moisture occurred in the column. Evidently, the low-level moistening is the primary reason for the increase in PW, with the mid-level moistening having a secondary effect. While it is clear that the boundary layer becomes more wet and deep, Figure 3.5 also suggests that the shallow cumulus activity increased with domain size. Likewise, the mid-level moistening suggests that mid-level cumulus congestus activity increased with domain size. We return to these points later.

The medium domain case (1536 x 1536 km) seems to have reached a quasi-steady state at around day 145, with PW fluctuations ( $\sim 5\%$ ) about a mean value of approximately 31.8 mm. Similarly, the (3072 x 3072 km) seemed to have reached a quasi steady-state by day 150, however there are large fluctuations in the PW ( $\sim 5\text{-}8\%$ ) about the final 10-day mean value of approximately 35.1 mm.

Note that an additional important result for the large domain case is that a second smaller convective cluster formed in the domain at around day 185, but then re-merged with the larger cluster at around day 200 (Figure 3.6 and Supplementary Materials 3; animation of cloud top height for large domain case). We later investigate changes in the RCE aggregated state before this smaller cluster formed.

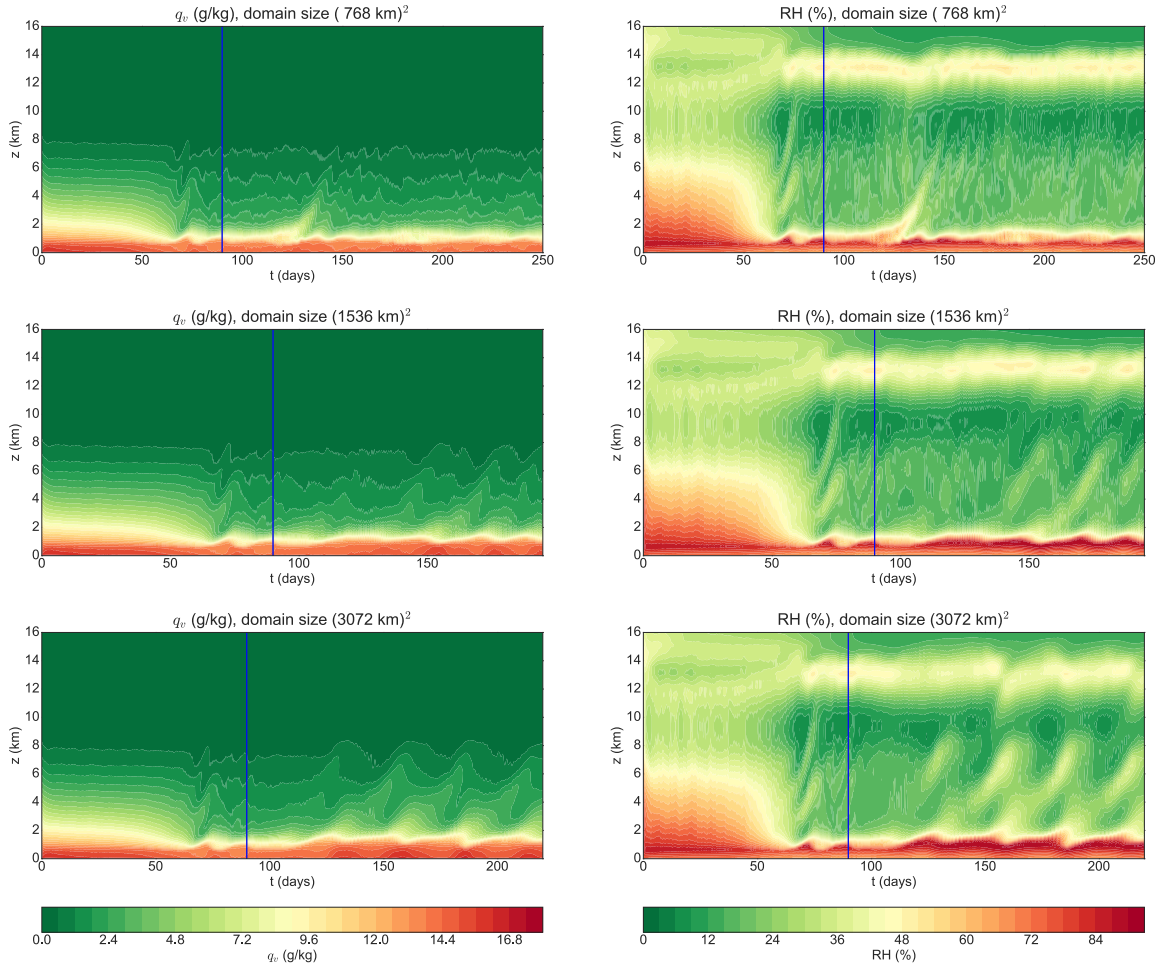


FIGURE 3.4. Hourly time-height cross section of relative water vapor mixing ratio,  $q_v$  (g/kg) (left), and relative humidity, RH (%) (right), for small domain case (top), medium domain case (middle) and large domain case (bottom).

### 3.1. CONVECTIVE MERGING

It is important to note that the convective merging process which gave rise to the single convective cluster in the larger domain simulations (Figure 3.2) was different from the convective aggregation process which occurred in the small domain (Figure 3.1b). The organization of convection which occurred in the small domain is consistent with previous studies of convective aggregation, wherein a large dry patch developed and forced the convection into a confined area of the domain. This convective merging also appears to be different than the

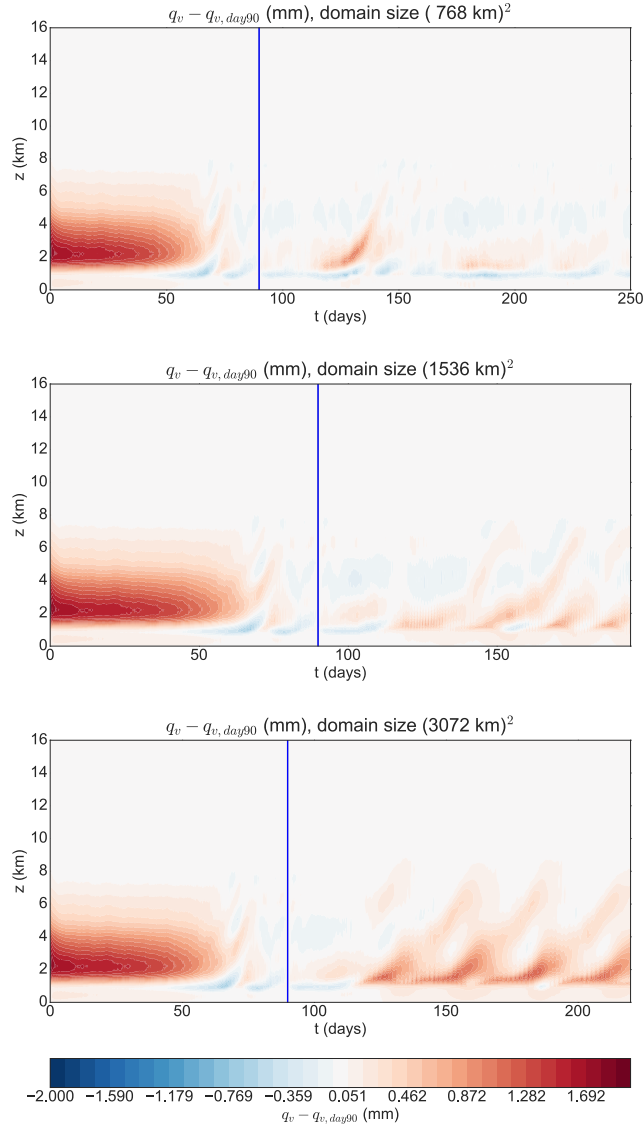


FIGURE 3.5. Hourly time-height cross section of the horizontal mean water vapor mixing ratio at time  $t$ ,  $q_v$  (g/kg), minus the horizontal mean water vapor mixing ratio at day 90, for small domain case (top), medium domain case (middle) and large domain case (bottom).

“coarsening” process outlined in Craig & Mack (2013), wherein moist patches interact with the environment in a manner that is analogous to the way that water droplets interact with their environment during cloud droplet growth. Specifically, smaller moist patches require an environment which is more wet (like small water droplets), whereas larger moist patches can persist with a drier environment (like large water droplets). In effect, the large moist

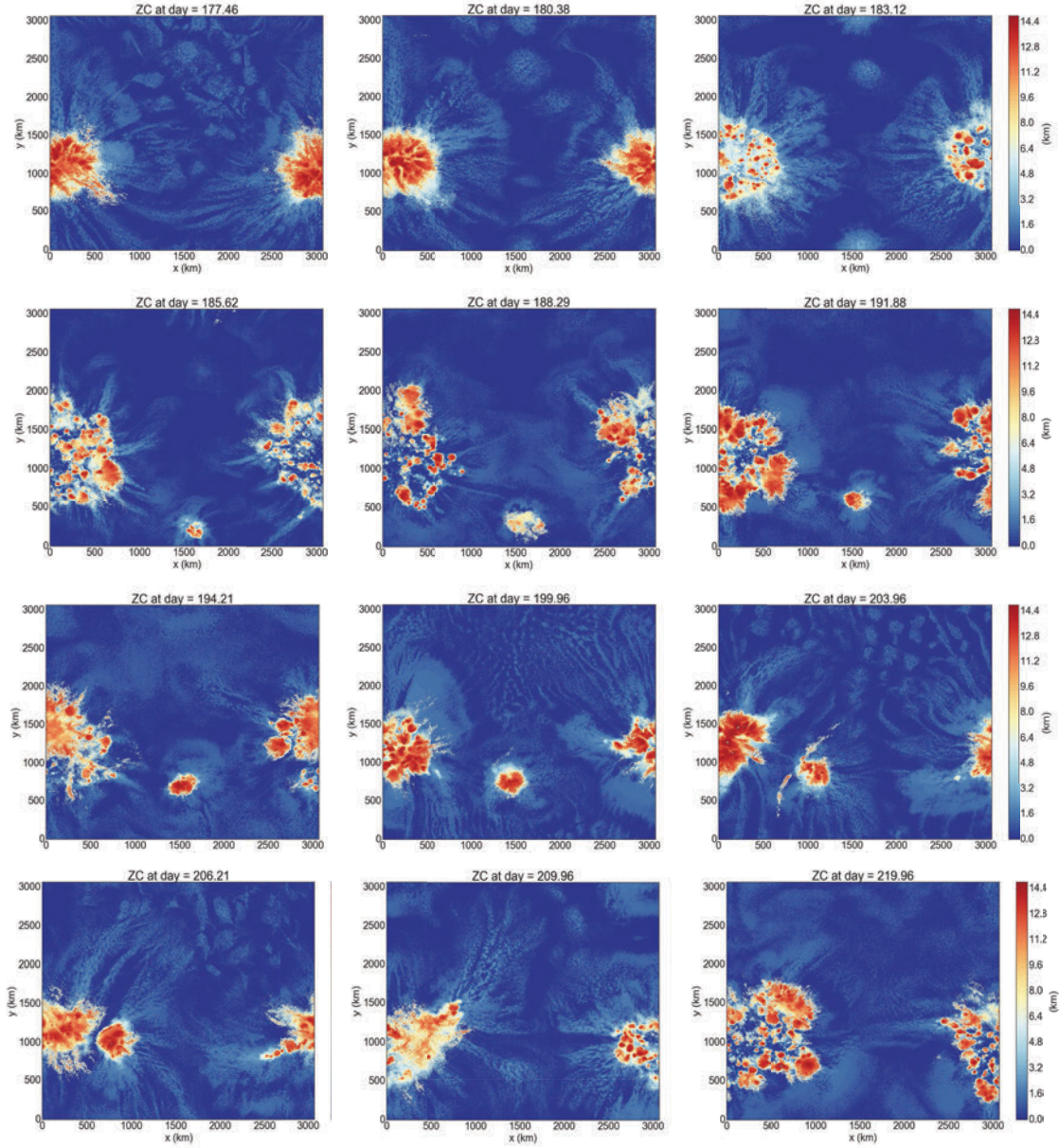


FIGURE 3.6. Maps of cloud top height (km) for the large domain case. Snapshots are approximately every 3 days except in the case of the last panel, which corresponds to the last time step of the simulation (day 220).

patches “feed” on the moisture in the environment, and cause the smaller moist patches to dissipate while the large moist patches grow. Eventually, the environment is significantly dried, such that the only the largest moist patch can persist.

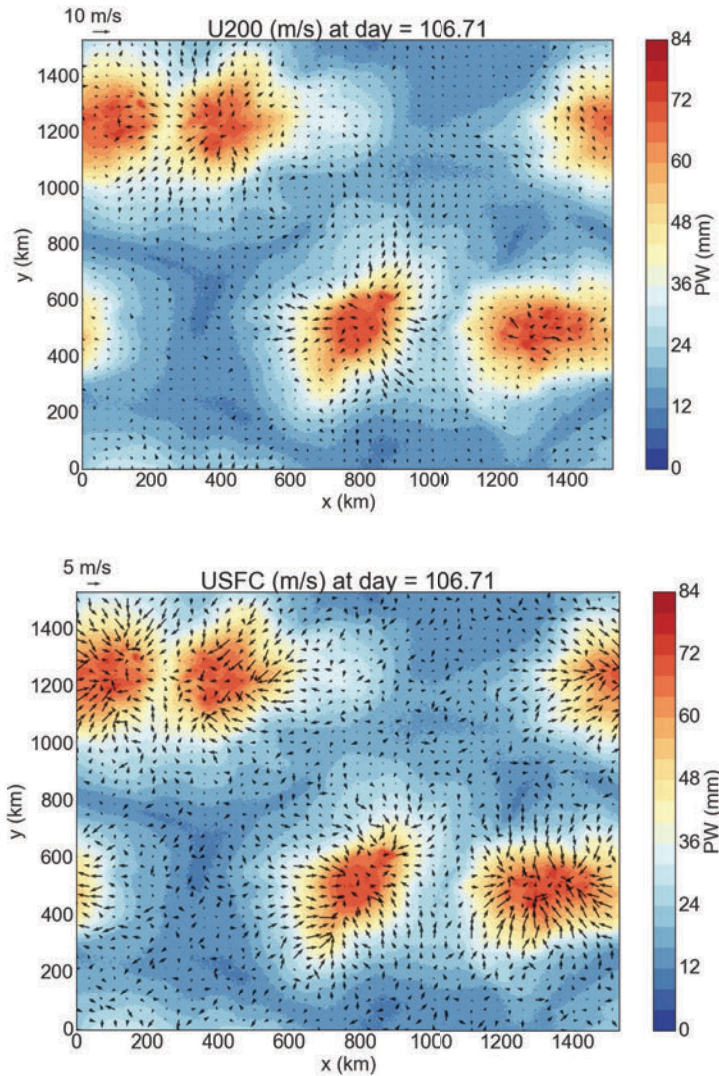


FIGURE 3.7. 200 hPa wind field (top), and surface wind field (bottom) during convective merging (day 106) for the medium domain case. Note that the wind speed scale, indicated by the length of the wind barb, is different for the two fields. The 200 hPa wind scale is 10 m/s and the surface wind scale is 5 m/s. Colored shading is precipitable water (mm).

Maps of lower-level and upper-level winds during the convective merging suggest that the circulation associated with each convective cluster favors the merging of clusters. Specifically, the outflow at tropopause (and hence the compensating subsidence-induced drying) is directed adjacent to neighboring convective clusters, whereas the low-level inflow (and hence

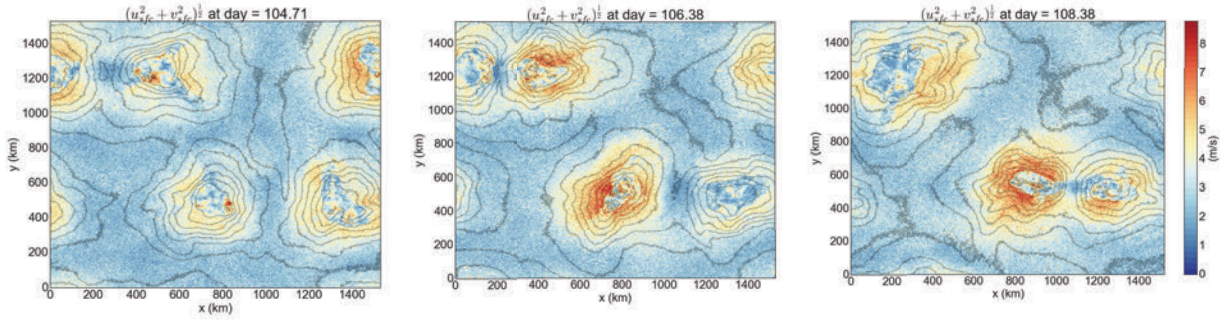


FIGURE 3.8. Maps of surface wind speed during convective merging (day 104 to 108) for the medium domain case. Grey contours are precipitable water, drawn every 8 mm (max: 88 mm, min: 20 mm). Colored shading is surface wind speed (m/s).

low-level moisture advection) is directed toward neighboring convective clusters (see Figure 3.7). We hypothesize that the circulations produced by two clusters superimpose in such a way that will produce a surface wind speed minimum at some point between the clusters. In turn, we predict that the convective clusters will move toward the surface wind speed minimum by advection, since the stronger outside inflow surface winds will prevail over the weaker inside inflow winds. This is illustrated in Figure 3.9. In this simple schematic, we have plotted idealized surface radial wind velocity,  $u$ , as a function of radial distance,  $r$ , for two convective clusters. The coordinate of the center of the convective cluster,  $r_c$ , is given by  $r_c = r_1 = 0$  km and  $r_c = r_2 = 700$  km, 600 km and 300 km. Note that we have set the convective clusters a distance apart that is comparable to the initial separation distance between convective clusters in the large domain (3072 x 3072 km). We use a  $u$  profile of the form  $u(r) \sim (r_c - r)e^{[K(r-r_c)^2]}$ , which is consistent with the shape of the surface wind speed radial profile in our simulations (shown later). Note that  $K$  is a constant and chosen to obtain a reasonably shaped velocity profile. Importantly, we can see that the the sum of the two velocity profiles results in weakened velocity inside the merging zone and there is a

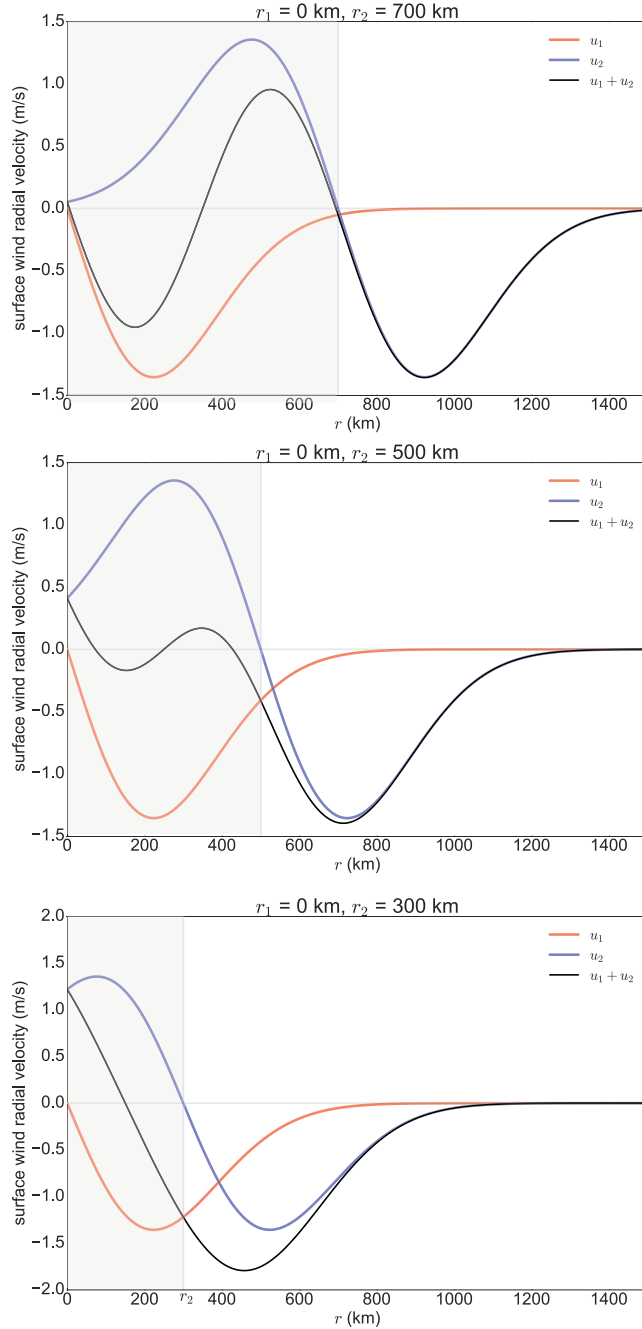


FIGURE 3.9. Idealized radial profiles of surface wind radial velocity during convective merging. Profiles are plotted for two different convective clusters ( $u_1$  and  $u_2$ ; red and blue, respectively) with three different separation distances ( $r_2 - r_1 = 700$  km,  $500$  km, and  $300$  km; top, middle, and bottom, respectively).  $u_1 + u_2$  is also plotted as the solid black line. The light grey area represents the “merging zone”, which is the region between the two convective clusters. The functional form of  $u_1$  and  $u_2$  is  $(r_c - r)e^{[K(r-r_c)^2]}$ , where  $r_c$  is the radial coordinate of the center of the convective cluster ( $r_2$  or  $r_1$ ), and  $K$  is an arbitrary constant.

velocity minimum between the two clusters, as hypothesized. Note that when the convective clusters are further apart, there is mass divergence in the merging zone, which would oppose the merging of the clusters. However, when the convective clusters are closer, the divergence weakens (see the  $r_2 = 500$  km case, middle panel) and eventually becomes mass convergence (see the  $r_2 = 300$  km case, bottom panel). It is important to remember that the shape of the velocity profile is chosen arbitrarily, but this schematic illustrates that it is possible for two circulations to interact in such a way as to produce mass convergence between two convective clusters, and hence favor the merging of the two clusters.

Consistent with this hypothesis, our simulation results show that inflow boundary layer winds between adjacent merging clusters became weak, with a surface wind speed minimum forming between the merging clusters, while inflow winds outside the merging zone remained strong (see Figure 3.8; note the “horse-shoe” pattern in the wind speed). Additionally, animations of the surface wind speed show that the clusters migrate toward the surface wind speed minimum (see Supplementary Materials 2; animation of surface wind speed and precipitable water during convective merging for the medium domain case).

To further explore the mechanisms behind the convective merging, we calculate a budget for the column-integrated frozen moist static energy (FMSE),  $\hat{h}$ , during the convective merging process. The FMSE is given by:

$$h = c_p T + gz + L_v q_v - L_f q_{ice} \quad (1)$$

We use FMSE because it is exactly conserved by the CRM governing equations, for adiabatic fluid motions. The budget equation for vertically-integrated FMSE is given by:

$$\frac{\partial \hat{h}}{\partial t} = LW_{net} + SW_{net} + SEF - \nabla_H \cdot \hat{\mathbf{u}}h \quad (2)$$

The  $\hat{x}$  notation represents a density weighted vertical integral of the variable  $x$ . SEF is the sum of the surface sensible heat and latent heat flux.  $LW_{net}$  and  $SW_{net}$  are the column longwave and shortwave radiative flux convergences, respectively, and are given by differences in net radiative fluxes between the top and bottom of the atmosphere:

$$LW_{net} = LW_{sfc} - LW_{top} \quad (3)$$

$$SW_{net} = SW_{top} - SW_{sfc} \quad (4)$$

Following the analysis of the mechanisms contributing to convective aggregation by Wing & Emanuel, (2012), we subtract the horizontal mean of equation (2) from the full form of the equation and then average over the domain to obtain an equation for the rate of change of the spatial variance of the vertically integrated FMSE:

$$\frac{1}{2} \frac{\partial \overline{\hat{h}'^2}}{\partial t} = \overline{\hat{h}' LW'_{net}} + \overline{\hat{h}' SW'_{net}} + \overline{\hat{h}' SEF'} - \overline{\hat{h}' \nabla_H \cdot \hat{\mathbf{u}}h} \quad (5)$$

The  $x'$  notation represents the departure of a variable  $x$  from its horizontal mean. The terms on the right hand side of (5) are correlations of FMSE anomalies with different terms in the FMSE budget. In other words, (5) quantifies whether a moisture anomaly will be enhanced (a positive correlation) or damped (a negative correlation) by specific processes like longwave radiative heating or surface fluxes. We calculated all terms from the model

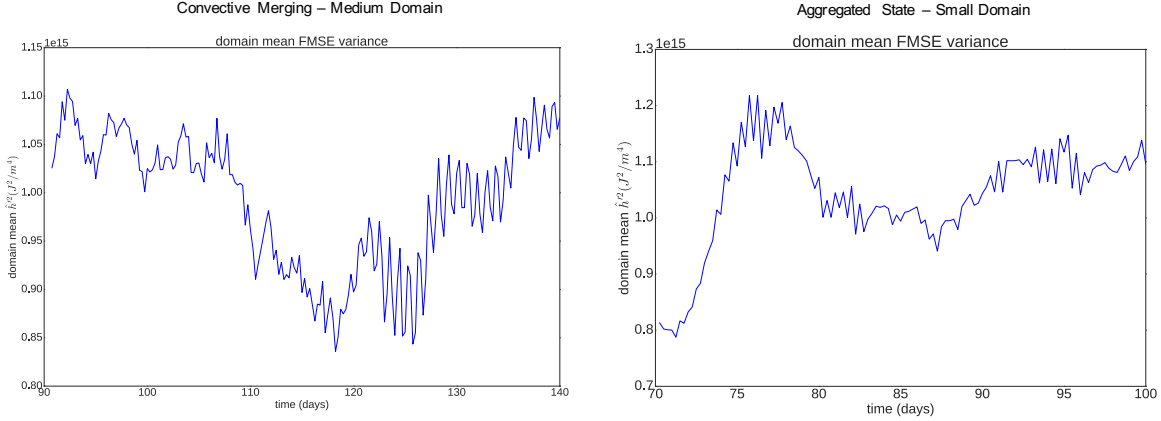


FIGURE 3.10. Left: domain mean FMSE variance for the medium domain case, plotted between day 90 to day 140. Note that convective merging occurs between around day 100 and day 125. Right: domain mean FMSE variance for the small domain case, plotted between day 70 and day 100. Note that the small domain reaches a relatively steady aggregated state around day 75.

outputted fields at 6-hourly intervals during convective merging (day 90 to 140). The horizontal convergence term was calculated as a residual from the rest of the budget (as was done in Bretherton et al., 2005 and Muller & Held, 2012). An important result is that while the domain FMSE variance was relatively constant during convective aggregation (see Figure 3.10, right panel), it decreased slightly during convective merging, and then increased to its original value once all clusters merged into the single cluster (see Figure 3.10, left panel). This suggests that negative feedbacks are dominant during convective merging, which is consistent with the hypothesis that dry grid cells in the merging zone become wet as a result of moisture advection.

Each term in (5) is shown in Figure 3.11, top panel, for the medium domain case during convective merging. We normalize by the domain mean of the FMSE variance,  $\hat{h}^2$  so that that each plotted term is the contribution to the fractional change in the domain-mean FMSE variance. Note that it is expected that all terms are small and roughly in balance during convective merging because the domain mean FMSE variance is constant in the aggregated

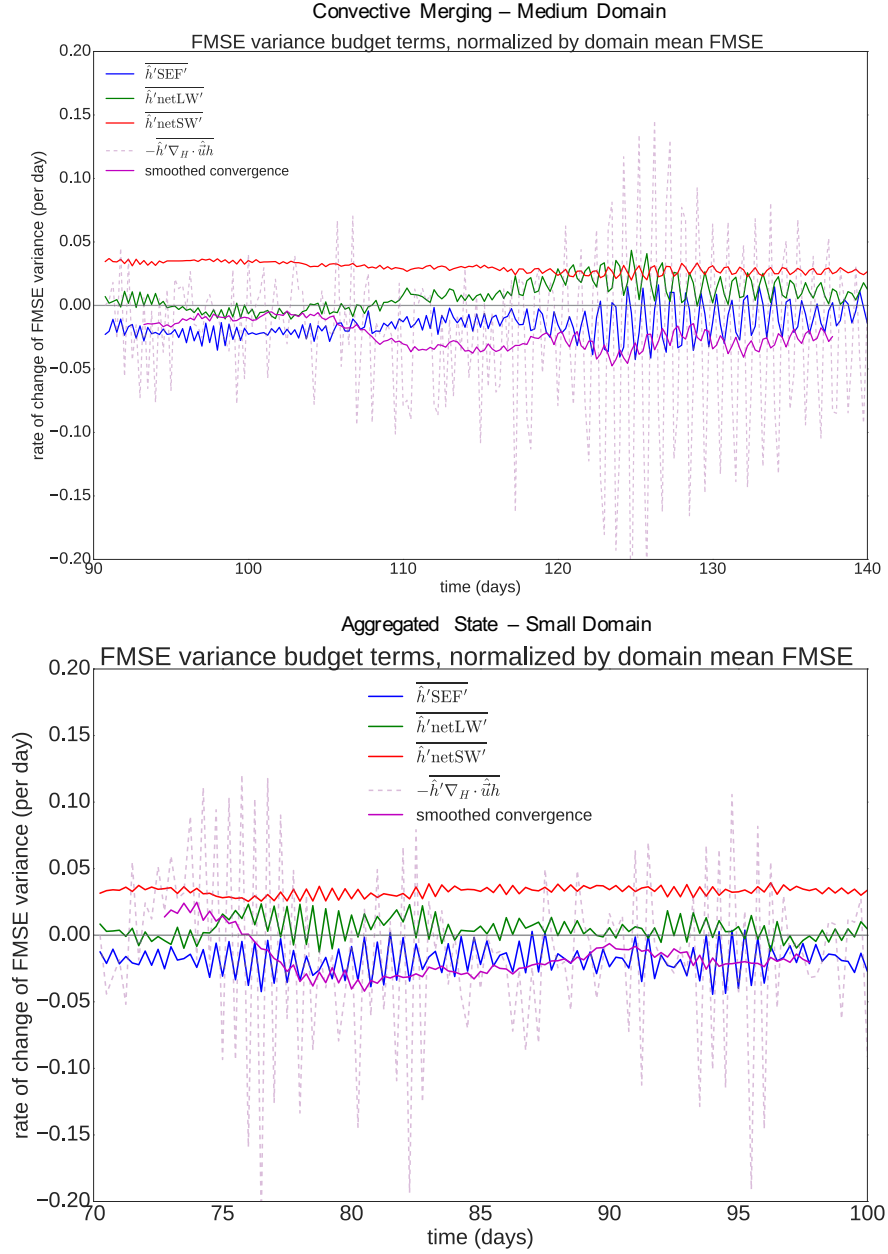


FIGURE 3.11. Left: domain mean FMSE variance budget terms for the medium domain case, plotted between day 90 to day 140. Convective merging occurs between around day 100 and day 125. Right: domain mean FMSE variance budget terms for the small domain case, plotted between day 70 and day 100. The small domain reaches a relatively steady aggregated state around day 75.

state. On the other hand, it seems that the decrease in FMSE variance during convective merging is in part because the domain-mean of the advective term became increasingly more

negative during the convective merging process ( $\sim$  day 110 to day 120), while other terms stayed relatively constant or close to zero.

Furthermore, this seems to be unique to the convective merging process, as the FMSE variance budget terms during convective aggregation did not display this behavior (see Figure 3.11, bottom panel). An unexpected result is that the longwave term became slightly negative during the early stages of convective merging (day 90 to 110), and gradually increased until the single cluster formed (day 120). Thus, in early stages of convective merging, the spatial variability of longwave radiative heating made dry areas more wet, and wet areas more dry. We suspect that this is because as the convective clusters began to move toward each other, the areas of the domain that were previously covered by deep convection became relatively devoid of deep clouds, and as a result, cooled more effectively by radiative longwave emission. Radiative cooling is then balanced by subsidence, which is a drying effect. Likewise, clear-sky areas became covered by deep clouds, and as a result, cooled less effectively by radiative longwave emission. Less radiative cooling means there will be less subsidence, which is an anomalous moistening effect.

Overall, the precise mechanism responsible for the convective merging in our simulations is unclear, but our results suggest that the circulations produced by the two convective clusters interact in a way that favors merging of adjacent clusters by low-level advection of moisture. We leave further investigation of the convective merging process to future work.

Next, we highlight differences between the single cluster in all three cases that are not readily apparent from the previously shown results. To highlight these differences, we calculated profiles as a function of radial distance from the convective cluster, and additionally obtained vertical profiles by compositing on the convective region and dry, subsiding region.

We will focus on showing changes in the convective region and the surrounding dry region that suggest the size of the domain is approaching a scale at which multiple convective clusters may exist in the domain (i.e. the natural spatial scale of convective aggregation).

## 4. RADIAL PROFILES

### 4.1. TIME AVERAGING METHODOLOGY

Before showing the radial profiles, we describe our time averaging methodology. For the small and medium domain case, we averaged over the last 5 and 10 days of the simulation, respectively. For the large domain case, we averaged over the last 3 days, before the smaller cluster formed in the domain (day 177 to 180). The reason for using a shorter averaging period for larger domain size was to reduce the required computer memory during the analysis (there are approximately 67 million points per time sample in the case of the largest domain). Importantly, though, the radial profiles are not highly sensitive to the averaging period in the range of 3 to 10 days. As the aggregated state has longer period fluctuations with increasing domain size (see Figure 3.1), it is possible that a longer averaging period could yield different results.

The radial structure of the time-averaged aggregated state is now described for each domain case. The fields were binned according to radial distance from the convective region center. A fixed bin-width of 5 km is used in all cases. To find the convective region center, we first average the PW field over 48 x 48 km blocks, and then define the center of the convective region to be coordinates of the block with maximum precipitable water. The radial distance was normalized by the domain width to facilitate comparison between all of the cases. In the following, the domain-normalized radial distance is denoted by  $\hat{r}$ .

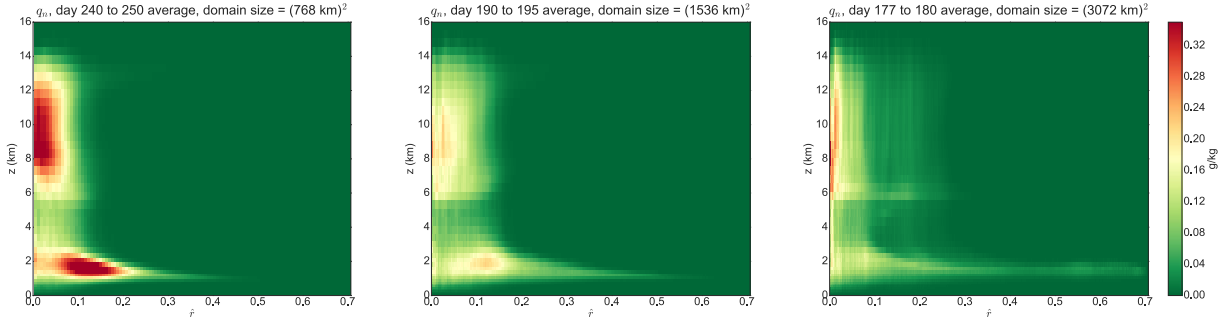


FIGURE 4.1. Radial profiles ( $z$ - $\hat{r}$ ) of non-precipitating condensate (g/kg), time averaged at the end of simulation for the small, medium and large domain case (left to right, respectively).  $\hat{r}$  is the normalized radial distance from the convection region center. For example, for the small domain case,  $\hat{r} = 0.1$  corresponds to  $r = 78.8$  km, whereas for the medium domain case,  $\hat{r} = 0.1$  corresponds to  $r = 153.6$  km. The bin-width is the same in all cases, however, and is equal to 5 km.

## 4.2. CLOUDS & WATER VAPOR

The radial structure of the clouds and the water vapor is described first. The non-precipitating condensate (liquid water and ice),  $q_n$ , is shown in Figure 4.1. Far from the convective cluster there is no deep convection, with a thin layer of clouds capping the boundary layer, while close to the convective region center there are clouds extending up to around  $z = 14$  km. In these simulations, the deep convection extends almost up to the tropopause, which is generally around  $z = 15$  km (see Figure 4.2; we later discuss the reasons for the apparent increase in tropopause height). Approaching the convectively active region ( $\hat{r} \rightarrow 0.1$ ), the height of maximum condensate increases, signifying increased shallow cumulus activity. We can see that in the range  $0 < \hat{r} < 0.1$ , the cloud layers can be divided into three distinct layers: a shallow cumulus layer ( $\sim 1$  to 3 km), a thin mid-level layer ( $\sim 3$  to 6 km) and a deep convection layer ( $\sim 6$  to 14 km). The large domain cases differs from the other two domain cases in that the condensate is more radially diffused throughout the mid and deep convective layers. For example, at around  $\hat{r} = 0.2$  and between  $z = 3$  to 14 km,  $q_n \approx 0$

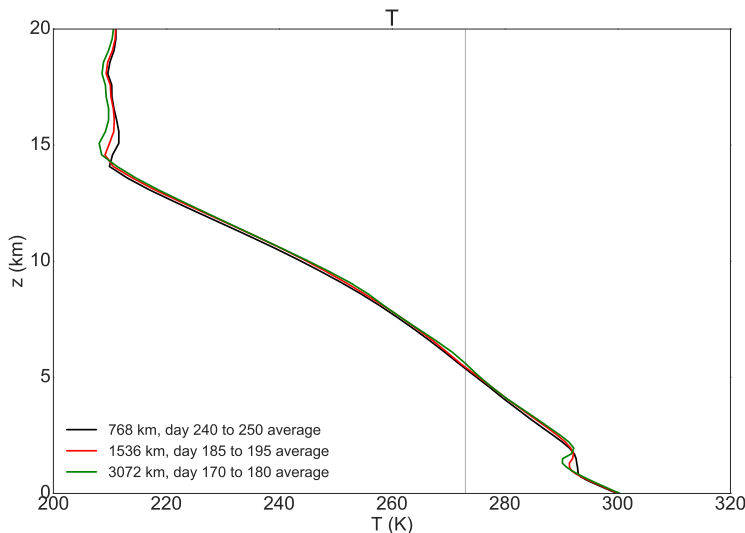


FIGURE 4.2. Temperature profiles for the small (black), medium (red), and large (green) domain cases. The grey line denotes  $0^\circ\text{C}$ .

g/kg in the smaller domain cases, while in the large domain case  $q_n \approx 0.05$  g/kg. The radial broadening of the convective region with domain size can also be seen in the precipitation field (see Figure 4.3, top panel). Note that almost no precipitation falls far from the convective region ( $\hat{r} > 0.3$ ), but that the spatial variance of precipitation increased with domain size.

Another important difference between the domain cases is that there is more low-level condensate far from the convective region with increasing domain size, and there is a mid-level peak in condensate at  $z = 6$  km and  $0.1 < \hat{r} < 0.2$  in the large domain case. The increase in low cloud amount and the mid-level peak in cloud amount can be seen more clearly in profiles of cloud fraction (see Figure 4.4). The increase in low cloud amount is consistent with a deeper, more humid boundary layer, as seen previously. Reasons for the mid-level peak in cloud fraction will be discussed later.

Radial profiles of relative humidity are shown in Figure 4.5. Note that the peak in condensate at the mid-levels coincides with a peak in relative humidity, and the mid-level

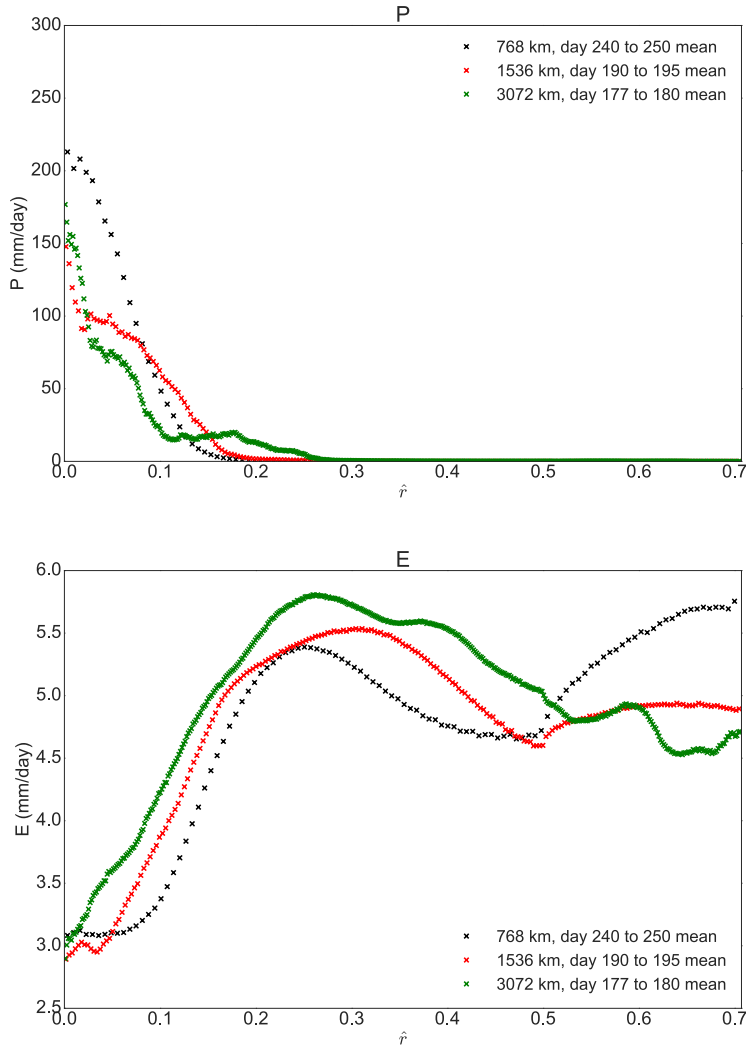


FIGURE 4.3. Top: radial profiles of precipitation,  $P$  (mm/day), for the small (black), medium (red), and large (green) domain cases. Bottom: same as top, except for surface evaporation,  $E$  (mm/day).

relative humidity peak extends further into the dry region with increasing domain size. The high relative humidity at  $z = 14$  km also coincides with a peak in the high cloud fraction (see Figure 4.4). This suggests that clouds are contributing to mid and upper tropospheric moistening, and the mid-level moistening became enhanced with increasing domain size. The extremely dry free troposphere far from the convective cluster ( $\sim 15\%$  RH) is due to subsidence throughout this entire region (shown later), and is consistent with

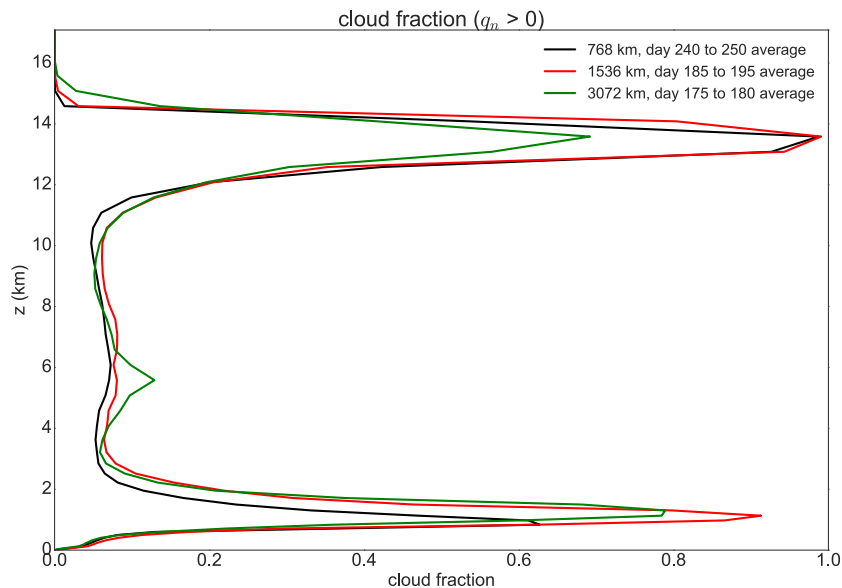


FIGURE 4.4. Cloud fraction profiles for the small (black), medium (red), and large (green) domain cases. Cloudy grid points are classified as those that have positive non-precipitating condensate,  $q_n > 0$ .

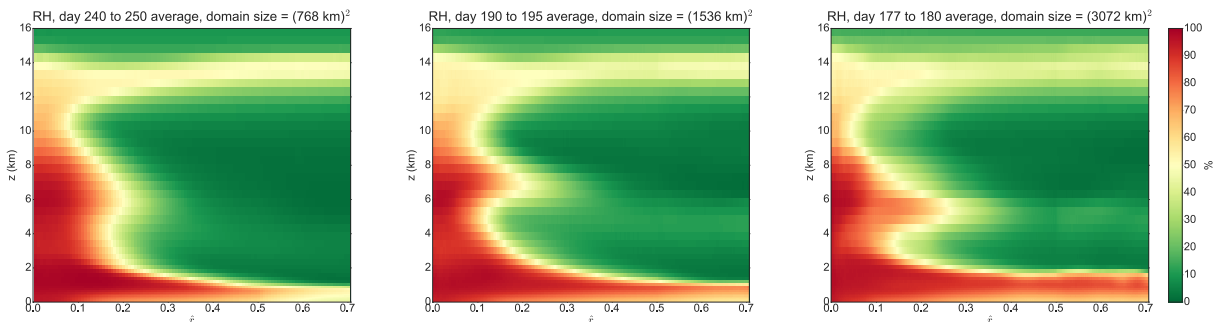


FIGURE 4.5. As in 4.1, except for relative humidity, RH (%).

previous studies of convective aggregation (e.g. Bretherton et al. 2005). Despite the dry free troposphere, however, the boundary layer remains relatively humid far from the convective region ( $\sim 40\%$  RH) with humidity gradually increasing to  $\sim 90\%$  at the convective region center. Additionally, the vertically-integrated water vapor decreases smoothly with respect to radial distance from the convective cluster even though the free troposphere is quite uniformly dry (see Figure 4.6). Thus, the smooth radial decrease in precipitable water in

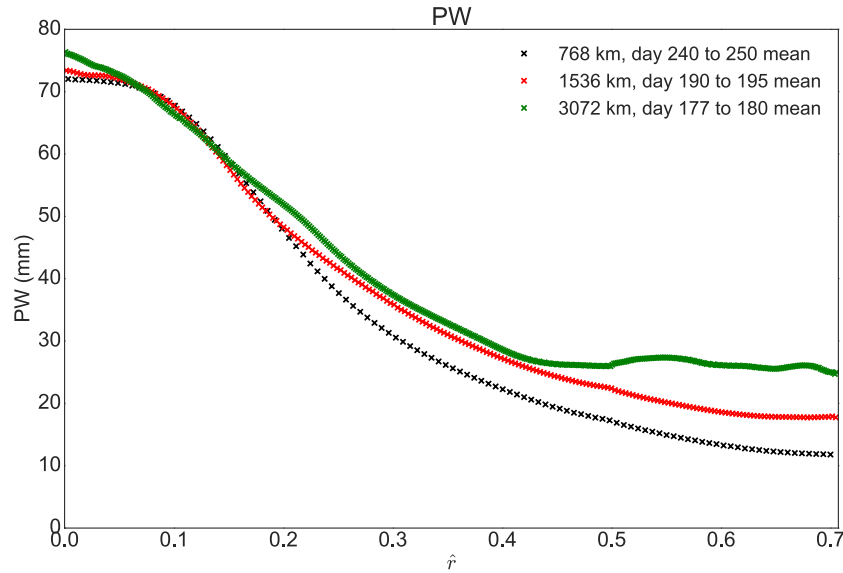


FIGURE 4.6. Radial profile of precipitable water, PW (mm) for the small (black), medium (red), and large (green) domain cases.

the dry region can be mostly attributed to the radial decrease in boundary layer water vapor. From Figure 4.6 we can also see that the domain is more wet with increasing domain size (consistent with Figure 3.1), with the largest increase in precipitable water occurring in the dry region, far from the convective cluster. As we have previously seen that the largest increases in horizontal mean water vapor occur primarily in the boundary layer, and low/mid troposphere (see Figure 3.5), we conclude that the observed increase in domain-mean PW is due to deepening and moistening of the boundary layer in the dry region, as well as low-level and mid-level moistening outside of the convective region. Although the increase in domain-mean PW that occurred with domain size was unexpected, the fact that the moistening occurred mostly outside of the convective region is fairly unsurprising, as the convective region is close to saturation throughout most of the troposphere.

### 4.3. CIRCULATION

The previous results suggest that the middle troposphere became more cloudy and humid with domain size. This suggests that more clouds are detraining in the mid troposphere, as previously discussed. However, moisture advection is also effected by the strength and structure of the circulation associated with the aggregated RCE state. Shown in Figure 4.7 is the streamfunction superimposed onto the radial water vapor field. The definition for the streamfunction,  $\psi_i(z)$ , at radial distance  $r_i$ , where  $i = 0, 1, \dots, N$  and  $N$  is the number of radial bins, is as follows:

$$\psi_i(z) = \frac{\Psi_i(z)}{r_i \Delta r_i} \quad (6)$$

$$\text{where } \Psi_i = \Psi_{i-1} - \rho(z)w_i(z)r_i\Delta r_i \quad (7)$$

$$\text{with } \Psi_0 = 0$$

This follows from the azimuthally averaged continuity equation in radial coordinates:

$$\frac{\partial(\rho r u)}{\partial r} + \frac{\partial(\rho r w)}{\partial z} = 0 \quad (8)$$

The averaged continuity equation will then be satisfied if we define  $\Psi$  as:

$$\frac{\partial \Psi}{\partial z} = \rho r u \quad (9)$$

$$\frac{\partial \Psi}{\partial r} = -\rho r w \quad (10)$$

Taking the forward difference discretization of (10) yields (7). Note that we divide  $\Psi$  by  $r_i \Delta r_i$  to get the streamfunction  $\psi$  in the typical mass flux units  $\text{kg m}^{-2} \text{s}^{-1}$ . Since  $r_i \Delta r_i$  is

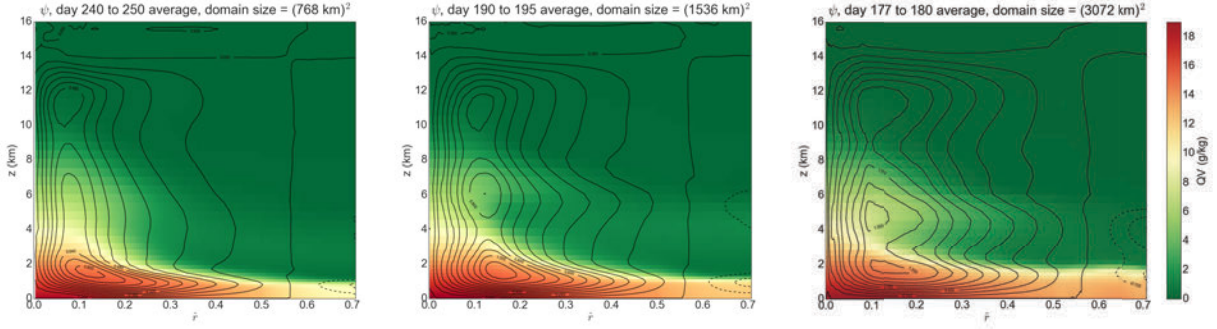


FIGURE 4.7. As in 4.1, except for water vapor mixing ratio,  $q_v$  (g/kg) and the streamfunction,  $\psi$  ( $\text{kg m}^{-2} \text{s}^{-1}$ ).  $q_v$  is indicated by the color shading, and  $\psi$  is indicated by the black contour lines. The solid contour lines are positive and indicate clockwise flow, whereas the dashed contour lines are negative and indicate counterclockwise flow.

proportional to the area of a thin disk at radial distance  $r_i$ , we can interpret  $\psi$  as the mass flux per unit area at radial distance  $r_i$ , whereas  $\Psi$  is the total mass flux at radial distance  $r_i$ . Note that we are free to set  $\Psi_0 = 0$  without changing the physical interpretation of the streamfunction, because the mass flux field is defined in terms of derivatives of  $\Psi$ .

The overall structure of the circulation is consistent with previous studies of convective aggregation (Bretherton et al. 2005; Muller & Held 2012; Jeevanjee & Romps; 2013), who found strong inflow (air flowing toward  $\hat{r} = 0$ ) in the boundary layer and strong outflow (air flowing away from  $\hat{r} = 0$ ) at the tropopause. An unexpected result, however, was the presence of multiple circulation cells above the low-level boundary layer cell (above  $\sim 0$  to 2 km). In particular, there is a weak mid-level cell ( $\sim 2$  to 8 km) and an additional upper-level cell ( $\sim 8$  to 14 km). It is also interesting that the mid-level cell becomes stronger with increasing domain size. Profiles of the radial velocity,  $u_r$ , are shown in Figure 4.8 so that the radial part of the circulation can be seen more easily. We can see that the mid-level cell is associated with mid-level outflow, which evidently transports water vapor from the convective region to the dry, subsiding region (see water vapor maxima at around

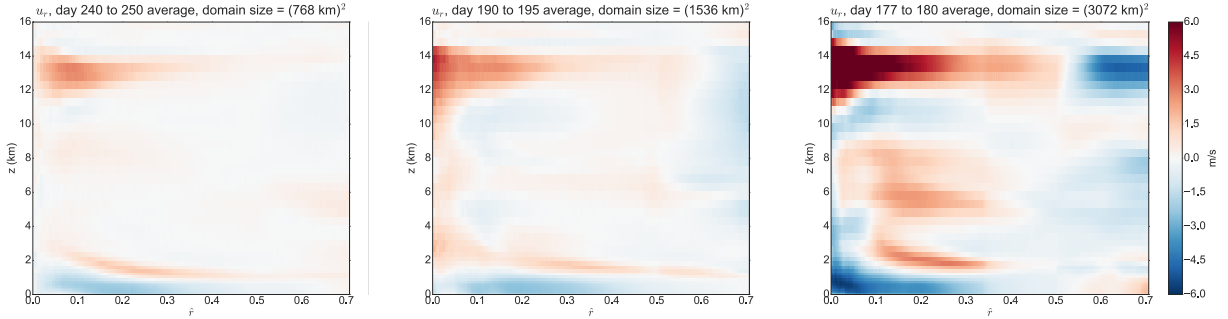


FIGURE 4.8. As in 4.1, except for radial velocity (m/s). Positive radial velocity means flow away from the convective region (toward  $\hat{r} = 0.7$ ), and negative velocity means flow toward the convective region (toward  $\hat{r} = 0$ ).

$z = 6$  km and  $\hat{r} = 0.3$  in Figure 4.7, and also the previously shown mid-level peak in RH in Figure 4.5). There is also a thin outflow layer above the boundary layer, which has been documented in previous studies of convective aggregation (Bretherton et al. 2005; Muller & Held 2012; Jeevanjee & Romps; 2013). The mid-level outflow becomes much more prominent with increasing domain size, which is consistent with the more developed mid-level circulation cell seen previously. Multiple circulation cells were found in CRM simulations of RCE by Posselt et al (2008), however there has been little discussion of this type of circulation structure and the associated mid-level outflow in previous studies of convective aggregation. Although the boundary layer inflow and upper level outflow are responsible for most of the mass transport, the mid-level outflow seems to be increasingly more important in transporting mass and moisture as the domain size is increased. This seems to be associated with important changes to the aggregated RCE state, which will be discussed in more detail in the following sections.

#### 4.4. STABILITY & BUOYANCY

An interesting result is that the mid-level peak in cloud fraction and relative humidity roughly coincides with the freezing level of 5 km (see Figure 4.2). The detrainment of clouds at the freezing level and associated peak in cloud amount is consistent with studies of observations of the tropical warm pool (TOGA COARE) by Johnson et al. (1996, 1999). In these studies, it was found that the combined effect of melting of ice below the  $0^{\circ}\text{C}$  level and the freezing of water above the  $0^{\circ}\text{C}$  level, resulted in the formation of a stable layer because the melting cools the environment, whereas the freezing warms the environment. It was additionally found that the stable layer affected the cloud population. In particular, it was found that the stable layer would tend to inhibit the growth of certain cumulus clouds and promote detrainment, which would result in a peak in the frequency distribution of cloud top height near the  $0^{\circ}\text{C}$  level (Johnson et al., 1999). See Figure 4.9 for a simple schematic that illustrates the effect of the freezing level on the cloud population. Note that the schematic is quite consistent with the previously seen radial plots of non-precipitating condensate.

In our simulations, a mid-level stable layer is visible in radial plots of the buoyancy frequency (see Figure 4.10). The stable layer extends into the dry region because horizontal temperature gradients are small. The horizontal temperature gradients are small because there is no rotation in the simulations. With rotation, the coriolis force acts to confine the propagation of gravity waves at a length scale proportional to the Rossby radius of deformation. Therefore, without rotation, as is the case in our simulations, gravity waves can effectively transport horizontal temperature anomalies, and hence, stability anomalies are effectively transported horizontally. This is consistent with observations of the Tropical atmosphere, where the Coriolis parameter is small and horizontal temperature gradients are

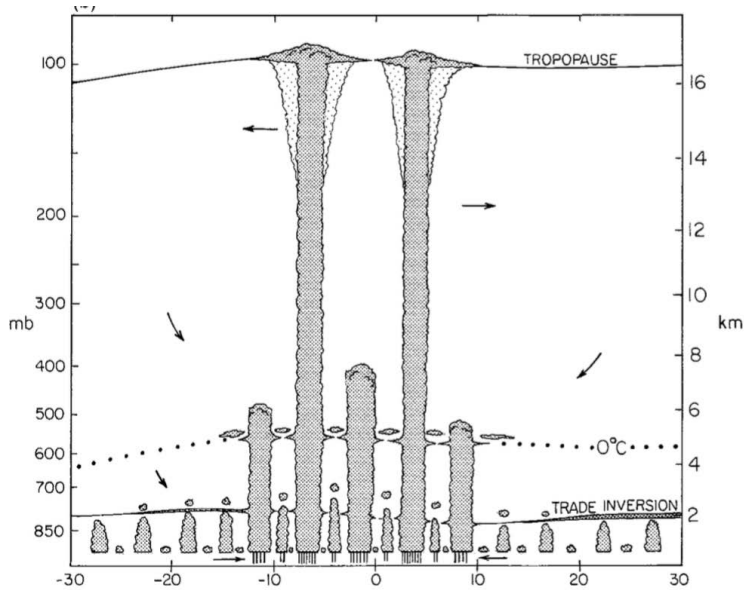


FIGURE 4.9. Schematic from Johnson et al. (1999). The x-axis is latitude. Three stable layers are indicated: the trade inversion, the  $0^{\circ}\text{C}$  level, and the tropopause. There are also three different cloud types indicated: shallow cumulus, cumulus congestus (mid-level detraining clouds), and cumulonimbus (deep convection). The arrows represent the meridional circulation.

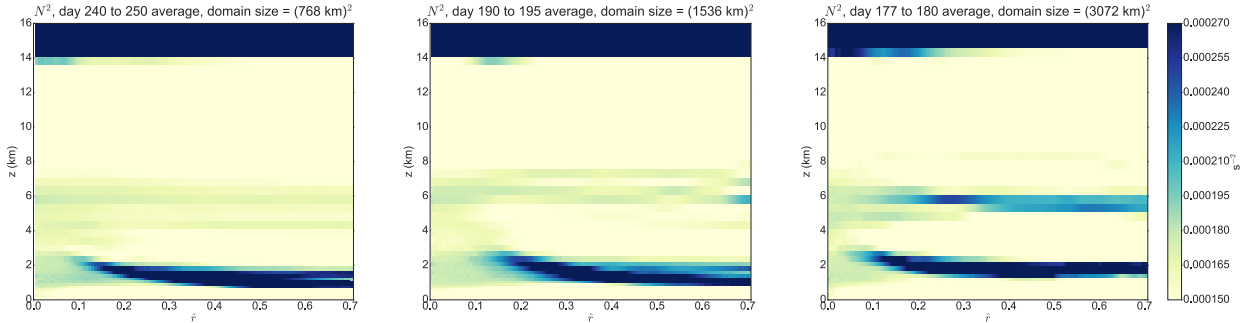


FIGURE 4.10. As in 4.1, except for the buoyancy frequency,  $N^2$  ( $\text{s}^{-1}$ ).

weak. The mid-level detraining of water vapor into the dry region in the simulations likely increases the stability in the dry region as well. Anomalous water vapor in the dry region would tend to warm below the anomaly and cool above the anomaly because water vapor is a strong absorber of infrared radiation. Indeed, there is a radiative cooling anomaly in the mid-levels which coincides with positive anomalies of relative humidity (see Figures 4.19, 4.5, 3.4, right panel, and 4.11, left panel).

It is unclear whether or not the mid-level stable layer is a direct consequence of the previously discussed melting process, as it is not exactly located at  $z = 5$  km (particularly in the medium domain case). However, a time series of the stability shows that there is a positive anomaly in  $\frac{\partial s}{\partial z}$  located close to  $z = 5$  km in both the medium and large domain case (see Figure 4.11, right panel), but then moves upward in time. We hypothesize that the upward migration of this stability anomaly happens because mid-level clouds *begin* detraining around the freezing level, but then continuously detrain until around  $z = 7$  km. The mid-level clouds modify the stability of the environment because they induce a cooling anomaly above the cloud top, and a warming anomaly below cloud base (this can be seen most clearly in Figure 4.11). The cooling anomaly above the cloud top happens because clouds strongly absorb longwave radiation and hence shield the air above the cloud from radiation emitted from warmer underlying air. Likewise, the warming anomaly below cloud the cloud base happens because the cloud effectively shields the air from the overlying cooler air. Thus, we believe that there is in fact a stable located around the freezing level in both cases, but that there is sampling sensitivity because the mid-level clouds modify the mid-level stability in a time varying fashion. In particular, in the medium domain case, we have most likely sampled during a “convective event” when the stable layer at the freezing level is weaker. The fact that the mid-level peak in cloud fraction and relative humidity roughly coincides with the height of this stable layer, suggests that the stable layer has important effects on the cloud population in our simulations (see Figures 4.4, 3.4, and 4.11, right panel). Also note that these effects are more pronounced with increasing domain size.

The peak in mid-level cloud fraction at the freezing level has also been found in CRM simulations of RCE by Posselt et al. (2008) using the Regional Atmospheric Modeling System

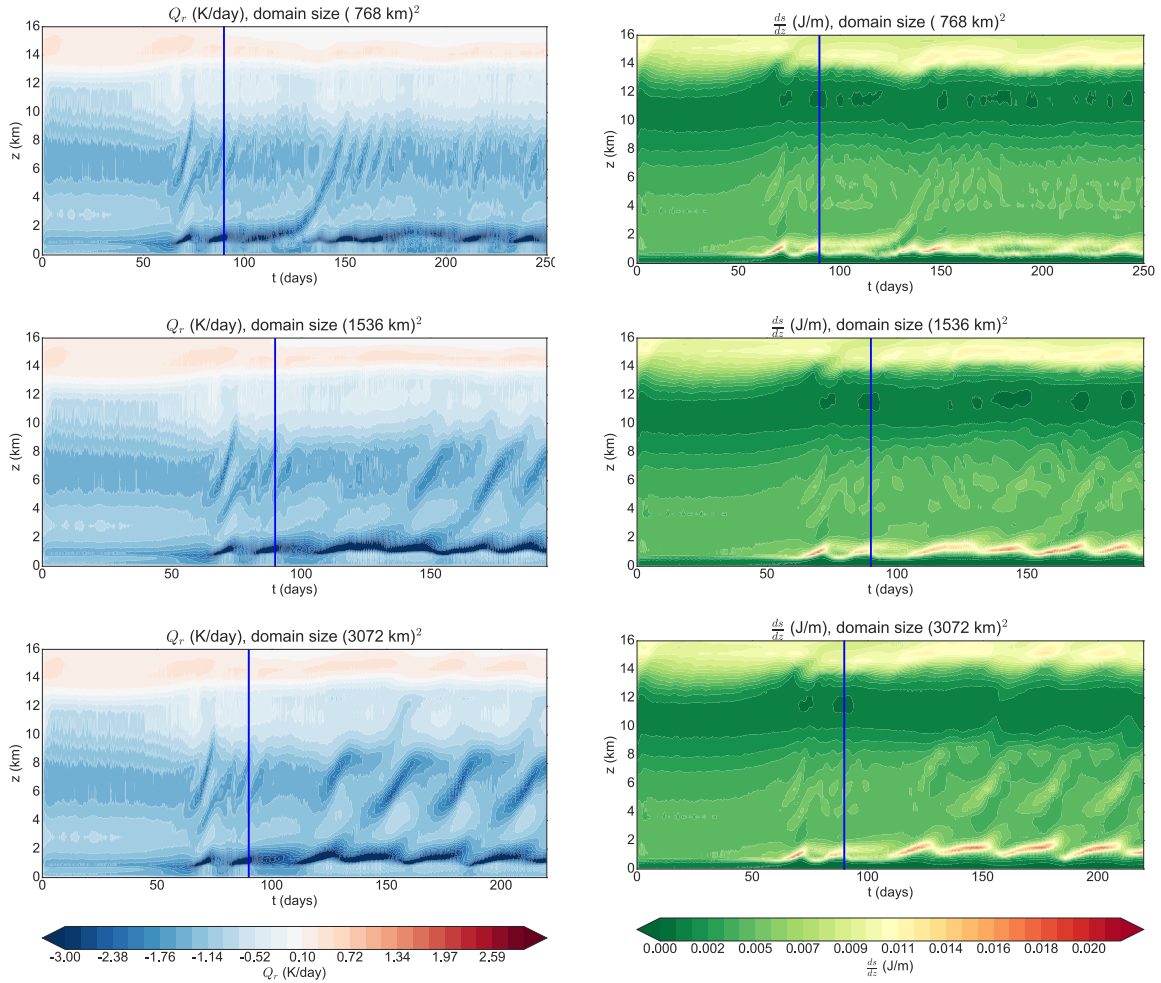


FIGURE 4.11. Hourly time-height cross section of the radiative heating rate,  $Q_r$  (K/day) (left), and the stability,  $\frac{\partial s}{\partial z}$  (J/m) (right), for small domain case (top), medium domain case (middle) and large domain case (bottom).

(RAMS), developed at Colorado State University (Pielke et al., 1992, Cotton et al., 2003). We note that our square domain set-up is different than the bowling-alley domain set-up (9600 x 180 km) used by Posselt et al (2008). It is interesting the mid-level stable layer and peak in cloud fraction are present in the aggregated RCE state, but that they are both sensitive to domain size in our simulations (i.e. both the the mid-level stable layer and peak in cloud fraction are more pronounced with increasing domain size).

In order to further illustrate the effects of the mid-level stable layer on convection, the buoyancy is shown in (Figure 4.12). Here, the buoyancy is given by  $\rho\theta'_v$ , where  $\theta'_v$  is the horizontal anomaly in virtual potential temperature. The virtual potential temperature is given by  $\theta_v = \theta(1 + 0.61q_v - q_l)$ , where  $q_v$  and  $q_l$  are the mixing ratios of water vapor and liquid water, respectively. The virtual potential temperature is equivalent to the potential temperature except that it accounts for the effects of water vapor and liquid water on density. In other words, it is the hypothetical potential temperature a dry parcel of air would have in order to give the same density as the parcel of wet air. Parcels of air accelerate where the buoyancy is positive, and decelerate where the buoyancy is negative so that we can write:

$$\frac{\partial w}{\partial t} \sim \rho\theta'_v \quad (11)$$

Note that, strictly speaking,  $\frac{\partial w}{\partial t}$  is also affected by pressure perturbations, so that the buoyancy represents only a part of the vertical forces that act on parcels of air.

Looking at the buoyancy in the convective region we can see that in the medium domain case there is a buoyancy dipole centered around  $z = 7$  km (at the mid-level stable layer) while in the large domain case there are two buoyancy dipoles in the mid-troposphere, one centered at the freezing level ( $z = 5$  km), and another centered at  $z = 9$  km. It is unclear why the vertical structure of buoyancy becomes increasingly more complex with domain size, but we can see that the lower buoyancy dipole in the large domain case is centered at the freezing level. Note that in the small domain case there is no buoyancy dipole in the mid-troposphere, which suggests that the mid-level stable layer is weaker in the small domain case and in turn does not have significant effects on the convection. The effects of the mid-level stable layer

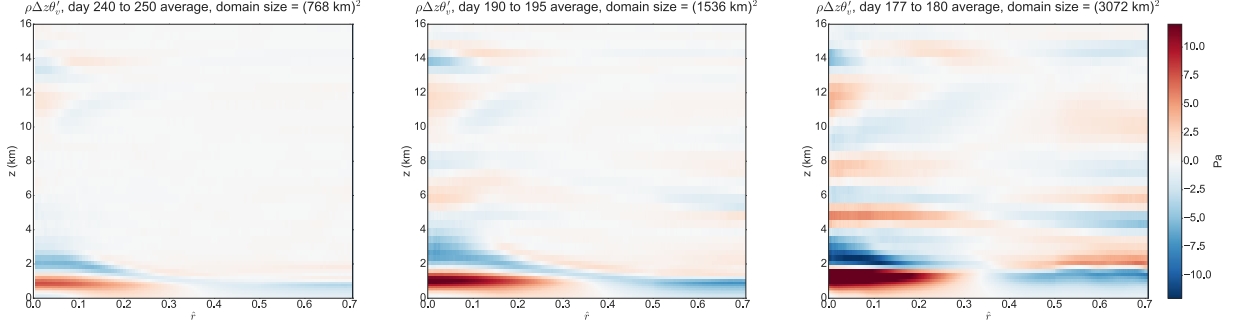


FIGURE 4.12. As in 4.1, except for the buoyancy,  $\rho\Delta z\theta'_v$  (Pa).

can also be seen in the vertical buoyancy flux (see the buoyancy flux dipole in the mid-troposphere in Figure 4.13, top panel). The vertical buoyancy flux is proportional to  $\rho w\theta'_v$ , so that it is a measure of the vertical transport of buoyancy perturbations. Importantly, from (11), we can see that:

$$w \frac{\partial w}{\partial t} \sim \rho w\theta'_v \quad (12)$$

$$\frac{1}{2} \frac{\partial w^2}{\partial t} \sim \rho w\theta'_v \quad (13)$$

In other words, the vertical buoyancy flux is related to the rate of change of vertical kinetic energy, so that the buoyancy flux can be interpreted as the degree of “convective activity”. We discuss this in more detail in the following.

The vertical buoyancy flux is proportional to the rate change of kinetic energy due to buoyancy forces, and so, when averaged over the entire domain, the sum of the domain mean buoyancy flux and the convectively-available potential energy (CAPE) must be conserved because the total energy must be conserved over the entire domain. Thus, the domain mean buoyancy flux is a measure of the rate at which the domain mean CAPE is being consumed by convection. Interestingly, the domain mean buoyancy flux systematically increased with domain size (see Figure 4.14), which suggests that convection consumes the CAPE more

quickly when the domain size is larger. This also suggests that the CAPE is being generated more quickly when the domain size is larger, as the domain mean CAPE is not changing with time so that the convection is in a state of quasi-equilibrium. We hypothesize that the domain mean CAPE is being consumed more quickly because the convective region occupies a greater fraction of the domain when the domain size is larger. Recall that we have previously seen that the non-precipitating condensate in the convective region became more radially diffused with increasing domain size (Figure 4.1), and the region of high surface precipitation spread out with increasing domain size (Figure 4.3). We can also clearly see that the fraction of the domain that is above a low buoyancy flux threshold of  $0.05 \text{ W/m}^2$  increases with domain size (see Figure 4.13, bottom panel). All of these results suggest that the convective region occupies a larger fraction of the domain with domain size. We later show the dynamical radial fields which also suggest that the convective region broadened with domain size.

A final interesting result is that the convective region boundary layer becomes more buoyant with domain size. Note that the spatial variance of buoyancy increases with domain size as well. A reason for this could be because horizontal temperature anomalies are transported less effectively by gravity waves with increasing domain size. With a larger domain size, the time required for a gravity wave to propagate over the entire domain increases. Therefore, horizontal temperature anomalies can build up over time because the gravity wave adjustment time scale is longer. Indeed, it is clear that the horizontal temperature anomalies became larger with increasing domain size, especially in the boundary layer (see Figure 4.17). The systematic increase in convective region buoyancy with domain size can also be seen in the tropospheric mean buoyancy (see Figure 4.15). We hypothesize that

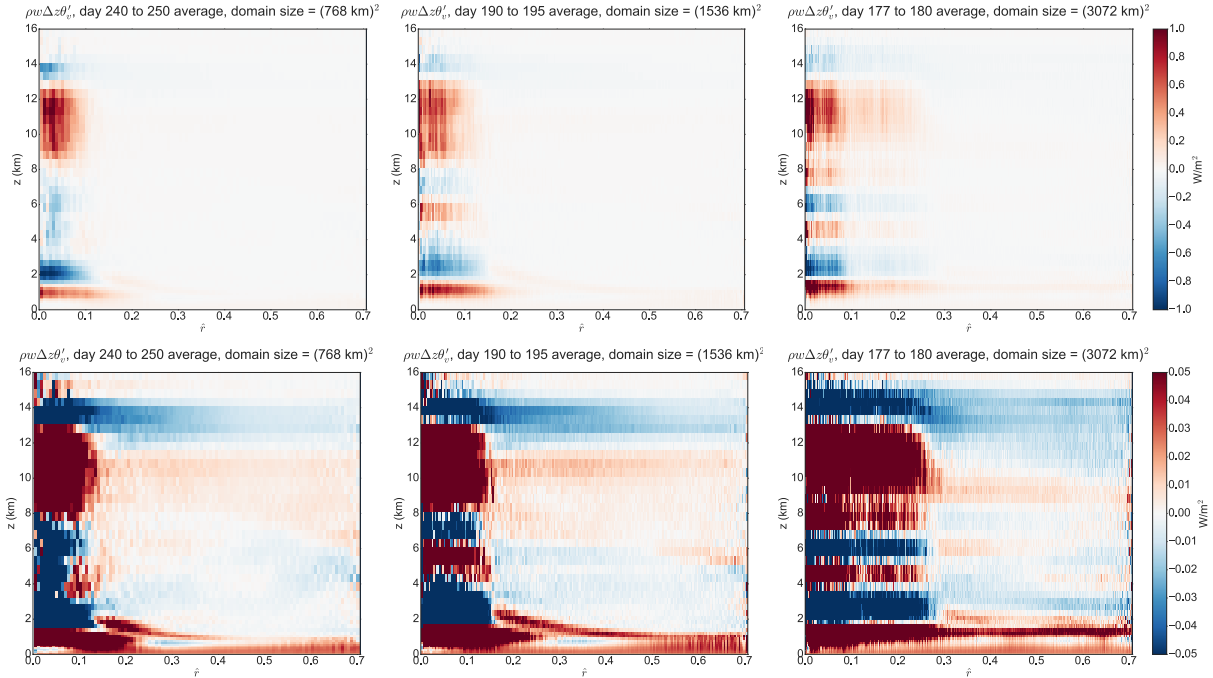


FIGURE 4.13. As in 4.1, except for the buoyancy flux,  $\rho w \Delta z \theta'_v$  ( $\text{W}/\text{m}^2$ ). The top and bottom panels are the same, except for the colorbar range. The top panel colorbar range is  $-1$  to  $1 \text{ W}/\text{m}^2$  and the bottom panel colorbar range is  $-0.05$  to  $0.05 \text{ W}/\text{m}^2$ .

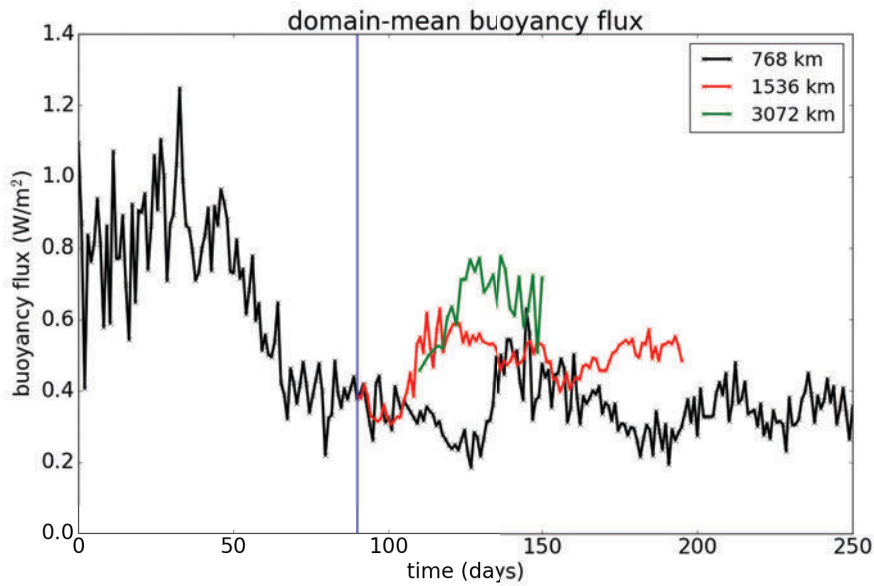


FIGURE 4.14. Time series of domain-mean buoyancy flux,  $\overline{\rho w \Delta z \theta'_v}$  ( $\text{W}/\text{m}^2$ ), for the small (black), medium (red), and large (green) domain case.

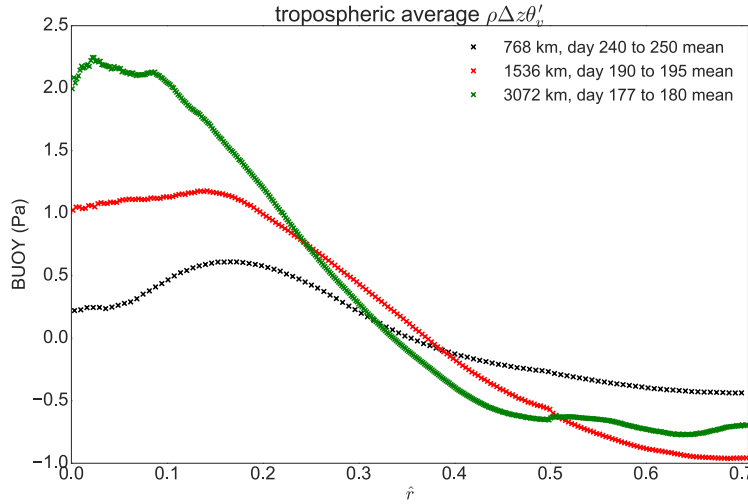


FIGURE 4.15. As in 4.3, except for the tropospheric mean buoyancy (Pa). The tropospheric average is calculated from the surface to  $z = 15$  km.

a boundary layer that has more spatial variance in buoyancy along with higher buoyancy overall, has important effects on the strength and distribution of convection. We return to this point in more detail in Section 6.

#### 4.5. VERTICAL VELOCITY

We now show the vertical velocity,  $w$ , in order to highlight some important differences in  $w$  between the domain cases in  $z$ - $\hat{r}$  space. In particular, we will show that the previous results which show that the convective region broadened with domain size are consistent with the dynamics. We will also show that conditions in the remote environment became more favorable for convection in the large domain case. We will discuss differences in the strength of the convection and the subsidence in more detail in Section 6.

The radial profiles of  $w$  are shown in Figure 4.16. The top panel shows  $w > 0$  and the bottom panel shows  $w < 0$ . In the top panel, we can see that  $w$  has a maximum between  $z = 10$  to  $12$  km in all cases, but the maximum seems to occupy a smaller fraction of the

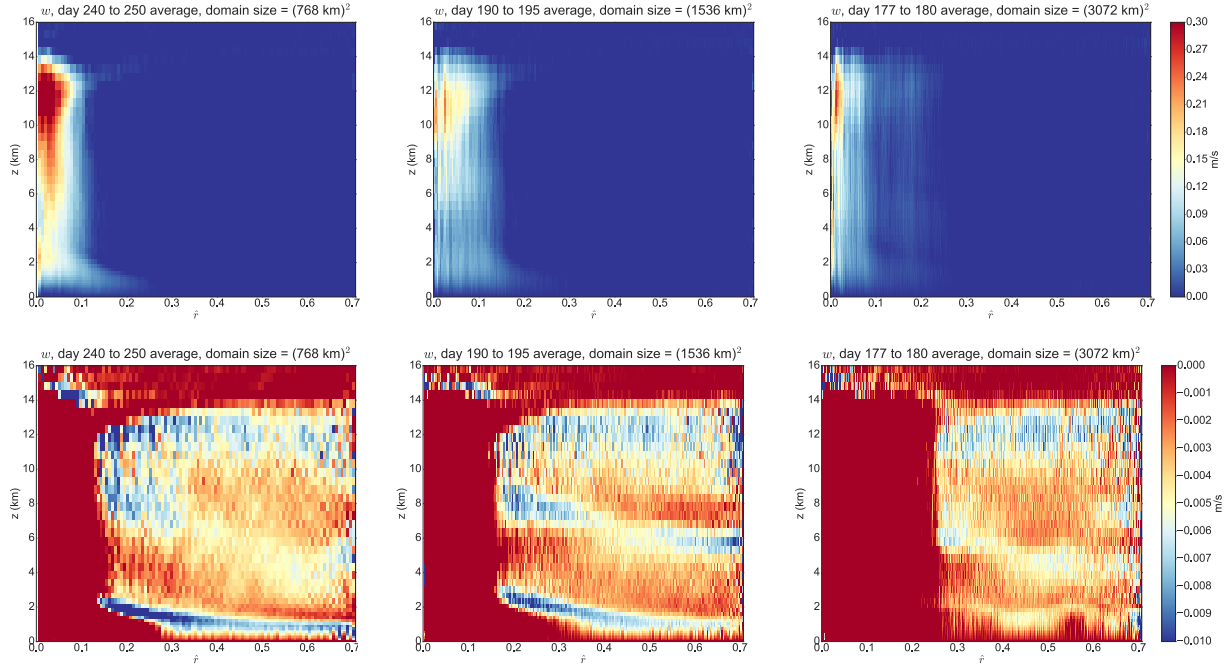


FIGURE 4.16. As in 4.1, except for vertical velocity (m/s). The top panel is positive vertical velocity (dark blue denotes downward motion) and the bottom panel is negative vertical velocity (dark red denotes upward motion). Note that the top colorbar ranges from 0 to 0.3 m/s while the bottom colorbar ranges from 0 to -0.01 m/s.

domain with increasing domain size. Additionally, it is clear that a larger fraction of weaker vertical velocities occupy the domain with increasing domain size. This can also be seen in the bottom panel as a widening of the region with  $w > 0$ , which goes from approximately  $0 < \hat{r} < 0.1$  in the small domain case, to  $0 < \hat{r} < 0.2$  in the large domain case.

Another important feature of the  $w$  profiles is the strong subsiding layer above the boundary layer (around 2 km) in the bottom panel. This is consistent with previous studies of convective aggregation, wherein strong radiative cooling at low cloud tops drove strong subsidence (e.g. Muller & Held 2012). Also note that the magnitude of this subsidence is similar throughout most of the troposphere, except for the subsidence into the boundary layer. This is because in clear-sky areas where horizontal temperature gradients are weak (see Figure 4.17), the radiative cooling by water vapor is generally balanced by adiabatic warming by

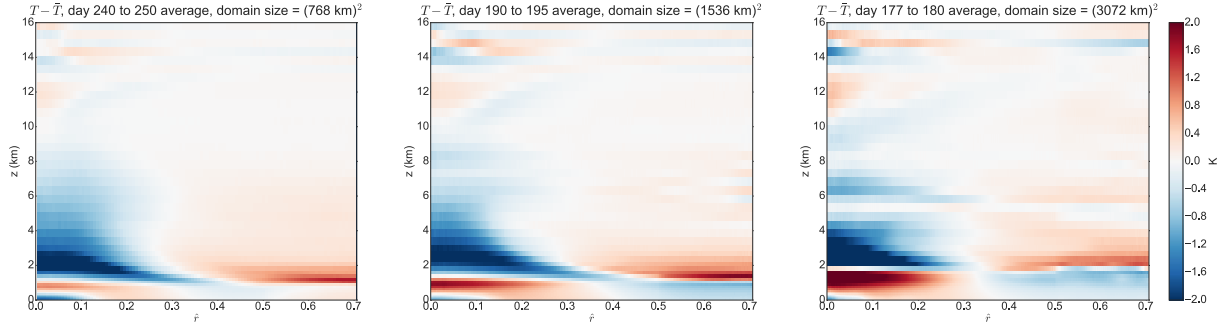


FIGURE 4.17. As in 4.1, except of the horizontal temperature anomaly  $T - \bar{T}$  (K). Note that  $\bar{T}$  is the horizontal mean temperature at a given height.

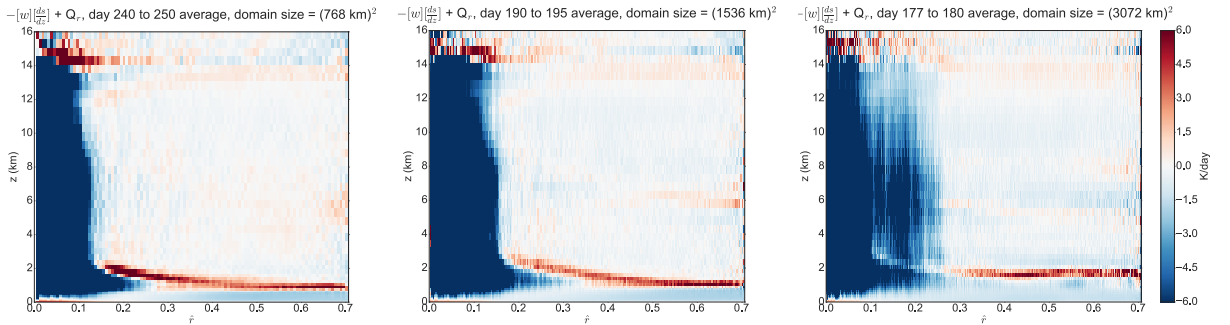


FIGURE 4.18. As in 4.1, except for the sum of adiabatic warming and radiative heating,  $-w \frac{\partial s}{\partial z} + Q_r$  (K/day).

subsidence (see Figure 4.18). This is a well-known balance that holds very well in both simulations of the tropical atmosphere, as well as in observations. Since the water vapor mixing ratio in the dry region free troposphere is not drastically changing with domain size, the radiative cooling and hence subsidence does not change drastically (see Figure 4.19 for radial profiles of the radiative heating rate). Note that the balance clearly does not hold in the convective region because there is both convective and condensation heating occurring there. The balance also does not hold at the top of the boundary layer because low cloud condensate is evaporating there (the excess adiabatic warming must be balanced by evaporative cooling). Recall that we have previously discussed that the boundary layer, and lower/mid troposphere is becoming more wet with increasing domain size. Evidently, the

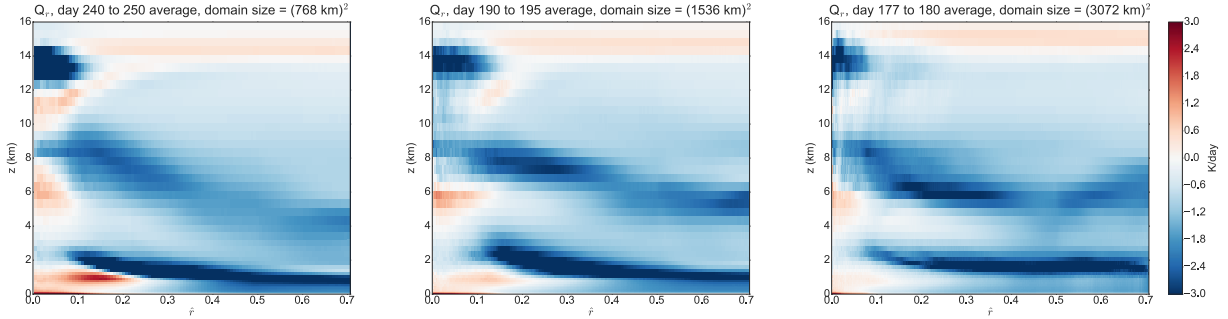


FIGURE 4.19. As in 4.1, except for the radiative heating rate,  $Q_r$  (K/day).

free tropospheric moistening does not drastically change the radiative cooling, otherwise we would see large changes in the subsidence in the free troposphere. However, while we don't see changes in the free tropospheric subsidence, a striking difference is in the large domain case, where the subsidence into the boundary layer is on average weaker by about a factor of four. Furthermore, the slight upward bulge in the subsidence profile between  $0.5 < \hat{r} < 0.6$ , suggests the initiation of convection there. Indeed, recall that when the large domain simulation was run for an extended period of time (day 180 to 220), a second smaller convective cluster formed far from the large convective cluster.

The above results can also be seen in radial profiles of tropospheric averaged  $w$ . The edge of the convective region extends from  $\hat{r} = 0.2$  in the small domain case to  $\hat{r} = 0.25$  in the large domain case, indicating a broadening of the convective region (see Figure 4.20, top panel). At intermediate distances from the convective cluster, the magnitude of tropospheric averaged subsidence is similar across all cases (see Figure 4.20, bottom panel)). However, there are differences in subsidence far from the convective region ( $0.6 < \hat{r} < 0.7$ ). In all cases, the subsidence is weaker far from the convective cluster (indicated by the "U-shaped" subsidence profile), but is generally more weak at a given  $0.6 < \hat{r} < 0.7$  with increasing domain size. Note that in the large domain case, the subsidence reaches a local minimum

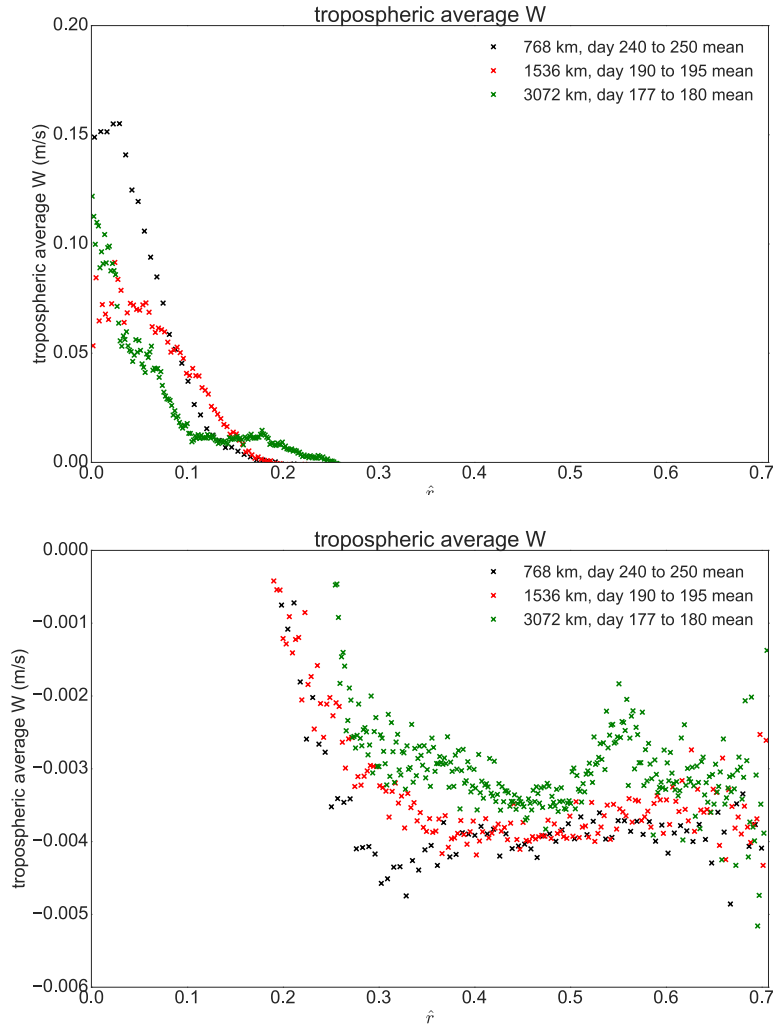


FIGURE 4.20. Top: radial profiles of tropospheric averaged  $w$  (m/s) for  $w > 0$ , for the small (black), medium (red), and large (green) domain cases. Bottom: same as top, except for  $w < 0$ . Note the difference in the y-axis range between the two plots:  $0 < w < 0.2$  m/s for the top panel, while  $-0.006 < w < 0$  m/s for the bottom panel.

at around  $\hat{r} \approx 0.6$ , but then increases as  $\hat{r} \rightarrow 0.7$ . We interpret this local minimum of subsidence as the “edge” of the large-scale circulation generated by the convective cluster. Note that an interesting result is that the subsidence increases as  $\hat{r} \rightarrow 0.7$  for the large domain case. As we have previously shown, when the large domain simulation was run for an extended period of time, a small convective cluster eventually formed far from the large convective cluster. We interpret the decreased subsidence at  $\hat{r} \approx 0.6$  along with the

increase in subsidence  $0.6 < \hat{r} < 0.7$ , as weak convection occurring at the edge of the large-scale circulation ( $\hat{r} \approx 0.6$ ), which in turn enhances the compensating subsidence into the boundary layer far from the convective region.

Overall, we have shown that interesting changes to the aggregated RCE state occur with increasing domain size. Importantly, the outflow and cloud detrainment around the freezing level is enhanced, as indicated by peaks in mid-level humidity and radial velocity around  $z = 6$  km. This is associated with a broadening of the convective region, i.e., that the mesoscale convective region occupies a greater fraction of the domain with increasing domain size. The free tropospheric subsidence in the dry region seems to be approximately invariant with domain size because the radiative cooling in the dry region does not change drastically, while the subsidence into the boundary layer decreases with domain size. Furthermore, we have shown that, in the largest domain case, conditions far from the convective cluster became more favorable for convection, suggesting the domain size is approaching a scale at which multiple convective clusters can exist in the domain. Next, we look more closely at the strength and the structure of the convection and subsidence by showing vertical composites of the convective region and the dry, subsiding region. In particular, we show results that point to a physical mechanism for the increased mid-level outflow, the broadening of the convective region, and the enhanced convective conditions far from the convective cluster which all occur with increasing domain size.

## 5. CONVECTIVE REGION AND SUBSIDING REGION COMPOSITES

### 5.1. COMPOSITING METHODOLOGY

Previous results suggested that there are interesting differences in the vertical and radial structure of the time-averaged aggregated RCE state between the domain cases. In particular, the previous results suggested that the convective region broadened with increasing domain size. This is an important result because it shows that the spatial scale of convective region changed with domain size, however the dynamical reasons behind such a change are not clear. Furthermore, it is not clear why this would occur with increasing domain size. Therefore, in the following analysis, we divide the domain into a convective region and a convection-free region in order to explore the differences in the strength and structure of the convection and subsidence in more detail. In particular, we highlight differences in the convection and convection-free region which explain the convective broadening which occurred with increasing domain size.

First, to show mesoscale ( $\sim 100$  km) features of the convective activity, the time-averaged vertical velocity field was averaged over  $48 \times 48$  km blocks at each height. The vertical velocity is averaged over 8 days in each case. We use the same averaging period, so that we can rule out differences in the statistics of the convection that result purely from sampling over a different time period. Convective blocks are then classified as those that have  $w > w_c = 0.01$  m/s and convection-free blocks as those that have  $w < w_c = 0.01$  m/s. The value of  $w_c$  was chosen by visual inspection of the block-averaged vertical velocity field. In general, smaller values of  $w_c$  result in inclusion of dry blocks in the convective region composite, whereas setting  $w_c = 0.01$  m/s resulted in inclusion of only wet blocks in all cases (see Figure 5.2, right panel). Composites are then obtained for different variables by

averaging the fields over both convective and convection-free blocks at each height. This yields a profile for the mesoscale convective region and convection-free region. The analysis was also performed without block-averaging using  $w_c = 0.3$  m/s, which captured smaller scale features of convective cores, rather than features of the entire wet region as a whole (see Figure 5.1 for a comparison of the two types of composites for the small domain case).

Note that the block-averaging is useful because it smooths out the effect of strong, moist convective downdrafts in the vicinity of strong convective cores. This can be seen in Figure 5.2, where the negative time-averaged vertical velocities generally have lower relative humidity after block-averaging is performed. An important distinction between the two composites is that, without block-averaging, a moist, convective downdraft contributes to a convection-free composite. Therefore, without block-averaging, it is not accurate to think of the convection-free region as the dry, subsiding region seen previously (e.g.  $\sim 0.2 < \hat{r} < 0.7$  in Figures 4.5 and 4.16), because convectively driven downdrafts are quite humid. In fact, because the convective fractional area without block averaging is so small (shown later), the convection-free composite can generally be interpreted as the domain mean profile (there are, of course, exceptions to this). On the other hand, with block averaging, it is appropriate to think of the convection-free region as the dry, subsiding region. In the following, we use the subscript  $m$  to denote with block-averaging and omit the subscript to denote without block-averaging. We also refer to block-averaged composites as “mesoscale composites” and non block-averaged composites as “core composites”, throughout.

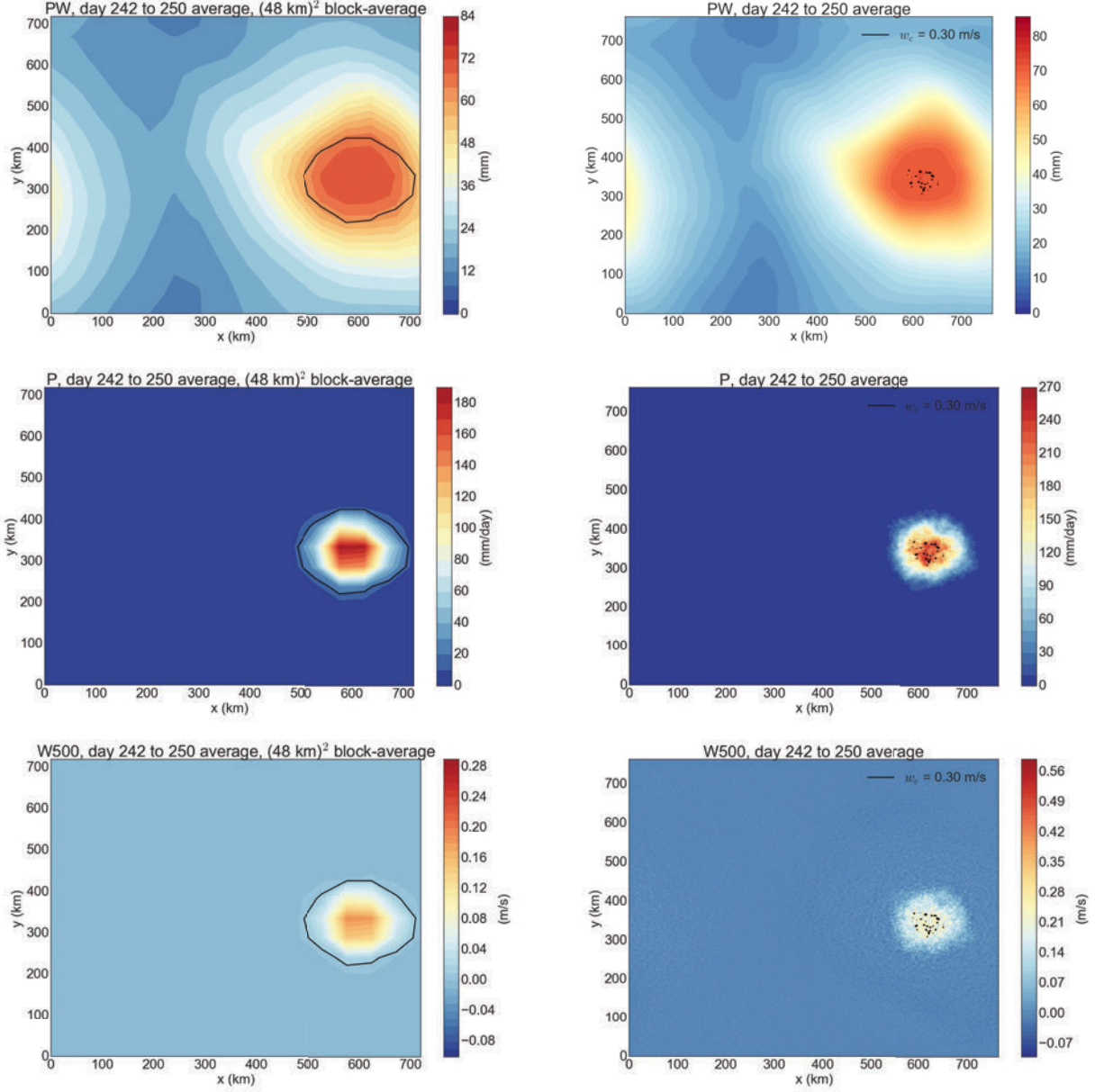


FIGURE 5.1. Top: Precipitable water, PW (mm). Middle: Precipitation, P (mm/day). Bottom:  $w$  at 500 hPa (m/s). The fields are time-averaged over the last 8 days of the simulation. The left plots are block-averaged, and the right plots are without block-averaging. The black contour encloses the regions used for the convective region composite. For example, for the block-averaged composite (left), the grid points with  $w > w_c = 0.01$  m/s are inside the black contour.

## 5.2. CONVECTIVE FRACTIONAL AREA

First, we show the fraction of the domain that is occupied by convection at each height,  $\sigma$ , and similarly, the mesoscale (48 x 48 km block-averaged) convective fractional area,  $\sigma_m$  (see

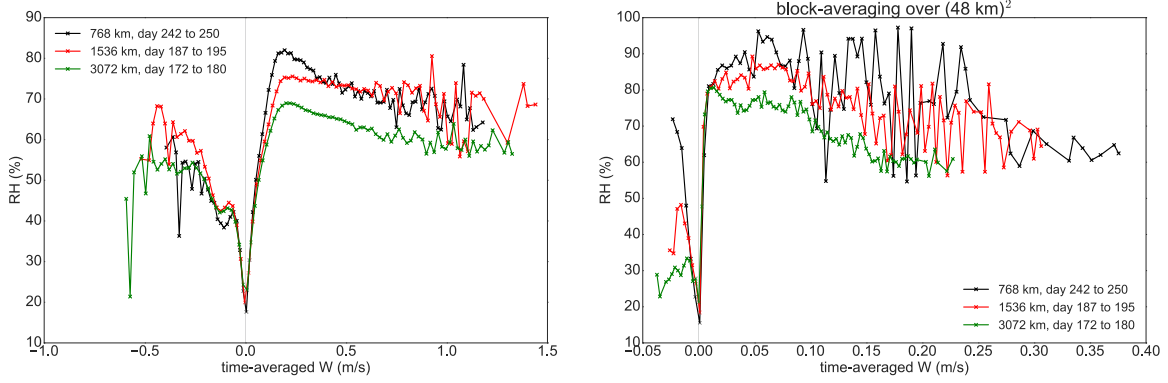


FIGURE 5.2. Left: Relative humidity binned according to time-averaged vertical velocity (m/s), without block-averaging for the large (green), medium (red) and small (black) domain case. Right: same as left, except with block-averaging.

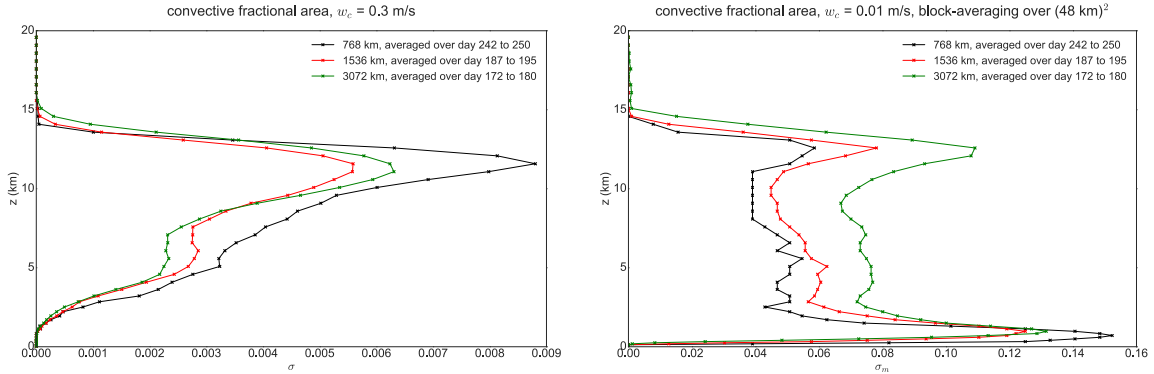


FIGURE 5.3. Left: Vertical profiles of the convective fractional area without block averaging,  $\sigma$ , for the large (green), medium (red) and small (black) domain case. Right: same as left, except for the mesoscale convective fractional area,  $\sigma_m$  (with block-averaging).

Figure 5.3).  $\sigma$  is consistent with expected properties of convective cores: a very small fractional area ( $\approx 0.001$ ) and an upward increasing profile in all cases. On the other hand,  $\sigma_m$  has larger magnitudes (0.04 to 0.15), suggesting broad areas of weak ascent in the convectively active region of the domain. The areas of weak ascent are vertically uniform throughout most of the mid-troposphere, but become large in the lower and upper troposphere. The large values of  $\sigma_m$  in the lower troposphere are consistent with a large fraction of the domain being covered by low clouds (weak convection). With the exception of the boundary layer and

lower tropospheric levels,  $\sigma_m$  increased throughout the troposphere in both the medium and large domain case. On the other hand,  $\sigma$  decreased throughout the domain size with increasing domain size. This is a surprising result as we have previously seen that the convective region boundary layer becomes more buoyant with domain size. With increasing boundary layer buoyancy, it is expected that a larger fraction of strong convective cores would occupy the domain. However, as we have seen that  $\sigma_m$  increased with increasing domain size, it is evident that the fraction of weak convection increased with increasing domain size despite the more buoyant boundary layer. We return to this point later. Note that change in  $\sigma_m$  and  $\sigma$  is sensitive to the sampling period, however, profiles of  $\sigma_m$  at different time periods shows that  $\sigma_m$  is larger with increasing domain size at most points in time.

### 5.3. CONVECTIVE REGION COMPOSITES

The differences in the strength and structure of the convective region are now described. The vertical velocity was composited on the convective region with and without block-averaging (see Figure 5.4). The strength of the mesoscale updraft became weaker with increasing domain size, while the strength of the convective cores remained roughly the same. To reiterate, this is a surprising result as would typically expect the higher buoyancy in the boundary layer to result in stronger convection. We attempt to explain this unexpected result in the following.

It seems that the weakening of the mesoscale convection is in part due to an increase in frequency of weak convection ( $0 < w < 0.3$ ) and an increase in downdraft strength (see Figure 5.5). Note that there is a higher frequency of larger magnitude negative velocities, indicating an increase in downdraft strength. This is additionally supported by an increase

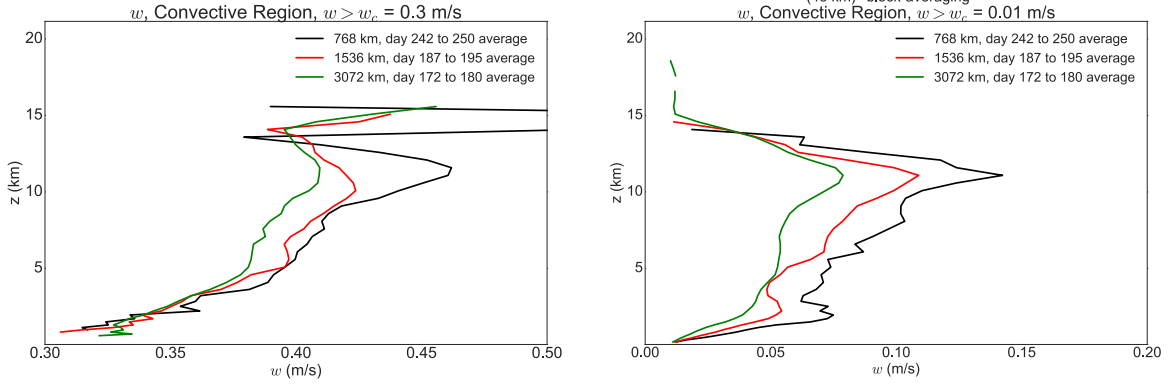


FIGURE 5.4. Left: Vertical profile of the vertical velocity composited on the convective core region (without block-averaging), for the large (green), medium (red) and small (black) domain case. Right: same as left, except for the mesoscale convective region (with block-averaging).

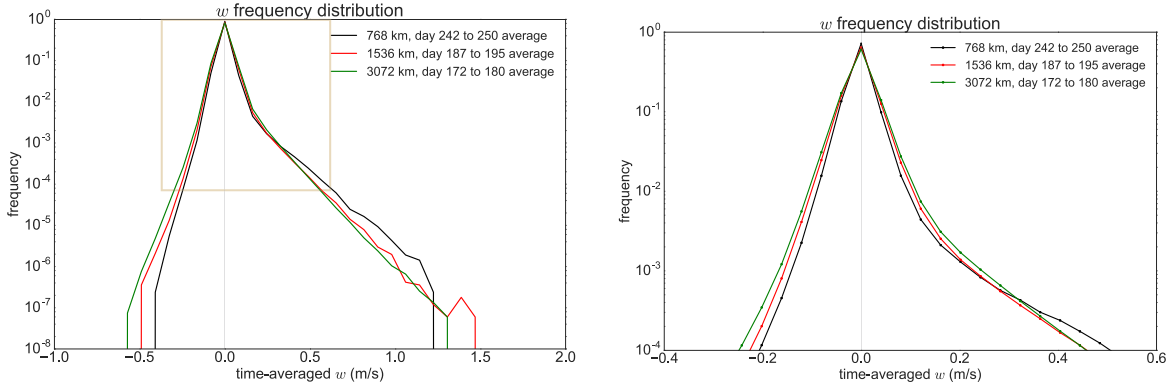


FIGURE 5.5. Left: the frequency distribution of time-averaged vertical velocity for the large (green), medium (red), and small (black) domain cases. The yellow box encloses the part of the distribution plotted in the panel on the right. Note that they y-axis is a logarithmic scale.

in the frequency of weak daily-average vertical velocities at the 500 hPa level in the range of  $0.02 < w < 0.05$  m/s during the evolution of the medium and large domain cases to steady-state (see Figure 5.6).

First, two reasons are proposed for the increase in frequency of weak convection with increasing domain size. We have seen that the mid-level stable layer became stronger with increasing domain size. This would tend to enhance mid-level detrainment, in effect preventing convection from reaching higher vertical velocities. Convective cores that would

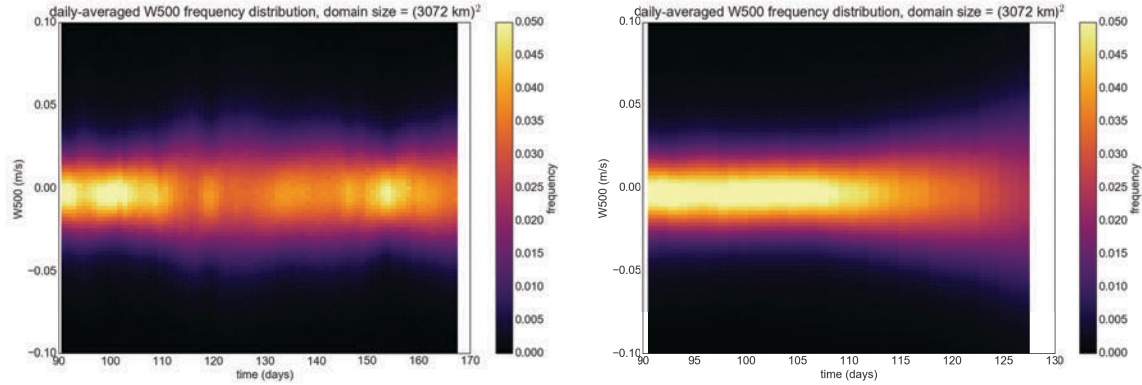


FIGURE 5.6. Frequency distribution of daily-average vertical velocity at 500 hPa for the medium domain case (left) and large domain case (right).

have previously penetrated through the mid-level stable layer and grow to high vertical velocities in the upper troposphere without being significantly slowed down by the stable layer (in the small domain case), now either become blocked by the mid-level stable layer or effectively slowed down. This idea is supported by an increase in mid-level mass flux out of the convective region and an associated enhanced mid-level stable layer with increasing domain size (see Figures 5.8 and 5.7). This is also supported by a sudden decrease in  $\sigma$  above the mid-level stable layer (around 5 km).

Note that  $\sigma_m$  also increased below the mid-level stable layer, which suggests that the mid-level stable layer is not the only reason for the increase in frequency of weak convection that occurred with domain size. Recall that we have seen that the spatial variance of buoyancy in the convective region boundary layer increased with domain size (see Figure 4.12 and 4.15). We hypothesize that this would tend to produce convection with more variable strength. This is consistent with the variance of the vertical velocity distribution increasing by 15% and 30% for the medium and large domain cases, respectively (see Table 6.2). Thus, while we would expect that higher buoyancy in the convective region boundary layer would result in stronger convection, it is apparent that the increase in vertical velocity variance occurred

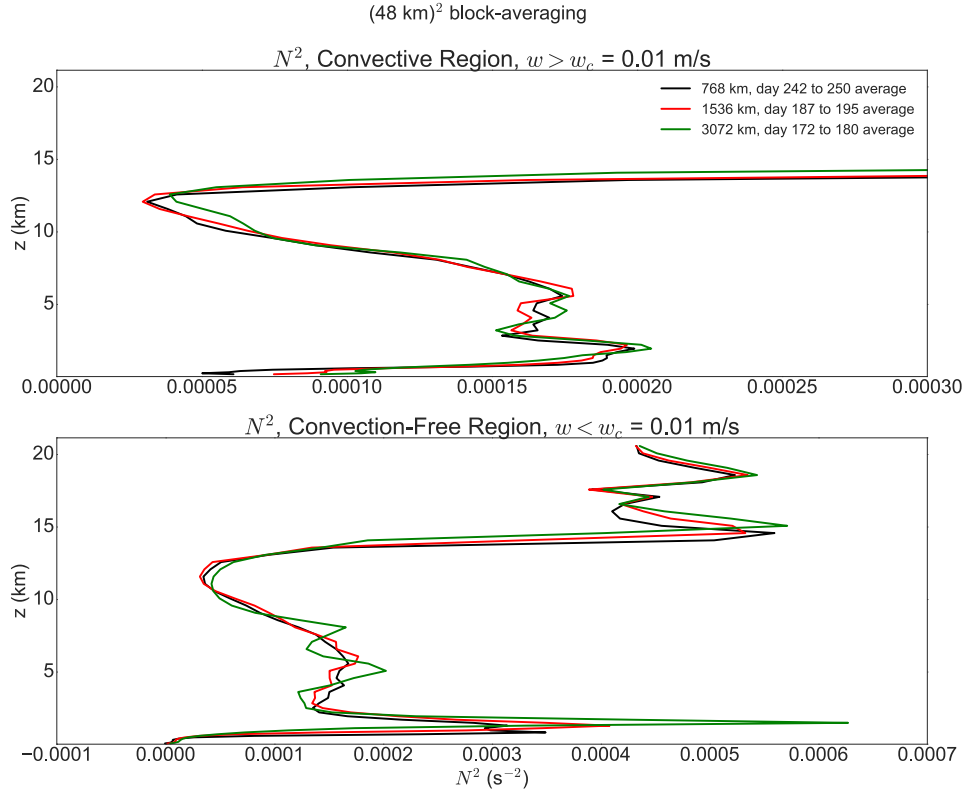


FIGURE 5.7. Top: Vertical profile of the buoyancy frequency,  $N^2$  (s<sup>-2</sup>), composited on the mesoscale convective region (with block-averaging), for the large (green), medium (red) and small (black) domain case. Bottom: same as top, except for the convection-free region.

in the range of weak convection ( $0 < w < 0.3$  m/s). Indeed, while the maximum vertical velocity became higher with larger domain size (see Table 6.2 and Figure 5.5, left panel), it is also clear that the frequency of stronger convection ( $0.3 < w < 1.5$  m/s) decreased with increasing domain size (see Figure 5.5, left panel).

A reason for the increase in downdraft strength is now proposed. This also relates to the observed enhancement of the mid-level stable layer. First, observe that the deep convective outflow height increased with increasing domain size (see Figure 5.8). This suggests that the deep convection penetrates deeper into the troposphere with increasing domain size. This is supported by a time series of maximum cloud top height (see Figure 5.9). With deeper

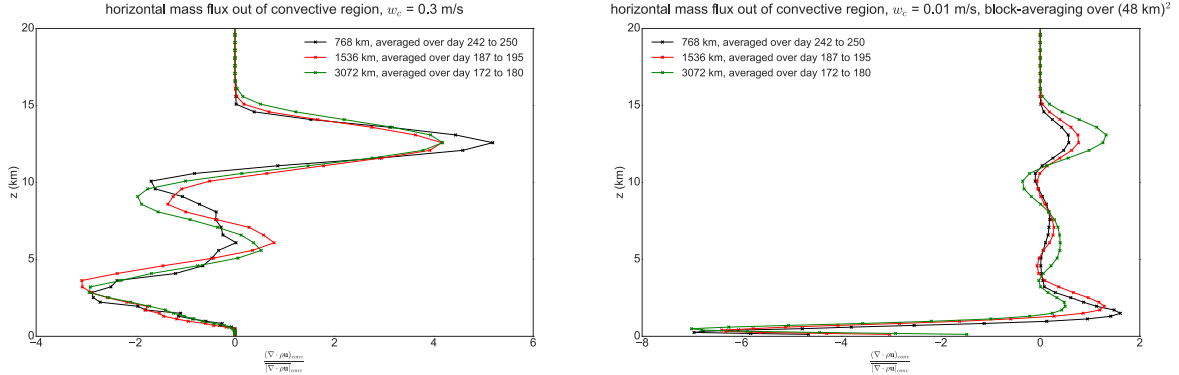


FIGURE 5.8. Left: Vertical profiles of the horizontal mass flux out of the convective core region (without block-averaging) for the large (green), medium (red) and small (black) domain case. Right: same as left, except for the mesoscale convective region (with block-averaging). Note that the horizontal mass flux has been scaled by the vertically averaged magnitude of the horizontal mass flux, to facilitate comparison between the two cases.

convection, higher production of ice and liquid precipitating condensate is expected. This can be seen in a time series of the vertically integrated liquid and ice precipitating condensate (see Figure 5.10). We speculate that the increase in precipitating condensate in turn leads to an increase in evaporative cooling in the convective region, which results in enhanced cold pools and hence stronger downdrafts. Note that as  $\int q_{p,l} dz$  goes up, there is also a slight increase in surface precipitation (see Figure 5.11), so that we cannot say with confidence that the re-evaporation of liquid precipitation has increased with domain size. However, note that the increase in precipitating ice most likely leads to more melting at the freezing level because no ice condensate reaches the surface. Because increased melting at the freezing level is associated with enhanced cooling, this may explain the stronger downdrafts. In any case, the increased melting seems to explain the enhancement of the mid-level stable layer that has been previously discussed (especially in the large domain case; see Figure 5.7).

The deeper convection is unsurprising as we have already seen that the strongest cores became stronger with domain size. In this case, the strongest convective cores would tend to

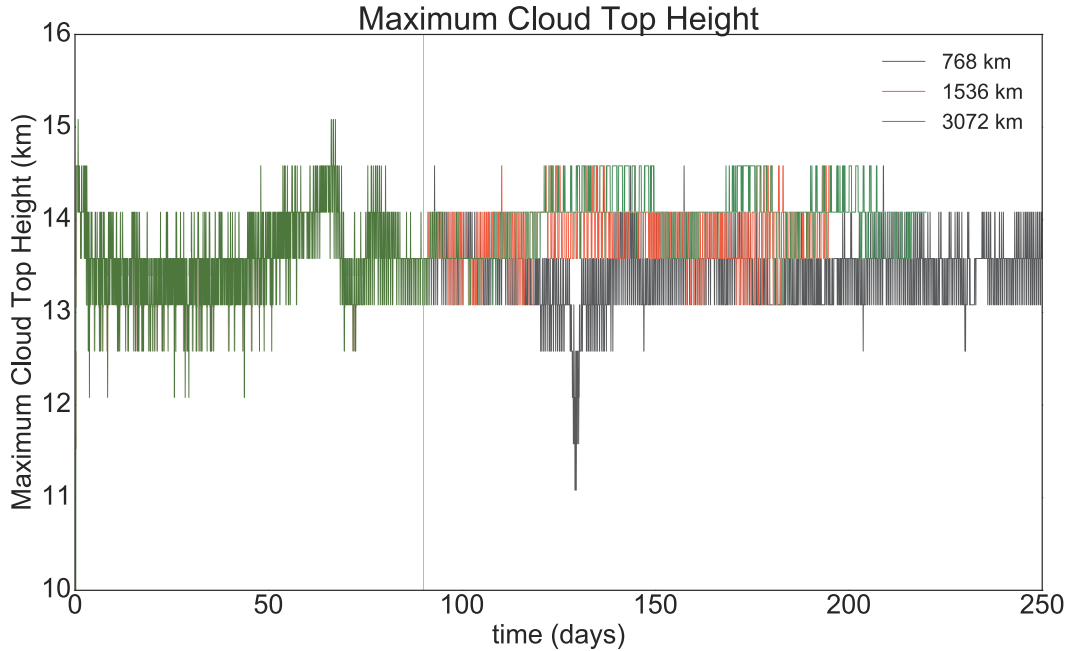


FIGURE 5.9. Hourly time series of maximum cloud top height (km), for the small (black), medium (red), and large (green) domain case. We define the maximum cloud top height as the height at which the sum of the non-precipitating condensate,  $q_n$ , above that height is greater than 0.001 g/kg.

“erode” the lower stratosphere over time, making the tropopause deeper over time. Another reason for the increase in the height of the deep convection is because the high cloud fraction became systematically higher with increasing domain size (see Figure 5.12). Since high clouds tend to shield the lower stratosphere from upwelling longwave radiation, we suspect that the increase in high cloud fraction has a cooling effect on the lower stratosphere. A cooling lower stratosphere means that the tropopause will increase in height. Indeed, we can see that the stratosphere is cooler with increasing domain size (see Figure 4.2). However, a times series of the radiative cooling profile does not seem to indicate significant cooling of the lower stratosphere preceding the increase in maximum cloud top height (see Figure 4.11, left panel), suggesting that the strongest convective cores are primarily responsible for the

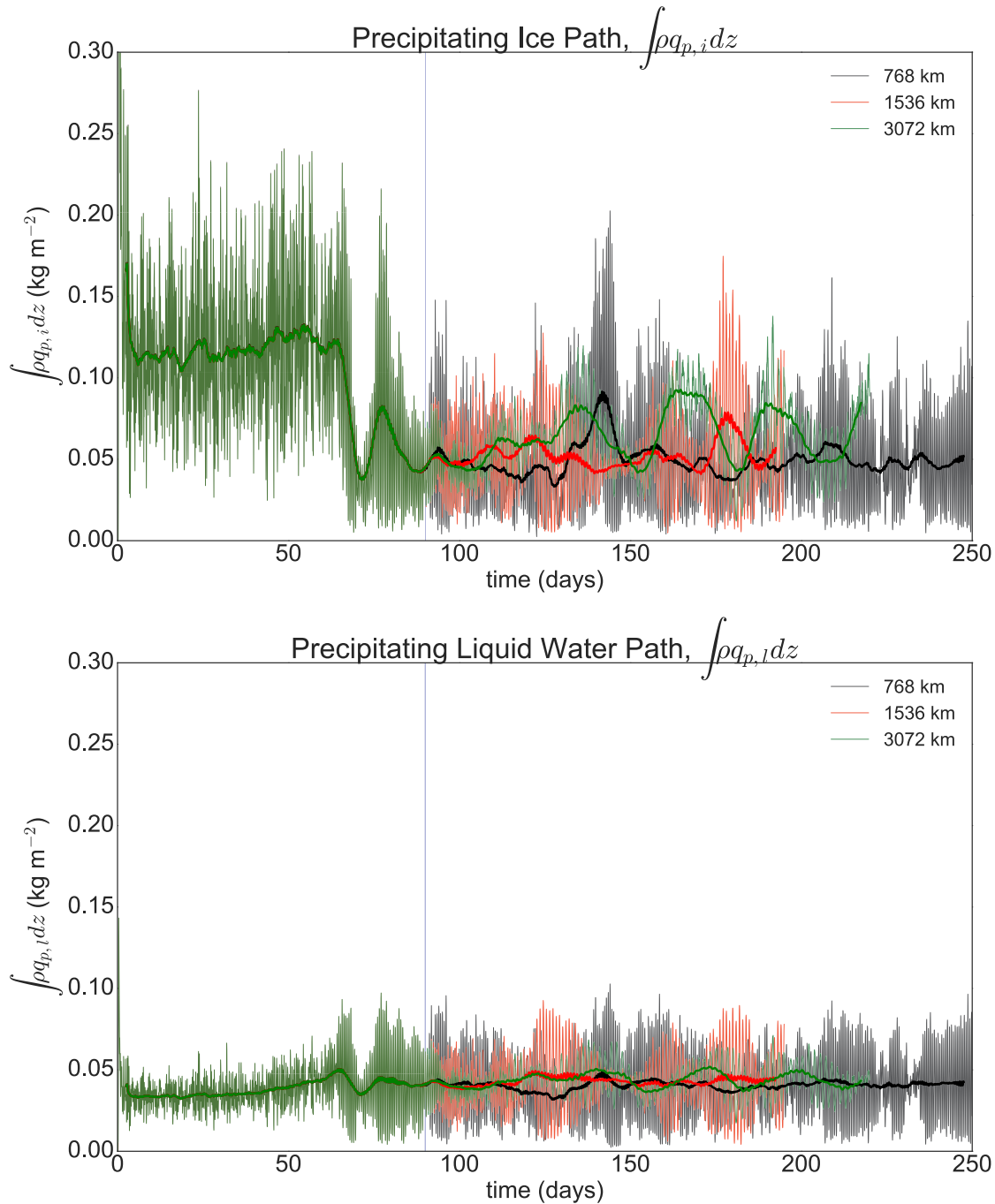


FIGURE 5.10. Top: Hourly time series of vertically-integrated precipitating ice condensate ( $\text{kg m}^{-2}$ ), for the small (black), medium (red), and large (green) domain case. Bottom: same as top except for precipitating liquid condensate.

raising of the tropopause, whereas the raising of the tropopause due to the increase in high cloud fraction is a secondary effect.

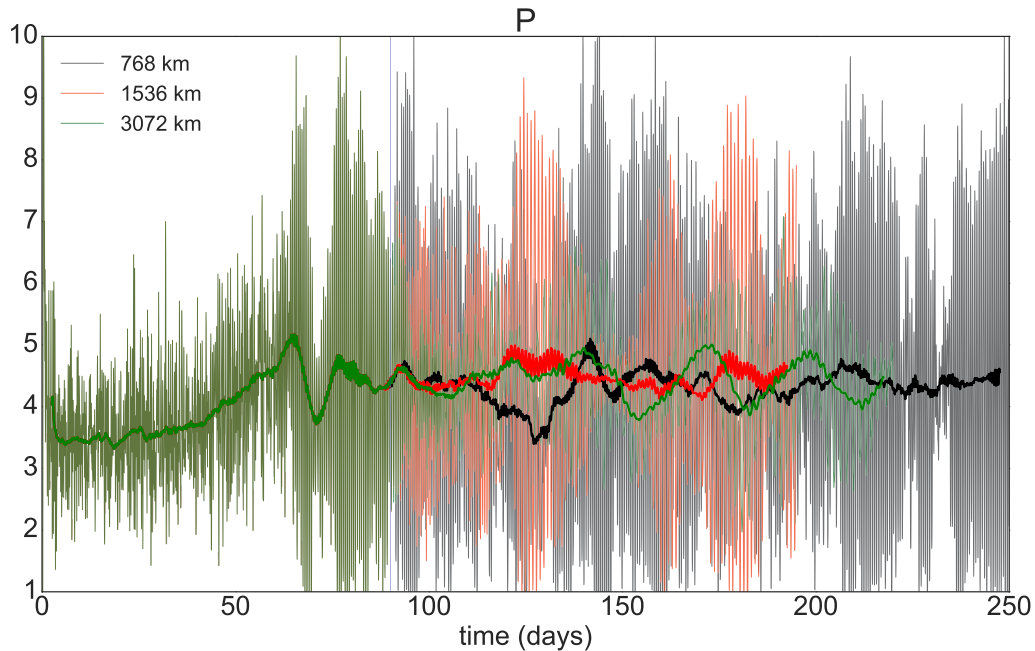


FIGURE 5.11. Hourly time series of the surface precipitation,  $P$  (mm/day), for the small (black), medium (red), and large (green) domain case.

Note that we hypothesize that there are more high clouds because the mass flux out of the mesoscale convective region increased with domain size (see Figure 5.8), as a result of a larger fraction of weak convective cores detraining at the upper troposphere. We suspect that there is a larger fraction of weak convective cores detraining at the upper troposphere because the higher spatial variance of buoyancy in the convective region boundary layer results in a larger fraction of intermediate strength convective cores that can penetrate the mid-level stable layer.

#### 5.4. CONVECTION-FREE REGION COMPOSITES

We have explained why the mesoscale convective updraft became weaker with domain size, however it is not clear why the convective region broadened with domain size. To explain this, we must consider the changes to the convection-free region that occur with domain size.

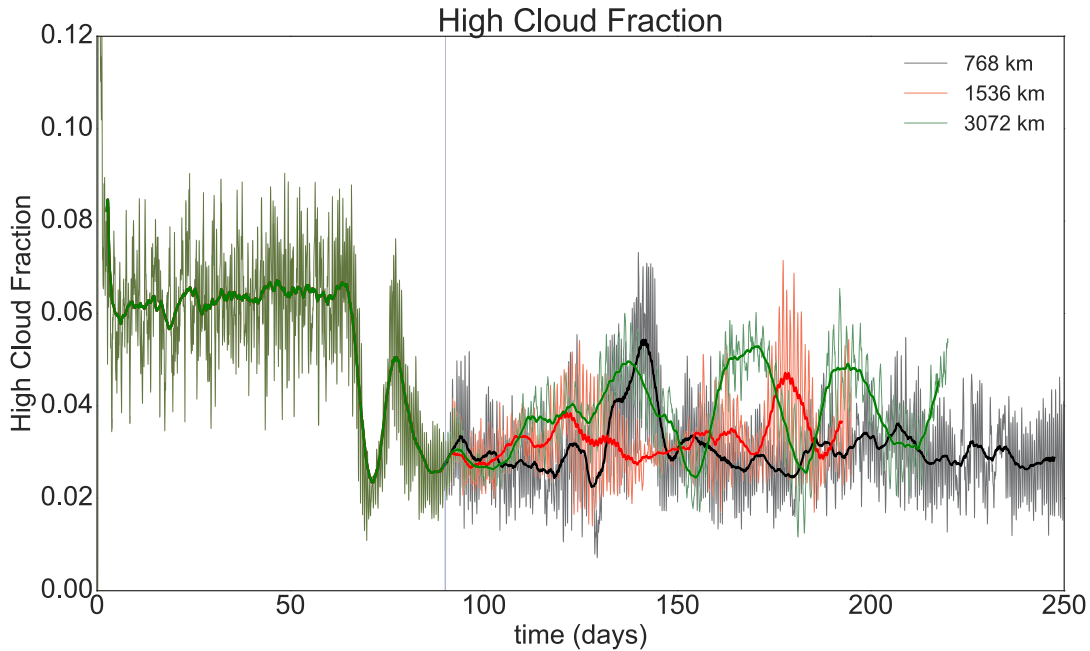


FIGURE 5.12. Hourly time series of high cloud fraction, for the small (black), medium (red), and large (green) domain case. The high cloud fraction is computed by

We must consider the convection-free region because, from a mass balance perspective, we know that the amount of mass moving upward in the convective region, must be balanced by the amount of mass moving downward in the convection-free region. Therefore any changes to the convective region, such as the strength and the size, must be consistent with this mass balance perspective. In the following, we show the convection-free mesoscale and core composites in order to explain some of the changes to the convective region that we have previously seen.

First, and most importantly, note that the mesoscale subsidence is similar throughout most of the troposphere in all of the domain cases ( $\sim -0.004$  m/s) (see Figure 5.13, right panel). The subsidence is relatively invariant in the dry region free troposphere due to close balance between radiative cooling and adiabatic warming driven by subsidence (see Figure 5.14, right panel). Evidently, the radiative cooling is relatively invariant in the

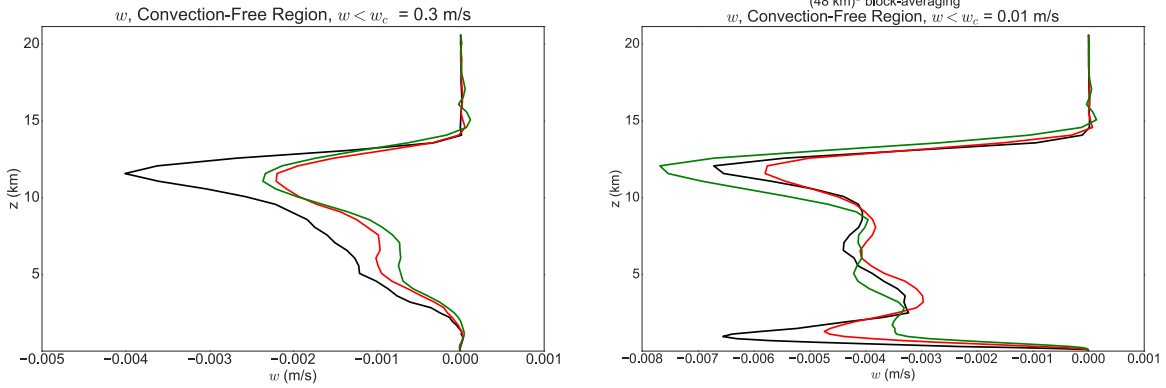


FIGURE 5.13. Left: Vertical profile of the vertical velocity composited on the convection-free region (without block-averaging), for the large (green), medium (red) and small (black) domain case. Right: same as left, except for the mesoscale convection-free region (with block-averaging).

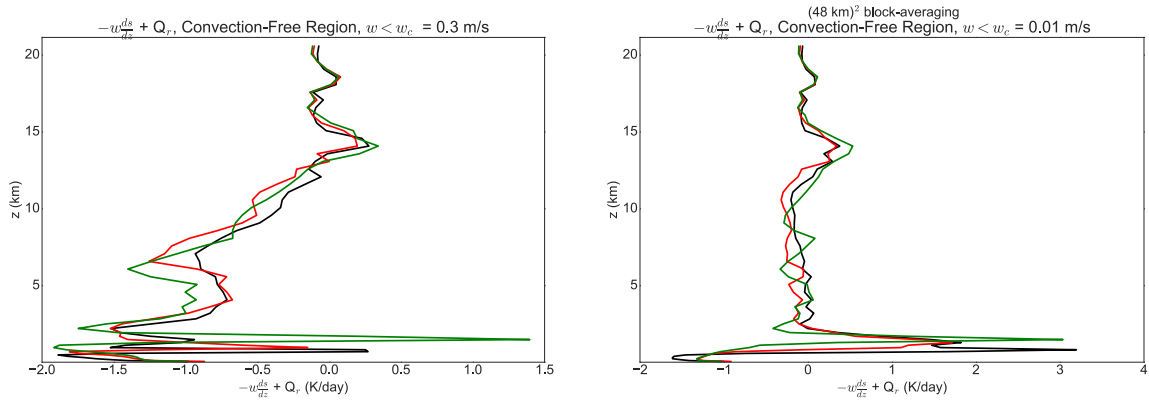


FIGURE 5.14. Left: Vertical profile of the sum of adiabatic warming and radiative cooling,  $-w \frac{ds}{dz} + Q_r$  (K/day), composited on the convection-free region (without block-averaging), for the large (green), medium (red) and small (black) domain case. Right: same as left, except for the mesoscale convection-free region (with block-averaging).

free troposphere with increasing domain size (see Figure 5.15, bottom panel), and so the subsidence is relatively invariant there.

On the other hand, the subsidence into the boundary layer systematically decreases with domain size (see Figure 5.13, right panel). Recall that there is a low-level circulation with return flow immediately above the convective region boundary layer (see Figure 4.8), which supplies the mass that subsides into the dry region boundary layer. Since the mass flux

out of the convective region is systematically weaker with increasing domain size (see Figure 5.8), it makes sense that the subsidence into the boundary layer is systematically weaker with increasing domain size. We suspect that the mass flux out of the convective region immediately above the boundary layer is weaker because the convective cores are more buoyant with domain size and detrain more at the mid-troposphere rather than immediately above the convective region boundary layer. Note that the weaker subsidence into the boundary layer explains the systematic deepening and moistening of the boundary layer with increasing domain size (shown previously in Figure 3.4). The deepening of the boundary layer and moistening can also be seen in composites of relative humidity in the dry region (see Figure 5.16, bottom panel).

It is interesting that despite the systematically weaker vertical mass convergence into the convection-free region boundary layer (due to the weaker subsidence), the mass flux into the convective region boundary layer is not necessarily systematically weaker (see Figure 5.8). We suspect that this is because the larger domains have more area for the subsidence to converge over.

It is also interesting that the subsidence in the convective-core free region is weaker with domain size, shown in Figure 5.13, left panel. It is important to remember that this composite includes samples of weak convection in the vicinity of the stronger convection, so the balance between adiabatic warming and radiative cooling is not necessarily expected to hold in this region (indeed, it does not; see Figure 5.14, left panel). First, note that the decrease in subsidence occurred mostly above  $z = 5$  km, around the mid-level stable layer. Also, recall that, with increasing domain size, while the strongest convective cores became stronger, there was a decrease in the frequency of strong convection and an increase in the

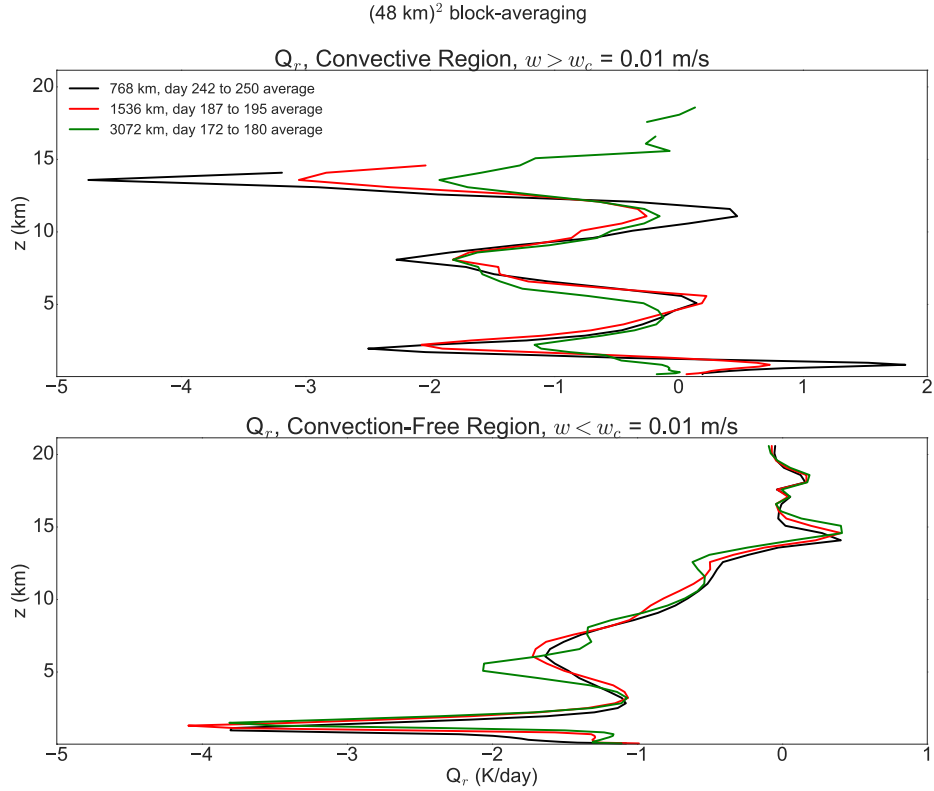


FIGURE 5.15. Top: Vertical profile of the radiative heating rate  $Q_r$  (K/day), composited on the mesoscale convective region (with block-averaging), for the large (green), medium (red) and small (black) domain case. Bottom: same as top, except for the convection-free region.

frequency of weak to intermediate strength convection (see Figure 5.5). This means that the time-averaged convective cores will be weaker with increasing domain size, which can be seen in Figure 5.4, left panel. Note that the weakening of the time-averaged convective cores is mostly above  $z = 5$  km, which coincides with the weaker subsidence in the convection-free region in Figure 5.13, left panel. Together, these results suggest that the enhanced mid-level stable layer in the larger domain cases makes the convective cores weaker in the time-averaged sense, thereby making the compensating subsidence in the convective-core free region weaker above  $z = 5$  km, by mass conservation.

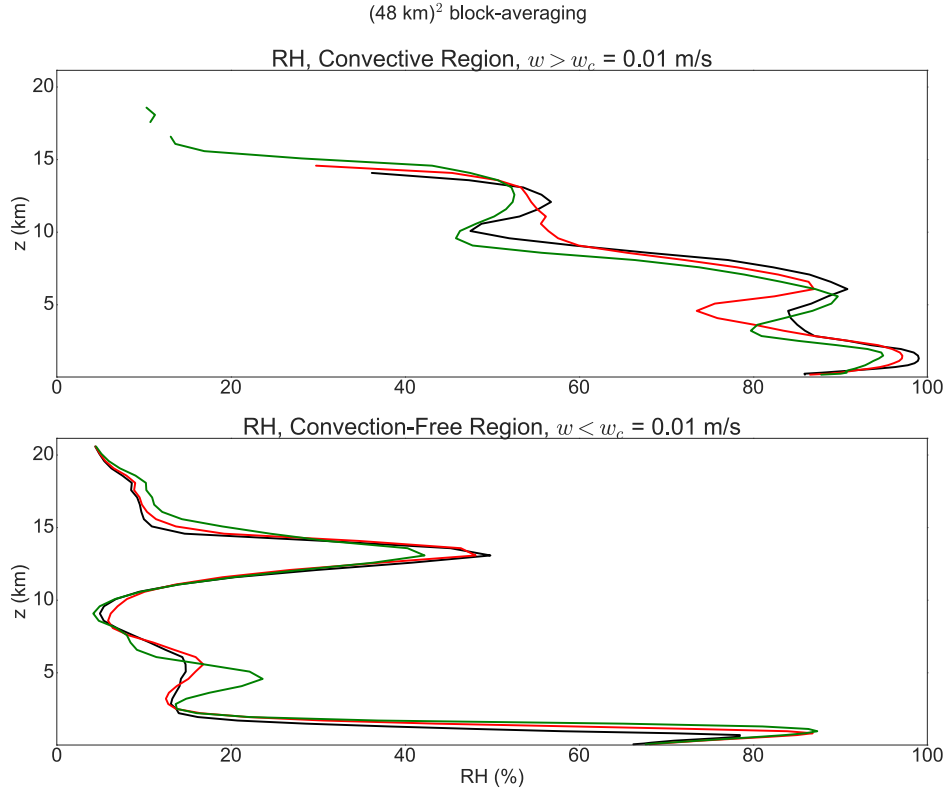


FIGURE 5.16. Top: Vertical profile of the radiative heating rate  $RH$  (%), composited on the mesoscale convective region (with block-averaging), for the large (green), medium (red) and small (black) domain case. Bottom: same as top, except for the convection-free region.

In summary, it is clear that the mesoscale convective region occupies a greater fraction of the domain with increasing domain size. Additionally, it makes sense that the mesoscale convective region updraft became weaker with domain size because the mesoscale subsidence is invariant with domain size. Furthermore, we have seen that the strongest cores are stronger with domain size, and that this is associated with deeper convection. The deeper convection seems to be associated with an enhanced mid-level stable layer, which we suspect has important effects on the distribution of convection and hence the cloud population. Indeed, we have seen that the enhanced mid-level stable layer is associated with an increase in horizontal mass flux out of the convective region in the mid-levels, which suggests an increase

in mid-level cloud detrainment. The main results will be summarized in table format for clarity and reference purposes in the next section. Later, we describe a physical mechanism for the broadening of the convective region with domain size, and then explore the effects of the broadening convective region on energy, mass, and water budgets in the framework of a simple model of the aggregated RCE state. In particular, we explore potential upper limits to the spatial scale of the convective region, which suggest a natural spatial scale of convective aggregation.

## 6. SUMMARY OF DOMAIN SIZE DEPENDENCIES

### 6.1. SIZE OF CONVECTIVE REGION

The previous results for the size of the convective region are summarized in Table 6.1 using three different metrics. We define the size of the convective region to be the fraction of the domain occupied by the convective region using three different metrics:  $\sigma_{PW}$ ,  $\sigma_{W500}$ , and  $\bar{P}/\hat{P}$ . The use of multiple metrics is useful because it gives a more complete picture of the structure of the convection. Note that in all cases, before calculating the size metric, the fields are time-averaged over the days 240 to 250, days 175 to 185 and days 170 to 180 in the small, medium, and large domain case, respectively. We define  $\sigma_{PW}$  as the fraction of points that exceed the mean PW by one standard deviation.  $\bar{P}/\hat{P}$  is the ratio of the domain-mean P with the average of P over points that have  $P > 0$ . Thus, it is a measure of the skewness of the precipitation distribution. If  $\bar{P}/\hat{P}$  is small, the precipitation is localized in the domain, whereas if  $\bar{P}/\hat{P}$  is large, the precipitation is spread out over the domain.  $\bar{P}/\hat{P}$  can also be interpreted as the degree of convective aggregation in the domain, as we would expect a more aggregated state to have more localized precipitation, and a less aggregated state to have less localized precipitation. We define  $\sigma_{W500}$ , as the fraction of vertical velocity blocks at 500 hPa that exceed  $w_c = 0.01$  m/s. Referring to Table 1, we see that the small domain and medium domain cases have similar spatial scale according to both  $\sigma_{PW}$  and  $\sigma_{W500}$  metrics, however the  $\bar{P}/\hat{P}$  metric indicates that the convection is more spread out in the medium domain case. In the large domain case, all metrics indicate that the convective region has broadened.

TABLE 6.1. Convective Region Size

| Domain Width | $\sigma_{PW}$ | $\sigma_{W500}$ | $\overline{P}/\hat{P}$ | $\overline{PW}$ |
|--------------|---------------|-----------------|------------------------|-----------------|
| 768 km       | 0.16          | 0.06            | 0.38                   | 28.0            |
| 1536 km      | 0.15          | 0.06            | 0.63                   | 31.9            |
| 3072 km      | 0.18          | 0.08            | 0.84                   | 35.9            |

TABLE 6.2. Convective Region and Dry Region Vertical Velocity, Stability, & Buoyancy Statistics

| Domain Width | $\overline{\Delta z \rho \frac{\partial w}{\partial t}}_{m,BL}$<br>(Pa) | $\overline{T - \overline{T}}_{m,BL}$<br>(K) | $w_{max}$<br>(m/s) | $\overline{ZC}_{max}^t$<br>(km) | $\overline{N^2}_{m,mid}$<br>( $10^{-4} \text{s}^{-2}$ ) | $\overline{N^2}_{dry,mid}$<br>( $10^{-4} \text{s}^{-2}$ ) | $\overline{N^2}_m$<br>( $10^{-4} \text{s}^{-2}$ ) |
|--------------|---|---|--------------------|---------------------------------|---|---|---|
| 768 km       | 2.8   | 0.26  | 25.5               | 13.5                            | 1.69  | 1.62  | 1.37  |
| 1536 km      | 3.6   | 0.46  | 28.1               | 13.8                            | 1.70  | 1.64  | 1.47  |
| 3072 km      | 4.1   | 0.53  | 33.2               | 14.0                            | 1.72  | 1.74  | 1.79  |

| Domain Width | $\text{var}(\Delta z \rho \frac{\partial w}{\partial t})_{m,BL}$<br>( $\text{Pa}^2$ ) | $\text{var}(w)$<br>( $\text{m}^2/\text{s}^2$ ) | $\overline{w}_m$ (m/s) | $\overline{w}_{dry}$ (m/s) | $\frac{\overline{(\nabla \cdot \rho \mathbf{u})}_{m,mid}}{ \overline{\nabla \cdot \rho \mathbf{u}} _m}$ | $\overline{w}_{dry,BL}$<br>( $10^{-3} \text{m/s}$ ) |
|--------------|---|--|------------------------|----------------------------|---|---|
| 768 km       | 1.0   | 0.026  | 0.069                  | -0.0030                    | 0.09  | -2.00   |
| 1536 km      | 2.1   | 0.035  | 0.054                  | -0.0025                    | 0.12  | -0.95   |
| 3072 km      | 4.1   | 0.038  | 0.038                  | -0.0026                    | 0.48  | -0.50   |

## 6.2. CONVECTIVE REGION AND DRY REGION STATISTICS

Domain size dependencies of the buoyancy, stability and vertical velocity in the convective region and dry region are summarized in Table 6.2. Note that the  $\overline{x}$  denotes a spatial average of the variable  $x$  over the region indicated by the subscript, and  $\overline{x}^t$  is a temporal average over the last 30 days of the simulation. For example,  $\overline{N^2}_m$  is the spatial average of the buoyancy frequency over the entire mesoscale convective region. Note that the subscript *mid* denotes the mid-levels between 5 km and 6 km, and *BL* denotes the boundary layer levels between the surface to  $p = 950$  hPa ( $\sim 600$  m).  $ZC_{max}$  is the maximum cloud top height, as defined in Figure 5.9.  $\overline{T - \overline{T}}_{m,BL}$  is the mean horizontal temperature anomaly in

the mesoscale convective region boundary layer. Finally, recall that the mesoscale convective region is defined in terms of time-averaged fields (8-day averaged vertical velocity), so that  $\text{var}(\Delta z \rho \frac{\partial w}{\partial t})_{m,BL}$  is the spatial variance, while  $\text{var}(w)$  is the variance in time and space.

## 7. DISCUSSION & INTERPRETATIONS

### 7.1. DISCUSSION OF THE SIMULATION RESULTS

Before discussing the results it is important to note that the larger domain cases may not have reached a complete equilibrium state yet (in particular, the 3072 x 3072 km case). It is possible that some of the large amplitude fluctuations in the large domain aggregated state (see Figure 3.1) would gradually level off over a long period of time. On the other hand, it is also possible that the aggregated state is only quasi-steady at larger scales (i.e. the large amplitude fluctuations will always remain). The fact that  $\sim 5$  mm amplitude fluctuations and  $\sim 20$  day time period between fluctuations are both relatively constant with time suggests that the aggregated state is oscillatory at large scales. We hope to extend the larger domain simulations in future work to address these concerns. Nonetheless, we believe that the conclusions formed here are largely insensitive to longer run-time of the simulations.

The reasons for the increase in the time-averaged domain mean precipitable water with increasing domain size are now summarized. The increase in the domain mean PW is a particularly important result because it is correlated with the size of the convective region and is associated with favorable remote conditions for convection. Recall that the subsidence into the dry region boundary layer weakened with increasing domain size as a result of a decrease in low-level mass flux out of the convective region. This is because convective cores became more buoyant with increasing domain size, and hence detrained more at mid-levels rather than immediately above the boundary layer, which in turn decreased the supply of mass available for subsidence into the dry region boundary layer. The weakening subsidence into the boundary layer was also associated with a deepening and moistening of the boundary

layer (see Figure 3.4), which in turn led to increased column integrated water vapor in the subsiding region (see Figure 4.6). It is also possible that the increase in mid-level clouds that occurred with increasing domain size further contributed to column moistening through changes in precipitation efficiency (Sherwood et al., 2014) and radiative heating profiles (Chikira, 2014). Consistent with this idea, we found that in the large domain case there was a mid-level peak in cloud fraction that coincided with both a mid-level peak in relative humidity and a mid-level peak in horizontal mass flux from the convective region into the dry region. (see Figures 4.4 and 5.8). This suggests the mid-level horizontal transport of water into the dry region was enhanced with increasing domain size, and that it is perhaps due to a greater number of clouds detraining at the mid-levels. We leave an a more detailed investigation of the relationship between the cloud changes and the associated moistening of the troposphere that occurred with domain size to future work.

The decrease in subsidence into the dry region boundary layer is a particularly important result because the deepening and growth of the boundary layer is a favorable condition for convection. Indeed, in the large domain case, an additional convective cluster formed far from the convective region when the simulation was run for an additional period of time (see Figure 3.6). This result suggests that the domain size is approaching a scale at which multiple convective clusters can co-exist in the domain; the natural spatial scale of convective aggregation. We conclude that this is ultimately because the subsidence into the boundary layer is decreasing as an indirect result of more buoyant convective cores in the convective region boundary layer detraining more at mid-levels rather than at low-levels.

Recall that an important result was that the increase in time-averaged domain mean precipitable was also associated with a broadening of the time-averaged mesoscale convective region with increasing domain size. It is important to emphasize that when we say the convective region has “broadened”, we mean that the *fractional area* of the mesoscale convective region increased with domain size, not just the *absolute area* of the convective region. Two reasons for the broadening of the time-averaged mesoscale convective region with increasing domain size are now discussed. Recall that, with increasing domain size, the convective region boundary layer had both higher spatial variance of buoyancy and higher maximum buoyancy, which we suspect is because the gravity wave adjustment time scale increases with domain size. Additionally, the free tropospheric subsidence in the dry region was relatively invariant with domain size, because the radiative cooling in the dry region did not change drastically with domain size. We conclude that these two properties of the aggregated RCE state result in the broadening of the time-averaged mesoscale convective region with increasing domain size for the following two reasons:

- (1) The more buoyant convective region layer means the strongest convective cores are stronger. As a result, the deep convection reaches deeper into the troposphere. An additional reason for the deeper convection is because there is more detrainment by weaker convection at the upper troposphere (because of (2)), which results in an increase in high cloud fraction, effectively cooling the lower stratosphere and deepening the tropopause. In either case, the effect of the deeper convection is to weaken the mesoscale convective updraft, because deeper convection is associated with stronger downdrafts and an enhanced mid-level stable layer due to increased melting. Therefore, because the free-tropospheric subsidence in the dry region is

invariant with domain size, the mesoscale convective region spreads out in order to conserve mass.

- (2) The higher spatial variance of buoyancy in the convective region boundary layer results in convective cores that have a higher spatial variance of strength. The increase in variance is associated with an increase in the frequency weak to intermediate strength convective cores, but counter-intuitively, a decrease in the frequency of strong convective cores. The frequency of strong convection decreases because the mid-level stable layer is enhanced with increasing domain size (by (1)). Therefore, because the free-tropospheric subsidence in the dry region is invariant with domain size, the higher frequency of weak convection means that the the mesoscale convective updraft will be weaker, and so it must broaden in order to conserve mass.

An additional interesting result was that the convective region not only broadened in the time-averaged sense, but that there were fluctuations in the size of the convective region over a regular time period. These fluctuations also became more prominent with increasing domain size. Specifically, in the large domain case, the convective region spontaneously spread out and contracted over a time period of about 25-30 days starting at around day 150 (see Supplementary Materials 3 and 4; animations of the cloud top height, precipitation and precipitable water for the large domain case, respectively). Interestingly, the fluctuations in domain-mean PW were also associated with fluctuations in the size of the convective region. In particular, the domain mean PW increased as the convective region broadened, but then the domain mean PW decreased as the convective region contracted (see Figure 3.1). Thus, the domain mean PW is correlated with the fractional area of the mesoscale convective region in time, and in the time-averaged sense. We suspect that the broadening

and contracting of the convective region affects the domain mean PW because of changes in the precipitation efficiency. In other words, when the convection is more spread out, there is more re-evaporation of precipitation and so the domain mean PW increases.

The broadening of the time-averaged convective region along with the more pronounced spreading and contracting of the convective region with domain size suggests that the convective region “wants” to occupy a larger fraction of the domain with larger domain size, but that there are also additional negative feedbacks that prevent the convective region from expanding and occupying a very large fraction the domain. Evidently, there is a “tug-of-war” between the feedbacks that promote spreading of the convective region with the feedbacks that promote contraction of the convective region. It is also evident that these feedbacks become stronger with increasing domain size because the fluctuations in the size of the convective region become larger with increasing domain size. It is tempting to conclude that (1) and (2) are responsible for the broadening of the time-averaged mesoscale convective region, *and* the fluctuations in the size of the convective region. However, since our analysis was strictly performed on time-averaged fields ( $\sim 10$  day average), we do not form any conclusions about the mechanisms contributing to these fluctuations.

We have discussed a mechanism that explains the sensitivity of the size of the mesoscale convective region to the domain size, but we have not discussed the reasons why the mesoscale convective region occupies the observed fraction of the domain, and why, for example, it does not occupy a much greater fraction of the domain. Furthermore, although our results suggest that the domain size is approaching the natural spatial scale of the aggregated state, it is not clear that an upper bound to the size of the convective region even exists. It is important to remember that in the state of radiative-convective equilibrium, the domain-averaged energy,

mass, water and momentum budgets must be in balance. Specifically, the radiative cooling must be balanced by the condensation warming, the sum of the upward and downward mass flux at each height must equal zero, and the surface precipitation must equal the surface evaporation. Thus, these balances must always hold, regardless of the specific dynamical mechanisms driving the convective region broadening that occurs with increasing domain size (e.g. (1) and (2)).

In order to address the question of what determines the spatial scale of the aggregated RCE state, we now introduce a simple semi-analytical model of the aggregated RCE state which requires that energy, mass, and water budgets are balanced. The simple model consists of a convective region, surrounded by a dry, subsiding region in cylindrical geometry, divided into three layers: a boundary layer, free troposphere and outflow layer. We prescribe the distance from the center of the convective region to the outer edge of the dry region, while the size of the convective region is an unknown variable, so that we can investigate the dependency of the size of the convective region on domain size. The simple model is discussed in more detail in the following section.

## 7.2. SIMPLE MODEL OF THE AGGREGATED RCE STATE

7.2.1. *Description.* The simple model of the aggregated RCE state is based on previous two-column models of tropical circulations (e.g. Pierrehumbert, 1995; Nillson & Emanuel, 1998; Larson et al. 1999, Raymond & Zeng, 2000; Raymond, 2000) and the cylindrical model of cumulus convection by Asai (1968). Like the previous two-column models, this model consists of a wet, convective column adjacent to a dry, subsiding column, with a sea-surface at the bottom which provides a flux of water vapor into the columns. The columns are further

subdivided into three distinct layers: a boundary layer, free troposphere, and outflow layer, as depicted in Figure 7.1. This does not capture the periodicity of the simulated aggregated RCE state, but does capture the general structure and shape of the quasi-circular convective region surrounded by a dry, subsiding region. These two-column models have generally been used to explore various properties of the tropical atmosphere, such as the climate sensitivity, or in other words, how the SST changes in response to a radiative perturbation (e.g. Pierrehumbert, 1995; Larson et al., 1999). In our model, however, we simply prescribe a fixed sea-surface temperature along with radiative cooling. The fixed SST is consistent with our numerical simulations, so that the solutions can be compared more easily to the simulation results. The temperature profile is assumed to be horizontally uniform, which is consistent with observed weak temperature gradients in the Tropics. Another important distinction to make is that the size of the convective region was generally prescribed in previous two-column models, whereas we will treat this as an unknown variable in order to investigate the natural spatial scale of the aggregated RCE state.

A final key point is that this is a steady-state model, so that the final aggregated RCE state is diagnosed. As the equations are nonlinear, it is possible that multiple equilibria exist and that our solution represents only one such equilibrium state. Additionally, it is known that the state of RCE has multiple equilibria (as discussed in Section 1.3). Importantly, however, time-varying models of similar set-up and complexity (e.g. Nillson & Emanuel, 1998) showed that the RCE state can evolve to a *unique* solution in which there is deep convection in one column, subsidence in the other column, and a large-scale circulation connecting both. Thus, our simple model is at the very least set up in such a way as to capture the aggregated RCE state.

| outflow          | inflow         |
|------------------|----------------|
| Conv. free trop. | Dry free trop. |
| Conv. BL         | Dry BL         |

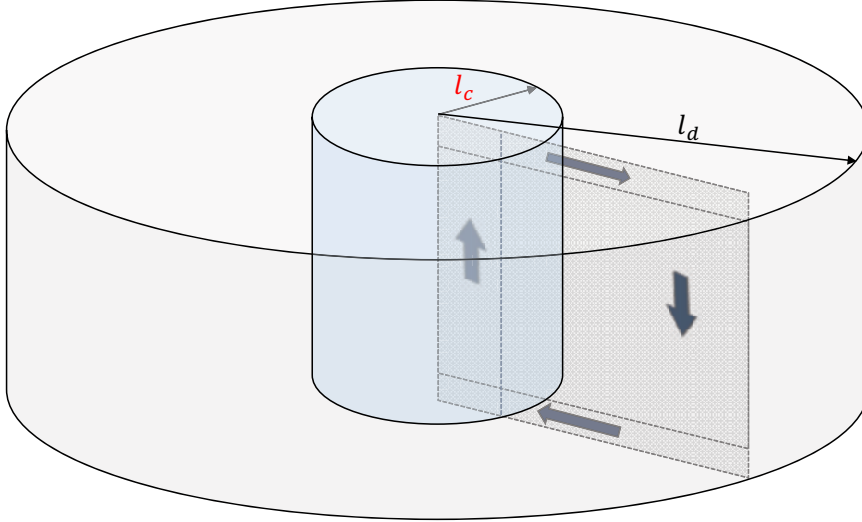


FIGURE 7.1. The geometric set-up of the simple model of the aggregated RCE state. The convective region is shaded in light blue, and the dry region is shaded in light grey. The dotted box represents a slice of the simple model, and the arrows denote the motion of the circulation. The top right panel indicates how each column is subdivided into separate regions: a boundary layer (BL), free troposphere, and outflow layer. Note that  $l_c$  is the length of the convective region and is unknown, and  $l_d$  is the distance from the center of the convective region to the edge of dry region and is prescribed.

A physical description of the model follows. The simple model is described by tracing a complete cycle of the circulation, starting from the dry region free troposphere. The convective region and dry region governing equations are derived in more detail in the next section.

The prescribed radiative cooling in the dry region free troposphere drives subsidence into the boundary layer (BL), which converges at the surface and produces surface winds by mass continuity. The surface winds produce evaporation of water vapor into the BL from the sea-surface, while the subsidence brings drier air into the BL from aloft. The surface winds increase moving toward the convective region due to the convergence of mass into

the boundary layer. Likewise, the relative humidity of the air increases because increased surface winds result in enhanced sea-surface evaporation. The convective region edge is reached at a distance where the BL obtains an unknown value of relative humidity,  $RH_c$ , which is a solution of the coupled mass, energy, and water budget equations. The convective region BL is assumed to have constant relative humidity equal to  $RH_c$ , where any water vapor that evaporates from the sea surface is injected directly into the convective region free troposphere. The surface winds converge in the convective region BL, resulting in upward motion in the convective region free troposphere. We require the adiabatic cooling produced by the upward motion to balance the sum of radiative cooling and condensation warming. The convective region free troposphere is assumed to be at 100% saturation with a horizontally uniform temperature profile given by a moist adiabat. All condensation is assumed to fall out as precipitation, with no re-evaporation occurring anywhere in the column, and a radiative cooling rate is prescribed throughout the convective region free troposphere. The convection is assumed to be deep, extending all the way to a prescribed tropopause height. The upward motion converges in the convective region outflow layer, producing winds that increase approaching the dry region inflow layer, and advection of water vapor into the dry region inflow layer. The winds then diverge in the dry region outflow layer, which results in subsidence and advection of the outflow water vapor into the dry region free troposphere. This completes a single cycle of the circulation.

*7.2.2. Equations.* We now derive the governing equations in each of the three vertical layers in both the convective region and the dry region. We also discuss the prescribed variables and simplifications used in each region. First, the variables of the model are introduced in Figure 7.2. Unknown variables are denoted by red text, whereas black text

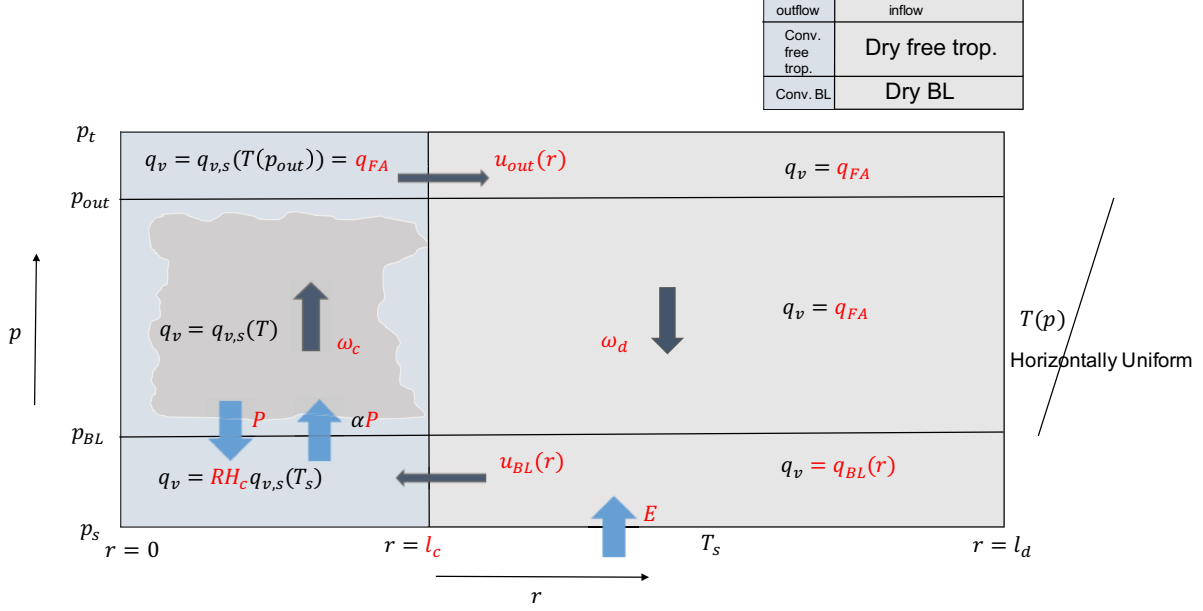


FIGURE 7.2. Variables of the simple model of the aggregated RCE state. The horizontal axis is radial distance from the convective region center (increasing to the right), and the vertical axis is pressure (increasing upward). Red text denotes unknown variables, and black text denotes prescribed variables. The solid blue arrows denote fluxes of water vapor or precipitation. The prescribed temperature profile is indicated on the far right and is horizontally uniform (note that this is merely for illustrative purposes; the exact temperature profile is shown in Figure 7.4). The prescribed net radiative heating in the dry region free troposphere,  $\hat{Q}_d$ , and the convective region free troposphere,  $\hat{Q}_c$ , are omitted for the sake of clarity. The dark grey arrows denote the motion of the circulation. The top right panel indicates how each column is subdivided into separate regions: a boundary layer (BL), free troposphere, and outflow layer.

indicates prescribed variables. In general, the subscript  $d$  denotes variables in the dry region free troposphere, while the subscript  $c$  denotes variables in the convective region. The subscript  $BL$  denotes variables in the boundary layer. Note that the prescribed net radiative heating in the dry region free troposphere,  $\hat{Q}_d$ , and the convective region free troposphere,  $\hat{Q}_c$ , are omitted from the diagram for the sake of clarity. Also note that the boundary conditions are not shown on the diagram. The radial velocity,  $u$ , is assumed to be zero at  $r = l_d$  and  $r = 0$ .

*Dry Region Free Troposphere.* The dry region free troposphere starts at a prescribed boundary layer top pressure of  $p_{BL} = 900$  hPa and extends to the prescribed outflow layer pressure given by  $p_{out} = 150$  hPa. The subsidence in the dry region,  $\omega_d$ , is assumed to be uniform (independent of  $p$  and  $r$ ) throughout the free troposphere, which is fairly consistent with the simulation results, except at the boundary layer top. Likewise, the water vapor mixing ratio,  $q_v = q_{FA}$  is assumed to be uniform, and will be given by the saturation water vapor mixing ratio at the height of the outflow. This results in a significantly drier free troposphere as compared to the simulations, but does not influence the radiative cooling because the radiative cooling is prescribed. The net radiative heating of the entire column,  $\hat{Q}_d$  (W/m<sup>2</sup>), is prescribed such that the troposphere cools at 1 K/day. This is consistent with the simulation results. The dry static energy profile,  $s(p)$ , is given by the prescribed moist adiabatic lapse rate and hydrostatic balance,  $\frac{\partial p}{\partial z} = -\rho g$ . The moist adiabatic lapse rate varies with height, but is approximately equal to 6.5 K/km.

The governing equations for the dry region free troposphere are now derived. In steady-state, the mass, water and energy budgets must be balanced, so we start with the continuity equation, which guarantees that mass is balanced:

$$\nabla \cdot \mathbf{u}_d + \frac{\partial \omega_d}{\partial p} = 0 \quad (14)$$

Here,  $u_d$  is the horizontal velocity in the dry region free troposphere and  $\omega_d$  is the vertical pressure velocity. We assume radial symmetry so that there is no azimuthal component of velocity and that the density  $\rho$  is horizontally uniform. This yields:

$$\nabla \cdot \mathbf{u}_d + \frac{\partial \omega}{\partial p} = \frac{1}{r} \frac{\partial (ru_d)}{\partial r} + \frac{\partial \omega_d}{\partial p} = 0 \quad (15)$$

The vertical velocity  $\omega_d$  is assumed to be uniform so that:

$$\frac{1}{r} \frac{\partial(ru_d)}{\partial r} = -\frac{\partial\omega_d}{\partial p} = 0 \quad (16)$$

$$\frac{1}{r} \frac{\partial(ru_d)}{\partial r} = 0 \quad (17)$$

$$ru_d(r) = A \quad (18)$$

Since the boundary condition is  $u_d(l_d) = 0$ , (18) becomes:

$$l_d u_d(l_d) = A = 0 \quad (19)$$

$$\implies u_d(r) = 0 \quad \text{for all } r \quad (20)$$

Therefore, there is no horizontal motion in the dry region free troposphere.

We now derive the equation for water balance in the dry region free troposphere. Recall that we assume that the water vapor mixing ratio is uniform and is given by the saturation water vapor mixing ratio at the outflow layer height, i.e.,  $q_v = q_{FA} = q_{v,s}(T(p_{out}))$ . Therefore, the water budget is trivial:

$$\nabla \cdot q_{FA} \mathbf{u}_d + \frac{\partial(\omega_d q_{FA})}{\partial p} = 0 \quad (21)$$

$$0 = 0$$

The equation for energy balance in the dry region free troposphere is now derived. Importantly, the moist static energy in the dry region free troposphere,  $h_d = s + L_v q_{FA}$ , is

conserved for adiabatic processes, so that:

$$\nabla \cdot \mathbf{u}_d h_d + \frac{\partial(\omega_d h_d)}{\partial p} = Q_d \quad (22)$$

$$\frac{\partial(\omega_d s)}{\partial p} = Q_d \quad (23)$$

Here,  $Q_d$  is the radiative heating rate in  $\text{J s}^{-1} \text{kg}^{-1}$ . Note that we have used the fact that  $u_d = 0$  and  $q_{FA}$  is uniform. Integrating both sides from  $p = p_{BL}$  to  $p = p_{out}$  and using the assumption that  $\omega_d$  is vertically uniform yields:

$$\omega_d(s(p_{BL}) - s(p_{out})) = \int_{p_{out}}^{p_{BL}} Q_d dp \quad (24)$$

$$\omega_d = \frac{\int_{p_{out}}^{p_{BL}} Q_d dp}{\Delta s_{trop}} \quad (25)$$

Here,  $\Delta s_{trop}$  is the dry static energy difference between the boundary layer top and the outflow layer,  $s(p_{BL}) - s(p_{out})$ . Defining the net radiative heating in the dry region free troposphere as  $\hat{Q}_d = \int_{z_{BL}}^{z_{out}} \rho Q_d dz$  and using hydrostatic balance and a change of variables on the RHS of (25) yields:

$$\omega_d = \frac{g \hat{Q}_d}{\Delta s_{trop}} \quad (26)$$

Importantly, (26) is a balance between adiabatic warming and net radiative cooling of the entire dry region free troposphere. This balance is consistent with our simulation results, and is expected to hold in clear-sky areas in observations of the atmosphere.

In summary, the mass, energy and water balances yield three equations for the dry region free troposphere, which hold for  $l_c < r < l_d$  and  $p_{out} < p < p_{BL}$  :

$$u_d(r) = 0 \tag{27}$$

$$q_v = q_{FA} = q_{v,s}(T(p_{out})) \tag{28}$$

$$\omega_d = \frac{g\hat{Q}_d}{\Delta s_{trop}} \tag{29}$$

*Dry Region Boundary Layer.* The dry region boundary layer starts at  $p = p_s = 1000$  hPa, and extends to  $p_{BL} = 900$  hPa. The boundary layer is assumed to be well-mixed ( $\frac{\partial s}{\partial p}$ ,  $\frac{\partial q_{BL}}{\partial p}$ , and  $\frac{\partial u_{BL}}{\partial p}$  are all approximately zero). We use a bulk-aerodynamic formula to calculate the turbulent flux of water vapor from the sea-surface into the boundary layer, with exchange coefficient,  $c_E = 0.001$ . The exchange coefficient is a parameterization of the efficiency of energy exchange between the surface and the overlying boundary layer, which is typically a function of surface properties, like the roughness. The value is chosen to be consistent with observed properties of a standard sea-surface. At the far edge of the dry region,  $l_d$ , the boundary layer water vapor mixing ratio is assumed to be equal to the free tropospheric water vapor mixing ratio,  $q_{FA}$ . This results in an unrealistically dry boundary layer far from the convective region. We assume that the radiative cooling in the boundary layer balances the warming due to subsidence and the surface sensible heat fluxes, so that the temperature of the boundary layer is not changing with time, however we do not explicitly prescribe a radiative cooling for the boundary layer. For consistency, we could prescribe the radiative cooling in the dry region boundary layer such that  $\omega$  is continuous across the boundary layer

top, however this is inconsistent with the simulation results because  $\omega$  changes quite rapidly across the boundary layer top (see Figure 4.16, bottom panel).

The governing equations for the dry region boundary layer are now derived. As was previously done for the dry region free troposphere, we start with the continuity equation:

$$\nabla \cdot \delta p_{BL} \mathbf{u}_{BL} = g E_d \quad (30)$$

Here,  $\delta p_{BL} = p_s - p_{BL}$  is the pressure thickness of the boundary layer.  $\delta z_{BL} = \frac{\delta p_{BL}}{\rho_{BL} g}$  is the corresponding boundary layer thickness in meters.  $E_d = \frac{\omega_d}{g}$  is the boundary layer entrainment rate ( $\text{kg m}^{-2} \text{s}^{-1}$ ). We assume that the entrainment rate is proportional to the subsidence into the boundary layer, so that the depth of the boundary layer is not changing with time. Therefore the previous expression simplifies to:

$$\nabla \cdot \delta p_{BL} \mathbf{u}_{BL} = \omega_d \quad (31)$$

Now, in radial coordinates and assuming radial symmetry (i.e. the azimuthal component of the divergence is zero), this becomes:

$$\frac{1}{r} \frac{\partial(r u_{BL})}{\partial r} = \frac{\omega_d}{\delta p_{BL}} \quad (32)$$

Integrating both sides from  $r' = r$  to  $r' = l_d$  yields:

$$u_{BL}(l_d) - u_{BL}(r) = \frac{\omega_d}{2\delta p_{BL}} \frac{(l_d^2 - r^2)}{r} \quad (33)$$

Finally, using the boundary condition that  $u_{BL}(l_d) = 0$  yields:

$$u_{BL}(r) = -\frac{\omega_d}{2\delta p_{BL}} \frac{(l_d^2 - r^2)}{r} \quad (34)$$

We now derive the equation for the water balance for the dry region boundary layer.

Starting with conservation of water vapor:

$$\nabla \cdot \delta p_{BL} \mathbf{u}_{BL} q_{BL} = g(F_q)_s + gE_d q_{FA} \quad (35)$$

Here,  $q_{BL}$  is the water vapor mixing ratio in the boundary layer, which varies radially. Likewise,  $u_{BL}$  is radial velocity in the boundary layer, which varies radially. The surface evaporation is given by  $(F_q)_s$  in  $\text{kg m}^{-2} \text{s}^{-1}$ . Therefore, the water vapor balance is between horizontal advection, entrainment of water vapor from the overlying dry free troposphere, and surface evaporation. As previously discussed, we use a bulk-aerodynamic formula for  $(F_q)_s$ , that is:

$$(F_q)_s = \rho c_E |u_{BL}| (q_{sat} - q_{BL}) \quad (36)$$

Expanding the LHS of (35) yields:

$$q_{BL}(\nabla \cdot \delta p_{BL} \mathbf{u}_{BL}) + \delta p_{BL} \mathbf{u}_{BL} \cdot \nabla q_{BL} = g(F_q)_s + gE_d q_{FA} \quad (37)$$

Using the definition of  $E_d$  and conservation of mass, (31), in the previous expression yields:

$$\omega_d q_{BL} + \delta p_{BL} \mathbf{u}_{BL} \cdot \nabla q_{BL} = g(F_q)_s + \omega_d q_{FA} \quad (38)$$

Using the bulk-aerodynamic formula for  $(F_q)_s$ , (36) and the fact that  $\nabla q_{BL} = \frac{\partial q_{BL}}{\partial r}$  yields:

$$u_{BL} \frac{\partial q_{BL}}{\partial r} + \frac{\omega_d}{\delta p_{BL}} q_{BL} = \frac{\rho g c_E}{\delta p_{BL}} |u_{BL}| (q_{sat} - q_{BL}) + \frac{\omega_d}{\delta p_{BL}} q_{FA} \quad (39)$$

Moving all  $q_{BL}$  terms to the LHS yields:

$$u_{BL} \frac{\partial q_{BL}}{\partial r} + \frac{\omega_d}{\delta p_{BL}} q_{BL} + \frac{\rho g c_E}{\delta p_{BL}} |u_{BL}| q_{BL} = \frac{\rho g c_E}{\delta p_{BL}} |u_{BL}| q_{sat} + \frac{\omega_d}{\delta p_{BL}} q_{FA} \quad (40)$$

Dividing by  $u_{BL}$  and substituting the expression for  $u_{BL}$ , (34) yields an ordinary differential equation for  $q_{BL}(r)$ :

$$\frac{\partial q_{BL}}{\partial r} - \left( \frac{c_E}{\delta z_{BL}} + \frac{2r}{l_d^2 - r^2} \right) q_{BL} = -\frac{c_E}{\delta z_{BL}} q_{sat} - \frac{2r}{l_d^2 - r^2} q_{FA} \quad (41)$$

Solving (41) for  $q_{BL}$  with the boundary condition that  $q_{BL}(l_d) = q_{FA}$  yields:

$$q_{BL}(r) = q_{sat} + \frac{2\hat{z}(q_{FA} - q_{sat})}{l_d^2 - r^2} \left[ r + \hat{z} - (\hat{z} + l_d) e^{\frac{r-l_d}{\hat{z}}} \right] \quad (42)$$

Here, we define  $\hat{z} = \frac{\delta z_{BL}}{c_E}$ .  $\hat{z}$  is the characteristic length scale for  $q_{BL}$  and is on the order of 1000 km for the prescribed values of  $c_E$  and  $\delta z_{BL}$ . This suggests that in order to obtain physically reasonable solutions,  $l_d$  should at least be greater than 1000 km. Note that  $q_{BL}$  is independent of  $\omega_d$  under this set-up. The subsidence drying is “felt” by the boundary layer purely via the value of  $q_{FA}$ . Realistically, the height of the boundary layer,  $p_{BL}$  is dependent on  $\omega_d$ , which would in turn influence  $q_{BL}$ .

Finally, note that, as previously discussed, the convective region edge is defined by the distance at which the relative humidity in the dry region boundary layer reaches  $RH_c$ , i.e,

we must have:

$$q_{BL}(l_c) = RH_c q_{v,s}(T_{BL}) = RH_c q_{sat} \quad (43)$$

Note that we have assumed the temperature of boundary layer is equal to the SST in (43), which is quite consistent with the simulations. Thus, (43) and (42) can be used to define the location of the convective region edge. This yields:

$$(RH_c - 1)q_{sat} = \frac{2\hat{z}(q_{FA} - q_{sat})}{l_d^2 - l_c^2} \left[ l_c + \hat{z} - (\hat{z} + l_d)e^{\frac{l_c - l_d}{\hat{z}}} \right] \quad (44)$$

In summary, there are two governing equations for the dry region boundary layer, which hold for  $l_c < r < l_d$  and  $p_{BL} < p < p_s$  :

$$u_{BL}(r) = -\frac{\omega_d}{2\delta p_{BL}} \frac{(l_d^2 - r^2)}{r} \quad (45)$$

$$RH_c = 1 + \frac{2\hat{z}(q_{FA} - q_{sat})}{q_{sat}(l_d^2 - l_c^2)} \left[ l_c + \hat{z} - (\hat{z} + l_d)e^{\frac{l_c - l_d}{\hat{z}}} \right] \quad (46)$$

*Convective Region Boundary Layer.* The convective region boundary layer extends from  $p_s$  to  $p_{BL}$ , as in the case of the dry region boundary layer. By comparison, however, the water vapor budget is much more simple. We assume that the relative humidity is radially constant throughout the boundary layer and equal to  $RH_c$ , where all of the water vapor that evaporates from the sea-surface is transported directly into the convective region free troposphere by turbulent fluxes. Strictly speaking, a constant relative humidity in the convective region boundary layer is not consistent with our simulations where relative humidity was found to vary radially in the convective region boundary layer. The turbulent fluxes of water vapor into the convective region free troposphere are assumed to be directly proportional

to the precipitation with constant of proportionality  $\alpha$ , which we diagnose from the simulation results. This dependence is motivated by the fact that more vigorous deep convection is typically associated with both more precipitation and surface evaporation due to enhanced cold pools and hence stronger downdrafts. The surface winds necessarily approach zero at the convective region center, which results in horizontal mass convergence, by continuity. Finally, since the convective region boundary layer essentially passively transports water vapor into the free troposphere, the net radiative heating in the convective region boundary layer is assumed to be zero so that the energy budget is balanced.

The mass balance in the convective region boundary layer is now derived. Starting with the continuity equation in the convective region boundary layer:

$$\nabla \cdot \delta p_{BL} \mathbf{u}_{BL} = \omega_c \quad (47)$$

Here,  $\omega_c$  is the vertical velocity in the convective region free troposphere, assumed to be uniform. The steps for deriving  $u_{BL}$  in the convective region boundary layer are same as the steps used to derive (34). This ultimately yields:

$$u_{BL}(r) = \frac{\omega_c}{2\delta p_{BL}} r \quad (48)$$

Importantly, mass conservation over the entire domain can be derived from (34) and (56).

Since  $u_{BL}$  must be continuous at  $r = l_c$ , we must have:

$$u_{BL}(l_c) = -\frac{\omega_d}{2\delta p_{BL}} \frac{l_d^2 - l_c^2}{l_c} = \frac{\omega_c}{2\delta p_{BL}} l_c$$

$$\omega_d(l_d^2 - l_c^2) = -\omega_c l_c^2 \quad (49)$$

Note that (49) guarantees the conservation of mass over the entire domain. In other words, at each height, the mass that moves upward in the convective region must be balanced by mass that moves downward in the dry region.

The water balance in the convective region boundary layer is now derived. As previously discussed, the relative humidity is assumed to be a uniform value of  $RH_c$ , so that  $q_{BL} = RH_c q_{sat}$ . Additionally, the evaporation of water from the sea-surface,  $(F_q)_s$ , is assumed to be equal to the turbulent flux of water vapor into the free troposphere,  $F_q(p_{BL})$ . This results in a trivial water balance for the convective region boundary layer:

$$\nabla \cdot (\delta p_{BL} \mathbf{u}_{BL} q_{BL}) = \omega_c q_{BL} + g[(F_q)_s - F_q(p_{BL})] \quad (50)$$

$$q_{BL}(\nabla \cdot \delta p_{BL} \mathbf{u}_{BL}) + \delta p_{BL} \mathbf{u}_{BL} \cdot \nabla q_{BL} = \omega_c q_{BL} \quad (51)$$

Here, we expanded the LHS (50) and have used the assumption that  $(F_q)_s = F_q(p_{BL})$ . Using the fact that  $\nabla q_{BL} = \frac{\partial q_{BL}}{\partial r} = 0$  and the continuity equation, (47), yields:

$$\omega_c q_{BL} = \omega_c q_{BL} \quad (52)$$

Therefore the water budget is balanced, assuming that the water vapor mixing ratio in the convective region boundary layer is uniform and equal to  $RH_c q_{sat}$ .

The energy balance in the convective region boundary layer is now derived. Starting with conservation of moist static energy in the convective region boundary layer,  $h_{BL,c} = s + L_v RH_c q_{sat}$ , yields:

$$\nabla \cdot (\delta p_{BL} \mathbf{u}_{BL} h_{BL,c}) = \omega_c h_{BL,c} + g L_v [(F_q)_s - F_q(p_{BL})] + g Q_{c,BL} \quad (53)$$

Here  $Q_{c,BL}$  is the net radiative heating rate in the convective region boundary layer. Noting that  $h_{BL,c}$  is uniform and using  $(F_q)_s = F_q(p_{BL})$  yields:

$$h_{BL,c} \nabla \cdot \delta p_{BL} \mathbf{u}_{BL} = \omega_c h_{BL,c} + g Q_{c,BL} \quad (54)$$

Using the continuity equation, (47), yields:

$$h_{BL,c} \omega_c = \omega_c h_{BL,c} + g Q_{c,BL} \quad (55)$$

Therefore, the net radiative heating in the convective region boundary layer must be zero, as previously discussed.

This yields three equations for the convective region boundary layer, valid for  $0 < r < l_c$  and  $p_{BL} < p < p_s$  :

$$u_{BL}(r) = \frac{\omega_c}{2\delta p_{BL}} r \quad (56)$$

$$q_{BL} = RH_c q_{sat} \quad (57)$$

$$Q_{c,BL} = 0 \quad (58)$$

*Convective Region Free Troposphere.* The convective region free troposphere extends from  $p_{BL}$  to  $p_{out}$ , as in the case of the dry region free troposphere. The rising motion in the convective region free troposphere,  $\omega_c$ , is driven by the mass convergence in the convective region boundary layer, and is assumed to be vertically uniform. The free troposphere is assumed to be at 100% saturation, where all condensation falls out as precipitation with no re-evaporation. The assumption of 100% relative humidity in the convective region is not necessarily valid (see Figure 4.5), although the relative humidity is high ( $\sim 70$  to  $80$  %).

It is important to note that  $\omega_c$  is the large-scale ascent in the convective region, and not equivalent to the vertical velocity of the convective cores. As such, we expect that  $\omega_c$  will be most comparable to the block-averaged mesoscale vertical velocity,  $w_m$ , from the simulation results. The assumption of constant vertical velocity in the convective region is an additional deficiency of the simple model, as we have previously seen that the mesoscale updraft in the convective region is not vertically uniform. We finally require that the adiabatic cooling driven by the rising motion must balance the sum of condensation warming and net radiative heating,  $\hat{Q}_c$ . Note that in doing this, the convective heat and moisture fluxes are neglected. This is clearly a highly simplistic model of the convective region – both re-evaporation of precipitation and convective fluxes are clearly important. However, we only intend to capture the general features of the convective region while keeping the model as simple as possible. Additional complexity can be introduced in future work.

As  $\omega_c$  is assumed to be uniform, the radial velocity in the convective region free troposphere,  $u_c$ , is zero. Therefore there is no horizontal motion in the convective region free troposphere, much like the dry region free troposphere. We skip the derivation for  $u_c$  because the derivation is identical to that used to show that  $u_d$  is zero.

The water balance for the convective region free troposphere is now derived. First, we start with conservation of liquid water,  $q_l$ :

$$\frac{\partial(q_l)}{\partial t} + \nabla \cdot q_l \mathbf{u}_c + \frac{\partial(\omega_c q_l)}{\partial p} = c - g \frac{\partial F_p}{\partial p} \quad (59)$$

Here,  $c$  is the rate of condensation ( $s^{-1}$ ) and  $F_p$  is the precipitation flux (positive downward) in  $kg\ m^{-2}\ s^{-1}$ . Assuming that  $q_l$  is uniform and in steady-state means the previous expression

becomes:

$$0 = c - g \frac{\partial F_p}{\partial p} \quad (60)$$

$$c = g \frac{\partial F_p}{\partial p} \quad (61)$$

(61) simply states that condensed water is immediately converted to precipitation.

The water vapor balance in the convective region free troposphere is now derived. Recall that we assume that the water vapor mixing ratio is given by the saturation water vapor mixing ratio, i.e.,  $q_v = q_{v,s}(T(p))$  in the convective region free troposphere. This yields:

$$\nabla \cdot q_{v,s} \mathbf{u}_c + \frac{\partial(\omega_c q_{v,s})}{\partial p} = -c + g \frac{\partial F_q}{\partial p} \quad (62)$$

$$\omega_c \frac{\partial q_{v,s}}{\partial p} = -c + g \frac{\partial F_q}{\partial p} \quad (63)$$

Here, we have used the fact that  $u_c = 0$  and that  $\omega_c$  is uniform.  $F_q$  is the turbulent water vapor flux (positive upward), which is zero everywhere except at  $p = p_{BL}$ . Recall that we assume that there is surface evaporation in the convective region boundary layer, which is associated with a turbulent flux of water vapor directly into the convective region free troposphere. Recall that we also assume that this turbulent flux of water vapor is proportional to  $P$  with constant of proportionality  $\alpha$ . Dividing (63) by  $\rho$  and using (61) in (63) yields:

$$\omega_c \frac{\partial q_{v,s}}{\partial p} = -g \frac{\partial F_p}{\partial p} + g \frac{\partial F_q}{\partial p} \quad (64)$$

Integrating the previous expression from  $p = p_{BL}$  to  $p = p_{out}$ :

$$\omega_c[q_{v,s}(p_{BL}) - q_{FA}] = -g[F_p(p_{BL}) - F_p(p_t)] + gF_q(p_{BL}) \quad (65)$$

We define the surface precipitation,  $P$ , as  $P = F_p(p_{BL})$ , so that  $P$  has units  $\text{kg m}^{-2} \text{s}^{-1}$ , and assume that  $F_p(p_t) = 0$  so that:

$$P = F_p(p_{BL}) = -\frac{\omega_c}{g}[q_{v,s}(p_{BL}) - q_{FA}] + F_q(p_{BL}) \quad (66)$$

Using the assumption that  $F_q(p_{BL})$  is proportional to  $P$ , with constant of proportionality  $\alpha$ , we can then write:

$$P = -\frac{\omega_c}{g}[q_{v,s}(p_{BL}) - q_{FA}] + \alpha P \quad (67)$$

$$(1 - \alpha)P = -\frac{\omega_c}{g}[q_{v,s}(p_{BL}) - q_{FA}] \quad (68)$$

$$P = -\frac{\frac{\omega_c}{g}[q_{v,s}(p_{BL}) - q_{FA}]}{1 - \alpha} \quad (69)$$

Finally, we assume that the water vapor at the boundary layer top,  $q_{v,s}(p_{BL})$ , is equal to the water vapor in the boundary layer,  $RH_c q_{sat}$ . This is equivalent to assuming that the lifting condensation level is at  $p_{BL}$ , which is fairly consistent with the simulation results.

This yields:

$$P = -\frac{\frac{\omega_c}{g}(RH_c q_{sat} - q_{FA})}{1 - \alpha} \quad (70)$$

$$P = -\frac{\frac{\omega_c}{g}\Delta q_{v,trop}}{1 - \alpha} \quad (71)$$

Here,  $\Delta q_{v,trop} = RH_c q_{sat} - q_{FA}$  is the difference in water vapor between the boundary layer and outflow layer. Note that  $P$  will be positive because  $\omega_c$  is negative (upward motion in the convective region) and  $RH_c q_{sat} \gg q_{FA}$ . Importantly, it can be shown that the total surface precipitation is equal to the total surface evaporation, i.e., that  $\pi l_c^2 P = E$  assuming that mass is balanced (see Appendix). Note that  $E = \pi l_c^2 \alpha P + 2\pi \int_{l_c}^{l_d} (F_q)_s r dr$  is the total evaporation. This shows that the water budget is balanced in the simple model.

The energy balance in the convective region free troposphere is now derived. We start with the conservation of moist static energy in the convective region free troposphere,  $h_c = s + L_v q_{v,s}$ , which is given by:

$$\nabla \cdot \mathbf{u}_c h_c + \frac{\partial(\omega_c h_c)}{\partial p} = Q_c + g L_v \frac{\partial F_q}{\partial p} \quad (72)$$

Here,  $Q_c$  is the radiative heating rate in the convective region in  $\text{J s}^{-1} \text{kg}^{-1}$ .  $F_q$  is the turbulent flux of water vapor from the convective region boundary layer and is proportional to  $\alpha P$ , as previously discussed. Using the fact that  $u_c = 0$  and  $\omega_c$  is uniform yields:

$$\omega_c \frac{\partial h_c}{\partial p} = Q_c + g L_v \frac{\partial F_q}{\partial p} \quad (73)$$

$$\omega_c \frac{\partial h_c}{\partial p} = Q_c + g L_v \frac{\partial F_q}{\partial p} \quad (74)$$

Integrating (21) from  $p = p_{BL}$  to  $p = p_{out}$  yields:

$$\omega_c (\Delta s_{trop} + L_v \Delta q_{v,trop}) = \int_{p_{out}}^{p_{BL}} \frac{Q_c}{\rho} dp + g L_v F_q(p_{BL}) \quad (75)$$

Using the definition of  $F_q(p_{BL})$  and substituting (16) for  $P$  yields:

$$\omega_c(\Delta s_{trop} + L_v \Delta q_{v,trop}) - g L_v F_q(p_{BL}) = \int_{p_{out}}^{p_{BL}} Q_c dp \quad (76)$$

$$\omega_c(\Delta s_{trop} + L_v \Delta q_{v,trop}) - g L_v \alpha P = \int_{p_{out}}^{p_{BL}} Q_c dp \quad (77)$$

$$\omega_c(\Delta s_{trop} + L_v \Delta q_{v,trop}) + L_v \frac{\alpha}{1-\alpha} \omega_c \Delta q_{v,trop} = \int_{p_{out}}^{p_{BL}} Q_c dp \quad (78)$$

$$\omega_c \left[ \Delta s_{trop} + \left( 1 + \frac{\alpha}{1-\alpha} \right) L_v \Delta q_{v,trop} \right] = \int_{p_{out}}^{p_{BL}} Q_c dp \quad (79)$$

Defining the net radiative heating in the convective region free troposphere as,  $\hat{Q}_c = \int_{z_{BL}}^{z_{out}} \rho Q_c dz$

and using hydrostatic balance with a change of variables on the RHS of (79) yields:

$$\omega_c = \frac{g \hat{Q}_c}{\Delta s_{trop} + \left( 1 + \frac{\alpha}{1-\alpha} \right) L_v \Delta q_{v,trop}} \quad (80)$$

Using (71) in (80), It can be shown that (80) is equivalent to:

$$\omega_c = \frac{g \hat{Q}_c + g L_v P}{\Delta s_{trop}} \quad (81)$$

Hence,  $\omega_c$  is given by a balance between adiabatic cooling and the sum of radiative cooling and condensation warming, as previously discussed. (80) can also be re-written as:

$$\omega_c = \frac{g \hat{Q}_c + g L_v \alpha P}{\Delta h_{trop}} \quad (82)$$

Importantly, (81) can be used to show that energy is conserved over the entire domain, assuming that mass is balanced and the energy is balanced in the dry region. Starting with

conservation of mass, (49), and using (81) and (26):

$$\omega_d(l_d^2 - l_c^2) = -\omega_c l_c^2 \quad (83)$$

$$\frac{g\hat{Q}_d}{\Delta s_{trop}}(l_d^2 - l_c^2) = -\frac{g\hat{Q}_c + gL_v P}{\Delta s_{trop}}l_c^2 \quad (84)$$

$$-\hat{Q}_d(l_d^2 - l_c^2) - \hat{Q}_c l_c^2 = l_c^2 L_v P \quad (85)$$

(85) states that the total radiative cooling over the domain must be balanced by the total condensation (or equivalently, the total evaporation).

*Convective Region Outflow Layer.* The convective region outflow layer starts at the prescribed pressure level  $p_{out} = 150$  hPa and extends to the prescribed tropopause height at  $p_t = 100$  hPa. The outflow layer is assumed to passively transport the moist static energy from the top of the deep convective region, into the dry region outflow layer. Specifically, we assume that outflow layer is well-mixed, in steady-state, and has uniform moist static energy  $h_{out} = s_{out} + L_v q_{FA}$ , where  $q_{FA} = q_{v,s}(T(p_{out}))$ . We additionally assume that the deep convection detrains into the bottom of the outflow layer with detrainment rate  $D_c = -\rho w_c = \frac{\omega_c}{g}$ . This results in three equations for the convective region outflow layer, valid for  $0 < r < l_c, p_t < p < p_{out}$ :

$$u_{out}(r) = \frac{\omega_c}{2\delta p_{out}}r \quad (86)$$

$$q_v = q_{v,s}(T(p_{out})) = q_{FA} \quad (87)$$

$$Q_{c,out} = 0 \quad (88)$$

Here,  $\delta p_{out} = p_{out} - p_t$  is the pressure thickness of the outflow layer. The net radiative heating in the convective region outflow layer is denoted by  $Q_{c,out}$ . (86) is obtained with the continuity equation, similar to  $u_{BL}(r)$ . (88) is obtained starting with conservation of moist static energy in the convective region outflow layer:

$$\nabla \cdot (\delta p_{out} \mathbf{u}_{out} h_{out}) = \omega_c h_{out} + g Q_{c,out} \quad (89)$$

Using the fact that the layer is well-mixed, in steady-state, and  $h_{out}$  is horizontally uniform, yields:

$$h_{out} \nabla \cdot \delta p_{out} \mathbf{u}_{out} = \omega_c h_{out} + g Q_{c,out} \quad (90)$$

$$h_{out} \omega_c = \omega_c h_{out} + g Q_{c,out} \quad \text{by continuity} \quad (91)$$

$$\implies Q_{c,out} = 0. \quad (92)$$

*Dry Region Inflow Layer.* The dry region inflow layer is essentially identical to the convective region outflow layer, except that the downward mass flux into the underlying convective region free troposphere is given by  $D_d = -\rho w_d = \frac{\omega_d}{g}$ . This results three equations, similar to the convective region outflow layer, and valid for  $l_c < r < l_d$ ,  $p_t < p < p_{out}$ :

$$u_{out}(r) = -\frac{\omega_d}{2\delta p_{out}} \frac{(l_d^2 - r^2)}{r} \quad (93)$$

$$q_v = q_{v,s}(T(p_{out})) = q_{FA} \quad (94)$$

$$Q_{d,out} = 0 \quad (95)$$

The derivations for (93) and (95) are essentially identical to the previously shown derivations for  $u_{out}$  in the convective region outflow layer.

TABLE 7.1. Coupled Simple Model Equations

|        |  |
|--------|--|
| Mass   | $\omega_c l_c^2 = -\omega_d(l_d^2 - l_c^2)$  |
| Water  | $RH_c = 1 + \frac{2\hat{z}(q_{FA} - q_{sat})}{q_{sat}(l_d^2 - l_c^2)} \left[ l_c + \hat{z} - (\hat{z} + l_d)e^{\frac{l_c - l_d}{\hat{z}}} \right]$ |
| Energy | $\omega_c = \frac{g\hat{Q}_c}{\Delta s_{trop} + (1 + \frac{\alpha}{1-\alpha})Lv\Delta q_{v,trop}}$   |

TABLE 7.2. Uncoupled Simple Model Equations

|        |  |
|--------|--|
| Mass   | $u_{BL}(r) = \begin{cases} -\frac{\omega_d}{2\delta p_{BL}} \frac{(l_d^2 - r^2)}{r}, & l_d < r < l_c \\ \frac{\omega_c}{2\delta p_{BL}} r, & 0 < r < l_c \end{cases}$    |
|        | $u_{out}(r) = \begin{cases} -\frac{\omega_d}{2\delta p_{out}} \frac{(l_d^2 - r^2)}{r}, & l_d < r < l_c \\ \frac{\omega_c}{2\delta p_{out}} r, & 0 < r < l_c \end{cases}$ |
| Water  | $q_{FA} = q_{v,s}(T(p_{out}))$   |
|        | $P = -\frac{\frac{\omega_c}{g} \Delta q_{v,trop}}{1-\alpha}$   |
| Energy | $\omega_d = \frac{g\hat{Q}_d}{\Delta s_{trop}}$  |

In summary, the simple model has 8 unknown variables:  $\omega_c$ ,  $\omega_d$ ,  $l_c$ ,  $RH_c$ ,  $q_{FA}$ ,  $P$ ,  $u_{BL}$ , and  $u_{out}$  (see Figure 7.2 for reference). Therefore, we require 8 independent equations to obtain a solution. The equations are summarized in Table 7.1 and Table 7.2. Table 7.1 summarizes the coupled equations, involving  $\omega_c$ ,  $l_c$  and  $RH_c$ , whereas Table 7.2 summarizes the uncoupled equations. The coupled equations must be solved as a system and cannot be solved analytically because of the nonlinearity of the equation for  $RH_c$ . The uncoupled

equations can be solved directly. We have not included the surface evaporation,  $E$ , as an unknown because it can be shown that  $E$  is equivalent to  $\pi l_c^2 P$  if mass is balanced (see Appendix). This is an important result because it shows that the simple model conserves water in the domain-averaged sense. Additionally, note that the momentum budget has not been discussed in the introduction of the simple model equations. This is because the momentum budget introduces an additional unknown, the surface pressure, which is completely determined by the boundary layer wind field, as the density is assumed to be horizontally uniform in our simple model ( $\frac{\partial p}{\partial x} \sim \rho u$ ). Thus, we do not gain any information by including the surface pressure term because the boundary layer wind field is determined by mass continuity.

In the next section, we analyze the simple model equations and derive a useful expression for the convective fractional area,  $\sigma$  that provides insight about the types of solutions we should expect. Later, we discuss the prescribed variables and the solutions of the simple model. In particular, we will show the solutions for varying domain length,  $l_d$ , and discuss how the length of the convective region,  $l_c$ , changes with increasing domain size. We also highlight the bounds on the spatial scale of the simple model.

*7.2.3. Analysis.* Before showing the solutions we derive a useful expression for fraction of the domain occupied by the convective region,  $\sigma = l_c^2/l_d^2$ , by further manipulation of the equations in Table 7.1. The expression will provide some information about the different types of solutions we can expect. Starting with conservation of mass, (49):

$$\omega_d(l_d^2 - l_c^2) = -\omega_c l_c^2 \tag{96}$$

Dividing by both sides by  $l_c^2$  yields:

$$\omega_d \left( \frac{1}{\sigma} - 1 \right) = -\omega_c \quad (97)$$

$$\frac{1}{\sigma} = 1 - \frac{\omega_c}{\omega_d} \quad (98)$$

$$\sigma = \frac{1}{1 - \frac{\omega_c}{\omega_d}} \quad (99)$$

Using (26) and (80) to substitute for  $\omega_c$  and  $\omega_d$  (i.e. the energy balances for the dry region and convective region free troposphere) yields:

$$\sigma = \left[ 1 - \frac{\hat{Q}_c}{\hat{Q}_d} \left( \frac{\Delta s_{trop}}{\Delta s_{trop} + \left(1 + \frac{\alpha}{1-\alpha}\right) L_v \Delta q_{v,trop}} \right) \right]^{-1} \quad (100)$$

Or equivalently:

$$\sigma = \left[ 1 - \frac{\hat{Q}_c}{\hat{Q}_d} \left( \frac{\Delta s_{trop}}{\Delta h_{trop} + \frac{\alpha}{1-\alpha} L_v \Delta q_{v,trop}} \right) \right]^{-1} \quad (101)$$

And:

$$\sigma = \left[ 1 - \frac{\hat{Q}_c}{\hat{Q}_d} \left( \frac{\Delta s_{trop}}{\Delta h_{trop,eff}} \right) \right]^{-1} \quad (102)$$

Here, we make the definition:

$$\Delta h_{trop,eff} = \Delta h_{trop} + \frac{\alpha}{1-\alpha} L_v \Delta q_{v,trop} \quad (103)$$

$\Delta h_{trop,eff}$  can be interpreted as an effective tropospheric difference in moist static energy which takes into account the energy associated with water vapor that has been added to the lower troposphere as a result of sea-surface evaporation in the convective region. Note that when  $\alpha = 0$ ,  $\Delta h_{trop,eff} = \Delta h_{trop}$ . Now, it must be true that  $0 \leq \sigma \leq 1$ , so that we must have:

$$0 \leq \frac{1}{1 - \gamma} \leq 1 \quad (104)$$

Here, we introduce the definition:

$$\gamma = \frac{\hat{Q}_c}{\hat{Q}_d} \left( \frac{\Delta s_{trop}}{\Delta h_{trop,eff}} \right) \quad (105)$$

Multiplying (104) by  $1 - \gamma$ , yields two inequalities that must be true:

$$0 \leq 1 \quad \text{and} \quad (106)$$

$$1 \leq 1 - \gamma \quad (107)$$

Since (106) is always satisfied, (104) is equivalent to (107). Simplifying (107) yields:

$$\begin{aligned} 0 &\leq -\gamma \\ \gamma &\leq 0 \\ \frac{\hat{Q}_c}{\hat{Q}_d} \left( \frac{\Delta s_{trop}}{\Delta h_{trop,eff}} \right) &\leq 0 \end{aligned} \quad (108)$$

Importantly, (108) contains all possible physical constraints on the simple model, because it contains the energy, mass, and water balance constraints.

The physical constraints given by (108) are now discussed. Note that the radiative heating rate in the dry region,  $\hat{Q}_d$ , is always negative. Likewise,  $\Delta s_{trop} = s_{BL} - s_{trop}$  is always negative because the prescribed moist adiabatic temperature profile is stable to dry adiabatic motion, whereas  $\frac{\alpha}{1-\alpha} L_v \Delta q_{v,trop}$  is always positive. However,  $\Delta h_{trop} = \Delta s_{trop} + L_v (RH_c q_{sat} - q_{FA})$  can be positive or negative, depending on the relative humidity in the convective region boundary layer,  $RH_c$ . In other words, the sign of  $\Delta h_{trop,eff}$  is completely determined by  $RH_c$ . For example, if  $RH_c$  is sufficiently high, we might expect  $\Delta h_{trop,eff}$  to be positive. Therefore, the sign of the LHS of (108) essentially depends on the sign of  $\hat{Q}_c$  and  $\Delta h_{trop,eff}$ .

An important point to make is that we analyze the constraint (108) with respect to varying domain size,  $l_d$ . We do this in order to investigate the how the solutions will change with respect with  $l_d$ . This means that (108) will only ever be violated if  $RH_c$  actually changes with increasing  $l_d$ . It is possible that  $RH_c$  is insensitive to  $l_d$ , in which case (108) may always be valid. Recall that the expression for  $RH_c$  is quite complicated and depends on both  $l_d$  and  $l_c$ :

$$RH_c = 1 - \frac{2\hat{z}(q_{sat} - q_{FA})}{q_{sat}(l_d^2 - l_c^2)} \left[ l_c + \hat{z} - (\hat{z} + l_d) e^{\frac{l_c - l_d}{\hat{z}}} \right] \quad (109)$$

We will later show that  $RH_c$  is an *increasing* function of  $l_d$ . It is important to keep this in mind throughout the following discussion.

Returning to the physical constraint (108), we can see that (108) is true if either:

- (1)  $\hat{Q}_c > 0$ , while  $\Delta h_{trop,eff} < 0$ , or
- (2)  $\hat{Q}_c < 0$ , while  $\Delta h_{trop,eff} > 0$ .

From the previous discussion, (1) implies that solutions with  $RH_c$  lower than some critical relative humidity,  $RH_{c,crit}$ , will require radiative heating in the convective region free troposphere, where we define  $RH_{c,crit}$  to be the relative humidity that yields  $\Delta h_{trop,eff} = 0$ . Likewise, (2) implies that solutions with  $RH_c > RH_{c,crit}$  will require radiative cooling in the convective region free troposphere. The expression for  $RH_{c,crit}$  is given by:

$$\Delta s_{trop} + L_v \left(1 + \frac{\alpha}{1 - \alpha}\right) (RH_{c,crit} q_{sat} - q_{FA}) = 0 \quad (110)$$

and since  $q_{FA} \approx 0$ :

$$RH_{c,crit} = \frac{-\Delta s_{trop}}{L_v q_{sat} \left(1 + \frac{\alpha}{1 - \alpha}\right)} \quad (111)$$

This gives  $RH_{c,crit} \approx 87\%$  with  $\alpha = 0$ . Note that  $RH_{c,crit}$  decreases with increasing surface evaporation in the convective region,  $\alpha$ . This can be seen in Figure 7.3, where we have plotted  $\sigma$  as a function of  $\alpha$  and  $RH_c$  and the blue line denotes  $RH_{c,crit}$ .

Therefore, we can rewrite (1) and (2) as:

$$(3) \hat{Q}_c > 0, \text{ while } RH_c < RH_{c,crit}, \text{ or}$$

$$(4) \hat{Q}_c < 0, \text{ while } RH_c > RH_{c,crit}$$

Importantly, (144) shows that as  $RH_c$  approaches  $RH_{c,crit}$ ,  $\sigma$  approaches zero because  $\Delta h_{trop,eff} = 0$  when  $RH_c = RH_{c,crit}$ . This can also be seen in Figure 7.3. As we have previously discussed that  $RH_c$  increases with  $l_d$ , this means that there exists an  $l_d$  such that  $RH_c$  approaches  $RH_{c,crit}$  and hence  $\sigma$  approaches zero.

We can loosely interpret the spatial scale of the simple model,  $l_d$ , as being *bounded* if  $\sigma$  approaches zero at a finite value of  $l_d$ , because this implies that the convective region

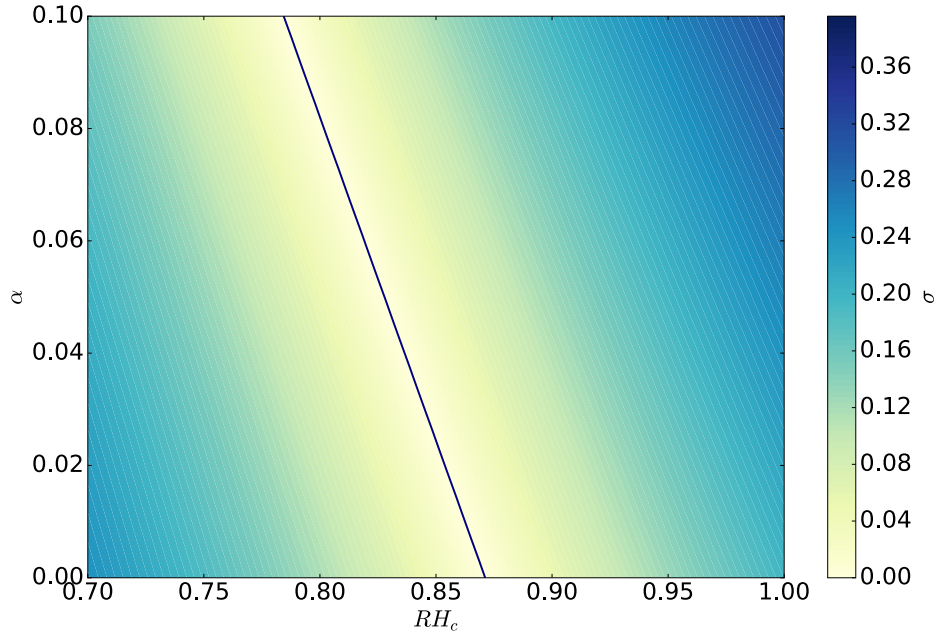


FIGURE 7.3. The convective fractional area of the simple model,  $\sigma$ , plotted in  $\alpha$ - $RH_c$  space.  $RH_c$  is the relative humidity in the convective region boundary layer.  $\alpha$  indicates the strength of surface evaporation in the convective region boundary layer. The blue line denotes  $RH_{c,crit}$ . To the left of the blue line is the radiative heating regime, and to the right of the blue line is the radiative cooling regime.

cannot expand indefinitely for increasing  $l_d$ . Strictly speaking, when  $\sigma$  approaches zero at a finite value  $l_d$ , this implies that  $l_c$  approaches zero and the vertical velocity in the convective region,  $\omega_c$ , approaches infinity. This scenario can be interpreted as a single cumulonimbus cloud at  $r = 0$ . Under these conditions, it is fair to say that the convection is not aggregated. Therefore, we interpret the length scale  $l_d$  at which  $\omega_c$  begins to increase very rapidly as being a bound on the spatial scale of the simple model of the aggregated state,  $l_d$ . Likewise, if  $\sigma$  approaches a non-zero constant for increasing  $l_d$ , we can interpret the spatial scale of the simple model as being *unbounded*.

We emphasize that it is important to determine whether the unbounded solutions are consistent with both the simulations and observed convection. For now, we simply show

that the spatial scale of the simple model is bounded purely from a theoretical perspective. Importantly, we have found that the only way for  $\sigma$  to approach zero and hence for  $l_d$  to be bounded is for:

$$-\frac{\hat{Q}_c}{\hat{Q}_d} \left( \frac{\Delta S_{trop}}{\Delta h_{trop,eff}} \right) \rightarrow \infty \quad \text{at finite } l_d \quad (112)$$

Here, we have referred back to (144). In other words,  $l_d$  is bounded if either:

$$(5) \Delta h_{trop,eff} \rightarrow 0^-, \text{ while } \hat{Q}_c > 0, \text{ or}$$

$$(6) \Delta h_{trop,eff} \rightarrow 0^+, \text{ while } \hat{Q}_c < 0.$$

Here, the  $\rightarrow x^-$  notation denotes approaching  $x$  from values less than  $x$ , with changing  $l_d$ . Likewise, the  $\rightarrow x^+$  notation denotes approaching  $x$  from values greater than  $x$ , with changing  $l_d$ . Now since the sign of  $\Delta h_{trop,eff}$  is completely determined by the sign of  $RH_c - RH_{c,crit}$  we can rewrite the conditions (5) and (6) as:

$$(7) RH_c \rightarrow RH_{c,crit}^-, \text{ while } \hat{Q}_c > 0, \text{ or}$$

$$(8) RH_c \rightarrow RH_{c,crit}^+, \text{ while } \hat{Q}_c < 0.$$

Recall that we have previously discussed that  $RH_c$  is an *increasing* function of  $l_d$ . This implies that (7) is an upper bound for  $l_d$  because increasing  $l_d$  will ultimately lead to increasing  $RH_c$  and hence the approach of  $RH_{c,crit}$  from below (i.e. (7) will be satisfied). On the other hand, this implies that condition (8) is a lower bound on  $l_d$ . In other words, decreasing  $l_d$  will lead to decreasing  $RH_c$  and hence the approach of  $RH_{c,crit}$  from above (i.e. (8) will be satisfied). (7) and (8) also imply that  $l_d$  is only bounded above if we prescribe a radiative heating in the convective region, but  $l_d$  is bounded below and unbounded above if we prescribe a radiative cooling in the convective region. This is illustrated in Figure 7.3. Note

that the radiative heating solutions are confined to  $RH_c$  that are less than  $RH_{c,crit}$ , which is the area to left of the blue line in Figure 7.3. On the other hand, the radiative cooling solutions are confined to  $RH_c$  greater than  $RH_{c,crit}$ , which is to the right of the blue line. Furthermore, in the radiative heating regime, we can see that  $\sigma$  decreases with increasing  $RH_c$  (and hence  $l_d$ ) from Figure 7.3. On the other hand. in the radiative cooling regime, we can see that  $\sigma$  increases with increasing  $RH_c$  (and hence  $l_d$ .) We return to these points later.

We emphasize that these are the *theoretical* bounds on the spatial scale of the simple model. Later, we show that the unbounded solutions are unphysical and so we will introduce an additional physical constraint to the simple model, which acts as an upper bound on  $l_d$  for the radiative cooling solutions.

In the radiative cooling regime ( $\hat{Q}_c < 0$ ), the lower bound on  $l_d$  can be interpreted as the length scale at which the convective region boundary layer becomes too dry (i.e.  $RH_c < RH_{c,crit}$  and hence  $\Delta h_{trop,eff} < 0$ ), such that the condensation warming in the convective region free troposphere is too weak to balance the sum of the radiative and adiabatic cooling. This can be seen by rewriting the expression for  $\omega_c$ , (80), in terms of  $\Delta h_{trop,eff}$ , i.e.:

$$\omega_c = \frac{g\hat{Q}_c}{\Delta h_{trop,eff}} \quad (113)$$

$$\omega_c \Delta h_{trop,eff} = g\hat{Q}_c \quad (114)$$

$$\omega_c \left[ \Delta s_{trop} + L_v \left( 1 + \frac{\alpha}{1-\alpha} \right) \Delta q_{v,trop} \right] = g\hat{Q}_c \quad (115)$$

$$\omega_c \left[ \Delta s_{trop} + L_v \frac{\Delta q_{v,trop}}{1-\alpha} \right] = g\hat{Q}_c \quad (116)$$

In particular, note that if  $\Delta h_{trop,eff} < 0$ , then for  $\omega_c < 0$  (upward motion) we have:

$$\omega_c \left[ \Delta s_{trop} + L_v \frac{\Delta q_{v,trop}}{1 - \alpha} \right] > 0 \quad (117)$$

$$\omega_c \Delta s_{trop} - g L_v P > 0 \quad (118)$$

$$\omega_c \Delta s_{trop} - g L_v P > g \hat{Q}_c \quad (119)$$

$$\omega_c \Delta s_{trop} - g \hat{Q}_c > g L_v P \quad (120)$$

Here, we have simply used the expression for the surface precipitation,  $P$ , (71), and also used the fact that  $\hat{Q}_c < 0$ . Importantly, (120) states that the condensation warming is less than the sum of the adiabatic and radiative cooling in the convective region free troposphere if both  $\hat{Q}_c < 0$  and  $\Delta h_{trop,eff} < 0$ . In other words, energy will be unbalanced in the convective region if  $\Delta h_{trop,eff} < 0$  in the radiative cooling regime. A similar line of reasoning can be used to show that, in the radiative heating regime ( $\hat{Q}_c > 0$ ), the adiabatic cooling will be too weak to balance the sum of the radiative heating and condensation warming if  $\Delta h_{trop,eff} > 0$ .

7.2.4. *Solutions.* Before showing the solutions of the simple model, the prescribed variables are summarized in Table 7.2. Note that  $l_d$  is a prescribed variable but is not listed because we show the solutions as a function of  $l_d$ . The prescribed temperature profile is a moist adiabat given by the equivalent potential temperature at the surface and is horizontally uniform (see Figure 7.4). Note that this temperature profile results in a troposphere which is warmer than the simulations by approximately 4 K, but more importantly, the shape of the temperature profile is consistent with that of the simulations.

The tropopause height and boundary layer height were estimated from simulation results. We find the corresponding pressure at which  $\frac{\partial T}{\partial z}$  becomes noticeably large (see Figure 7.4),

TABLE 7.3. Simple Model Prescribed Variables

|             |                        |
|-------------|------------------------|
| $T_s$       | 302 K                  |
| $p_s$       | 1000 hPa               |
| $p_{BL}$    | 900 hPa                |
| $p_{out}$   | 150 hPa                |
| $p_t$       | 100 hPa                |
| $c_E$       | 0.001                  |
| $\hat{Q}_d$ | -1.0 K/day             |
| $\hat{Q}_c$ | -0.6, 0.6 K/day        |
| $\alpha$    | 0.00, 0.05, 0.08, 0.10 |

and the boundary layer height is similarly estimated as the point at which  $\frac{\partial s}{\partial z}$  becomes sufficiently far from zero. This yields approximate values for  $p_t$  and  $p_{BL}$ .

The radiative cooling rates,  $\hat{Q}_c$  and  $\hat{Q}_d$ , were also estimated from the simulation results. The vertically averaged radiative heating rate in the mesoscale convective region was calculated to be approximately -0.6 K/day, and relatively insensitive to the domain size. Likewise, the vertically averaged radiative heating rate in the dry region was approximately -1.0 K/day. We experiment with radiative heating in the convective region because, as previously discussed, the solution regime depends on the sign of the radiative heating rate.

The fraction of precipitation in the convective region that is equal to the surface evaporation, i.e.,  $\alpha$ , was computed from Figure 4.3.  $\alpha$  is computed by calculating the average precipitation over the region where the precipitation is not very small. For example, in the small domain case, this region would be  $0 < \hat{r} < 0.2$ . The surface evaporation is calculated over the same region to get  $\alpha$ . Note that this results in values of precipitation of 81.2, 58.9, and 37.5 mm/day and evaporation of 3.7, 4.2, 4.6 mm/day, so that  $\alpha = 0.05, 0.07$  and

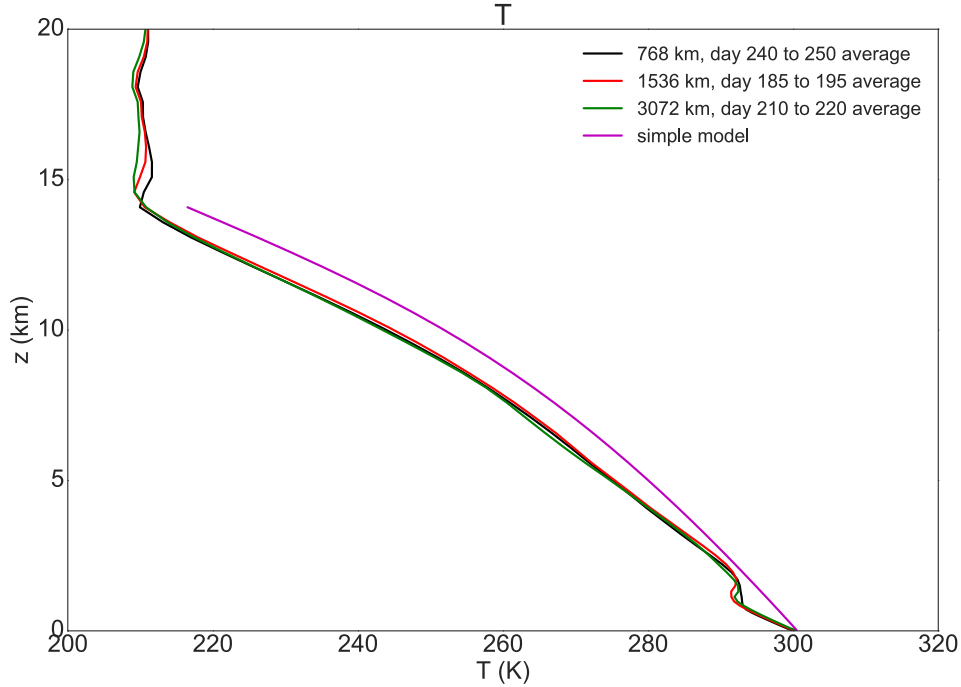


FIGURE 7.4. The prescribed temperature profile for the simple model (magenta). The temperature profiles from the simulations are plotted for reference purposes. The simple model temperature profile is given by a moist adiabat with  $\theta_e = 367$  K, the equivalent potential temperature at the surface and is calculated from  $p_s = 1000$  hPa to  $p_{out} = 200$  hPa.

0.12, for the small, medium and large domain, respectively. Evidently,  $\alpha$  increases as the convective region broadens, however we use a constant value of  $\alpha$  for simplicity. Note that the prescribed value of  $\alpha = 0.08$  is simply the average of the  $\alpha$  computed from the different domain cases. We also experiment with a few different values of  $\alpha$ , including  $\alpha = 0$  (no surface evaporation in the convective region), in order to investigate the effect of the surface evaporation in the convective region boundary layer on the spatial scale of the convective region.

We now show the solutions for  $\sigma$ ,  $l_c$ ,  $\omega_c$ ,  $RH_c$ , and  $P$  for varying  $l_d$ . The solutions for  $u_{BL}$  and  $u_{out}$  are omitted for brevity. The solutions are found numerically with the built-in Python function, *fsolve*, until convergence is achieved as the system of equations cannot be

solved analytically. Also note that  $\omega_d$  is insensitive to domain size. The prescribed radiative cooling in the dry region and temperature profile essentially give  $\omega_d$ , which results in a vertical velocity of  $\approx -0.001$  m/s, consistent with the order of magnitude of the  $w_d$  from our simulations.

*Convective Region Radiative Cooling.* First, we show solutions corresponding to net radiative cooling in the convective region free troposphere, i.e.,  $\hat{Q}_c = -0.6$  K/day, and for varying  $\alpha$  and  $l_d$  (see Figure 7.5). Notice that these solutions are unbounded above, in the sense that  $\sigma$  approaches a constant value as  $l_d$  increases, but are bounded below, in the sense that  $\sigma$  approaches zero as  $l_d$  decreases. As  $\sigma$  approaches zero,  $\Delta h_{trop,eff}$  approaches zero from above, and  $RH_c$  approaching the critical value  $RH_{c,crit}$  from above. This is consistent with the discussion in the *Analysis* section (7.2.3). This occurs around  $l_d = 5000$  km. Strictly speaking, the numerical solver starts to diverge before  $\Delta h_{trop,eff}$  reaches zero and  $RH_c$  reaches  $RH_{c,crit}$ . We interpret this behavior as being due to  $\omega_c$  rapidly increasing in this vicinity, which makes it increasingly more difficult for the numerical solver to find a solution.

The value of  $\sigma$  that is approached when  $l_d \rightarrow \infty$  can be estimated by using (144), and by noting the fact that  $RH_c$  approaches a constant value which cannot exceed unity. For example, for  $\alpha = 0$ , we can see that  $RH_c$  approaches 0.95 with increasing  $l_d$ . So, using  $\hat{Q}_c = -0.6$  K/day,  $\Delta s_{trop} \approx -50,000$  J,  $q_{sat} = q_{v,s}(T_s)$ , we can use (33) to calculate that  $\sigma$  will approach  $\approx 0.15$ , which is consistent with the numerical solutions of  $\sigma$ . We can see that higher values of  $\alpha$  tend to increase  $\sigma$ , and also decrease the lower bound on  $l_d$ . This is because with higher surface evaporation,  $RH_{c,crit}$  will be lower, and so less boundary layer fetch is required in order to reach  $RH_{c,crit}$ . In other words, higher surface evaporation means

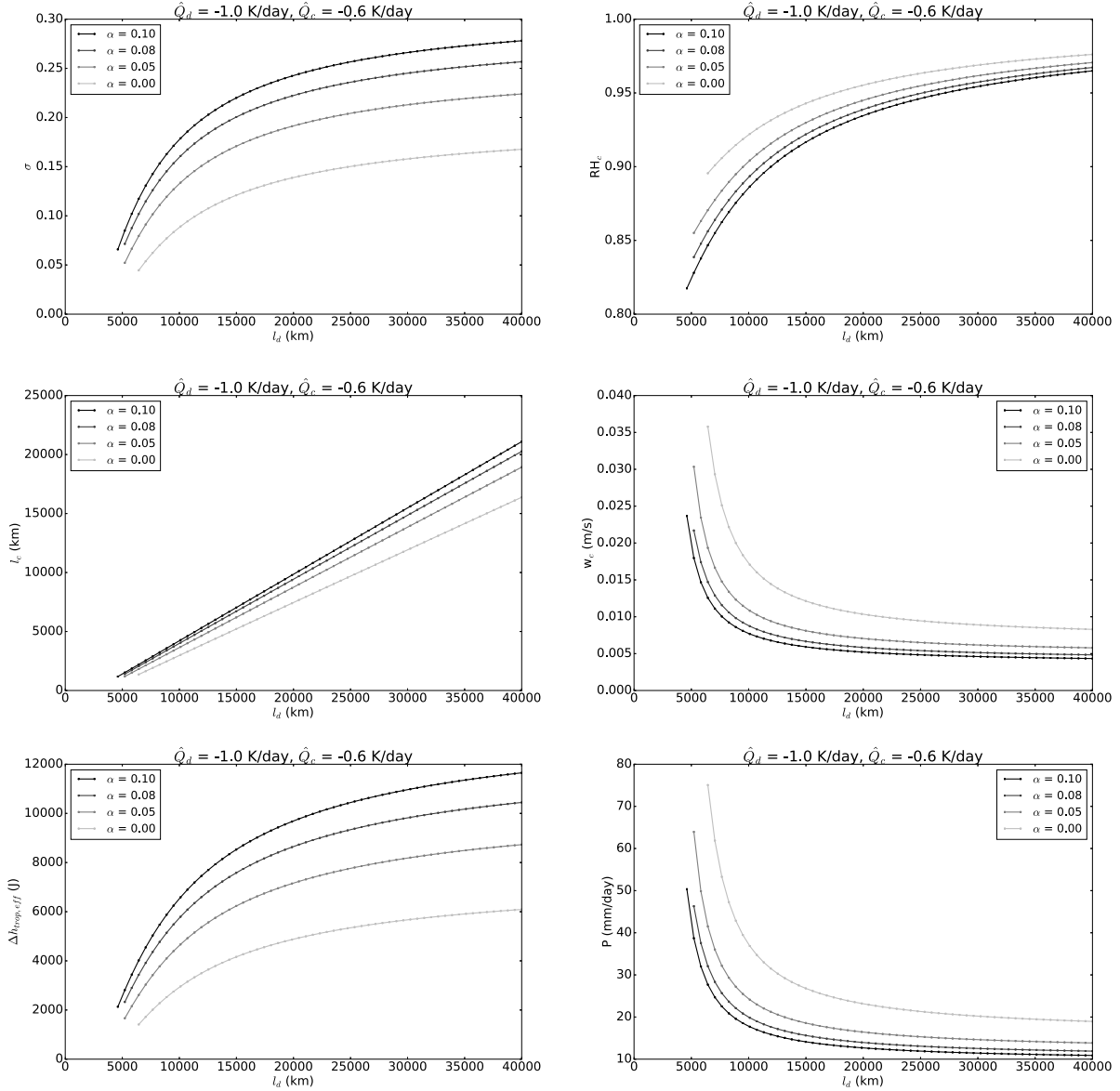


FIGURE 7.5. Solutions of the simple model of the aggregated RCE state for  $\hat{Q}_d = -1.0$  K/day,  $\hat{Q}_c = -0.6$  K/day. Solutions are plotted as a function of the  $l_d$ , the distance to the outer edge of the dry region. Multiple curves are plotted for varying  $\alpha$ , which is a prescribed constant of proportionality between surface evaporation and precipitation in the convective region (e.g. higher  $\alpha$  means more surface evaporation). Top left: the convective fractional area,  $\sigma = l_c^2/l_d^2$ . Top right: the relative humidity in the convective region boundary layer,  $RH_c$ . Mid left: the length of the convective region,  $l_c$  (km). Mid right: the vertical velocity in the convective region free troposphere,  $w_c$  (m/s). Bottom left: the effective tropospheric difference in moist static energy (defined in text),  $\Delta h_{trop,eff}$ . Bottom right: the surface precipitation,  $P$  (mm/day).

more water vapor will be added into the convective region free troposphere, which means that less water vapor in the convective region boundary layer is required to drive convection. Thus,  $\omega_c$  rapidly increases at a lower  $RH_{c,crit}$ , and hence a lower  $l_d$ . Additionally, we can see that higher values of  $\alpha$  are associated with lower precipitation, a larger convective region and a weaker convective updraft. It is interesting that our simulation results are consistent with this behavior as well.

*Convective Region Radiative Heating.* We now show solutions corresponding to net radiative heating in the convective region free troposphere,  $\hat{Q}_c = 0.6$  K/day. Recall that in our simulations, the convective region was radiatively cooling in the vertically averaged sense. It is instructive to prescribe a net radiative heating in the convective region despite the inconsistency with the simulations because the solutions have some properties that are more consistent with our simulation results, as compared to the radiative cooling solutions. In particular, we have seen that the solutions corresponding to radiative cooling in the convective region do not allow smaller scale ( $< 5000$  km) solutions, which is clearly inconsistent with the scale of the convective region in our simulations.

The solutions are shown in Figure 7.6. Note that these solutions correspond to scales that are smaller than that of the radiative cooling solutions ( $l_d < 5000$  km) and are bounded above, as expected. Note that  $RH_c$  approaches  $RH_{c,crit}$  from below and  $\Delta h_{trop,eff}$  approaches zero from below. This directly contrasts with the behavior of the radiative cooling solutions where  $RH_c > RH_{c,crit}$  and  $\Delta h_{trop,eff} > 0$ .

Another important feature of these solutions is that they correspond to a drier convective region boundary layer. In particular, note that for the smaller scale solutions ( $< 2000$  km), the relative humidity is extremely low at around 0.1 to 0.2. This highlights a deficiency

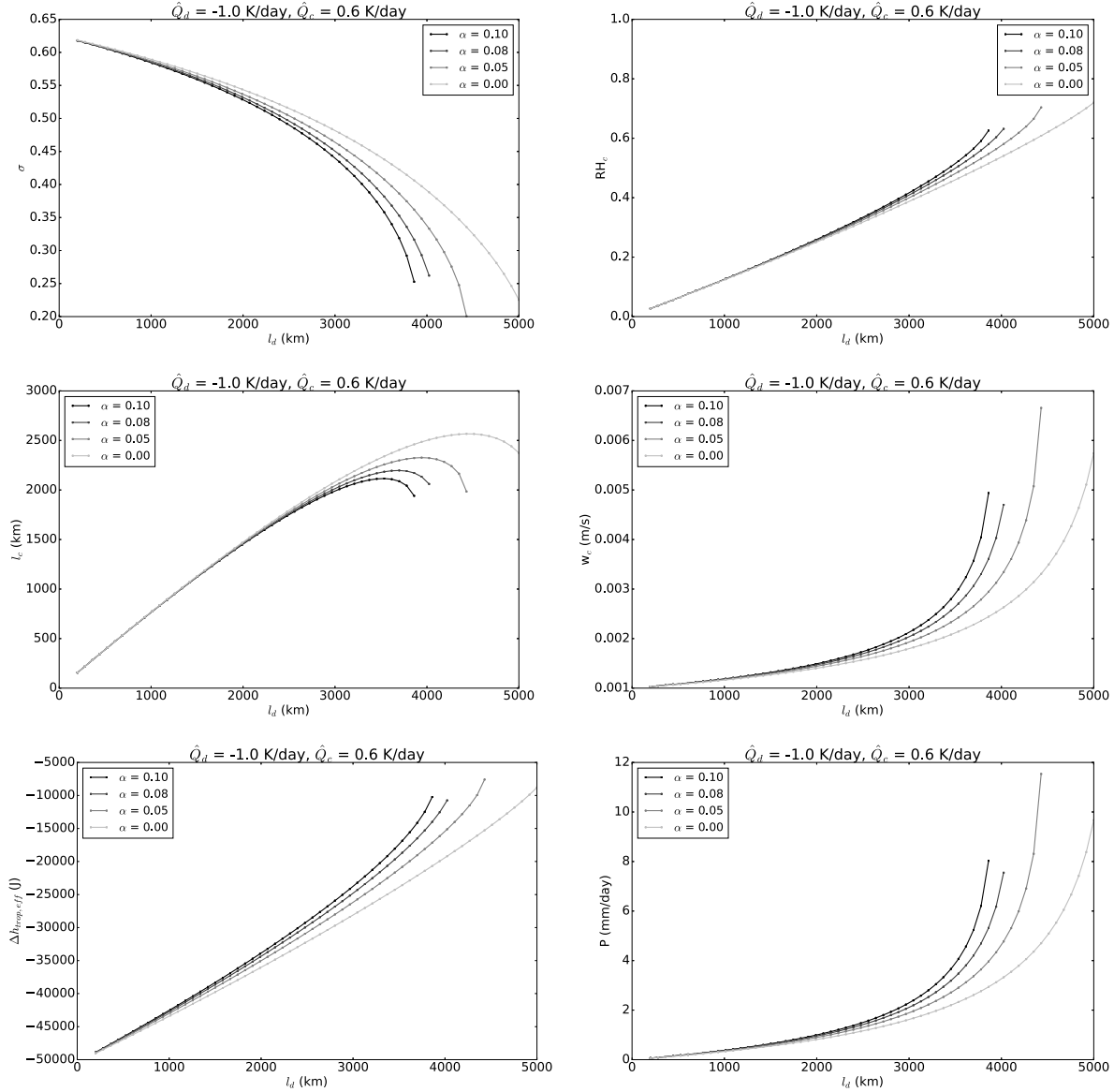


FIGURE 7.6. Solutions of the simple model of the aggregated RCE state for  $\hat{Q}_d = -1.0$  K/day,  $\hat{Q}_c = 0.6$  K/day. Solutions are plotted as a function of the  $l_d$ , the distance to the outer edge of the dry region. Multiple curves are plotted for varying  $\alpha$ , which is a prescribed constant of proportionality between surface evaporation and precipitation in the convective region (e.g. higher  $\alpha$  means more surface evaporation). Top left: the convective fractional area,  $\sigma = l_c^2/l_d^2$ . Top right: the relative humidity in the convective region boundary layer,  $RH_c$ . Mid left: the length of the convective region,  $l_c$  (km). Mid right: the vertical velocity in the convective region free troposphere,  $w_c$  (m/s). Bottom left: the effective tropospheric difference in moist static energy (defined in text),  $\Delta h_{trop,eff}$ . Bottom right: the surface precipitation,  $P$  (mm/day).

in the simple model, which is that there is no constraint on  $RH_c$ . In other words, deep convection is possible with any relative humidity in the convective region boundary layer. This is clearly not true in the real atmosphere, however, it is not necessarily obvious how we should constrain  $RH_c$  because deep convection can be triggered in a variety of ways. Thus, we simply allow  $RH_c$  to vary while keeping in mind that some solutions will be unphysical (e.g., the solutions where  $RH_c < 0.7$ ). This implies that most of the smaller scale solutions are quite unphysical and would never exist with a more realistic formulation of the convective region. It is also possible that the air in the dry region boundary layer requires unrealistically high fetch ( $l_d - l_c$ ) in order to reach high humidity, because the dry region free troposphere has very low relative humidity (i.e. the drying due to subsidence is unrealistically high). This could be remedied in future work by introducing an additional layer atop the boundary layer, which acts as a “moisture buffer” between the boundary layer and the free troposphere. Indeed, in our simulations we have seen that there is a shallow circulation with outflow from the convective region above the boundary layer. Notice, however, that  $RH_c$  becomes high as  $l_d$  is increased. In particular,  $RH_c$  approaches around 0.7 at around  $l_d = 5000$  km, which is much more physically reasonable. Thus, in the case of radiative heating in the convective region, we interpret the solutions that are closest to  $RH_{c,crit}$  as being physical solutions, while solutions far from  $RH_{c,crit}$  are more difficult to interpret.

Finally, notice that the bound on the spatial scale of the simple model decreases with increasing  $\alpha$ , which is consistent with what we saw with the radiative cooling solutions. The explanation is the same, i.e., that with higher surface evaporation more water vapor will be added into the convective region free troposphere, which means that less water vapor in the

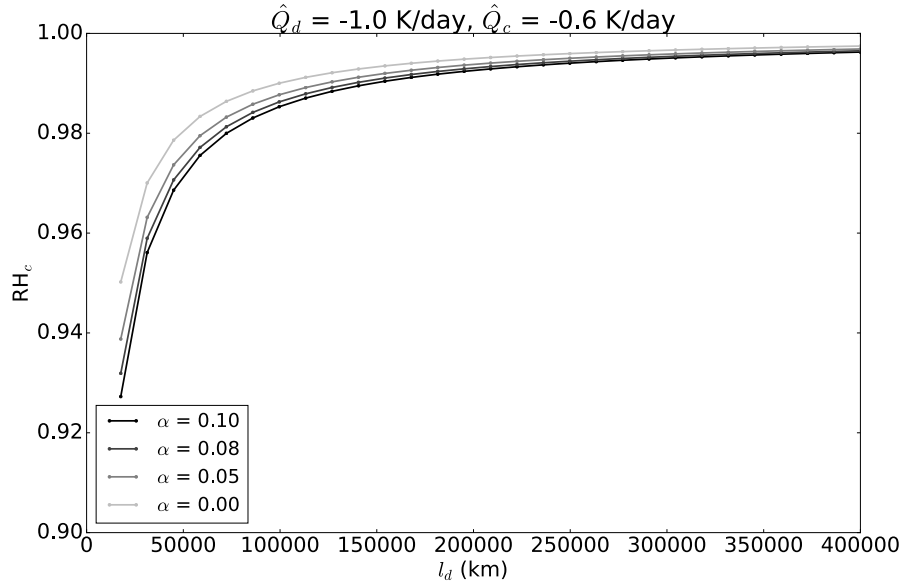


FIGURE 7.7. The convective region boundary layer relative humidity,  $RH_c$  for large scale solutions of the simple model radiative cooling regime.

convective region boundary layer is required to drive convection. Thus,  $\omega_c$  rapidly increases at a lower  $RH_{c,crit}$ , and hence lower  $l_d$ .

*Convective Region Boundary Layer Relative Humidity.* We now discuss the relationship between the convective region boundary layer relative humidity,  $RH_c$ , and the domain size,  $l_d$ . Importantly, note that  $RH_c$  *always* increases with respect to  $l_d$ . Indeed, even if we extend the domain size to unphysically large  $l_d$  ( $\sim 400,000$  km),  $RH_c$  is very slowly increasing with respect to  $l_d$ , and approaches unity (see Figure 7.7). This is a subtle but important point, and is true in both the radiative heating and radiative cooling regimes. Although the expression for  $RH_c$  is complicated, this behavior seems to be necessary in a cylindrical geometrical set-up of the aggregated RCE state. We describe this in more detail in the following.

First, note that if the boundary layer fetch decreased or was constant with domain size, the convective region would eventually occupy the entire domain and hence  $RH_c$  would steadily decrease with increasing domain size. This is because in cylindrical geometry,  $\sigma =$

$l_c^2/l_d^2$ , so that if the boundary layer fetch,  $l_d - l_c$ , is a constant,  $A$ , we would have:

$$\sigma = \frac{l_c^2}{l_d^2} = \frac{(l_d - A)^2}{l_d^2} \quad (121)$$

Importantly, we can clearly see that  $\sigma \rightarrow 1$  as  $l_d \rightarrow \infty$ . However, this could not happen because energy, mass, and water could not be balanced if the convective region occupied the entire domain. Therefore, the boundary layer fetch must *increase* with increasing domain size, and as a result, parcels of air will be more humid by the time they reach the convective region edge. In other words,  $RH_c$  must increase with increasing domain size.

*Convective Broadening.* We now discuss the relationship between the convective fractional area,  $\sigma$ , and the domain size,  $l_d$ . We focus on the relationship between  $\sigma$  and  $l_d$  in the radiative cooling regime. In the radiative cooling regime, recall that  $\sigma$  increases with  $l_d$  (see Figure 7.5). The explanation for this is simple. Importantly, as previously discussed, we know that the relative humidity in the convective region boundary layer must increase with domain size. This means that the energy available for supply into the convective region free troposphere is increasing with domain size, while the rate of energy loss from the convective region free troposphere (i.e. the radiative cooling) is constant with domain size. In other words,  $\Delta h_{trop,eff}$  must increase with domain size. Since the rate of energy supply to the convective region free troposphere is equal to the vertical velocity in the convective region multiplied by  $\Delta h_{trop,eff}$ , the vertical velocity must decrease. This can be seen from the conservation of moist static energy in the convective region free troposphere, i.e., equation

(80):

$$\omega_c = \frac{g\hat{Q}_c}{\Delta s_{trop} + \left(1 + \frac{\alpha}{1-\alpha}\right) L_v \Delta q_{v,trop}} \quad (122)$$

This can be re-written as:

$$\omega_c = \frac{g\hat{Q}_c}{\Delta h_{trop,eff}} \quad (123)$$

$$\omega_c \Delta h_{trop,eff} = g\hat{Q}_c \quad (124)$$

Importantly, recall that  $\Delta h_{trop,eff} > 0$  in the radiative cooling regime. Now, since  $\Delta h_{trop,eff}$  increases with  $l_d$  while the radiative cooling rate  $\hat{Q}_c$  is constant, then  $\omega_c$  must increase in magnitude. Additionally, since  $\omega_d$  is invariant with domain size, then by mass conservation,  $\sigma$  must increase with  $l_d$ . This can be clearly seen with equation (99):

$$\sigma = \frac{1}{1 - \frac{\omega_c}{\omega_d}} \quad (125)$$

Therefore, the reason that  $\sigma$  increases with domain size is essentially because the convective region boundary layer becomes more humid with domain size, while the rate of energy loss from the convective region free troposphere is invariant with domain size. Similar reasoning can be used to show that  $\sigma$  must decrease with domain size in the radiative heating regime. In particular, the vertical velocity must increase because  $\Delta h_{trop,eff}$  is negative and increasing with domain size in the radiative heating regime.

It is interesting that the relationship between  $\sigma$  and the domain size in the radiative cooling regime is similar to the relationship between  $\sigma_m$  and domain size in the simulations

(i.e. that both increase with domain size). We later discuss this in more detail in *Comparison to Simulations*.

*Convective Region Radiative Heating Sensitivity.* We briefly discuss the sensitivity of the solutions to the radiative heating rate in the convective region,  $\hat{Q}_c$ . It is important to note that, based on (111),  $\hat{Q}_c$  does *not* influence the value of  $RH_{c,crit}$ . Therefore, we conclude that the only way for the radiative heating rate to influence the bound on the spatial scale of the simple model is through the dependence of  $RH_c$  on  $l_d$ .

With a fixed domain size, we expect that if there is more radiative cooling in the convective region, there must be increased energy transport into the convective region in order to maintain a state of energy balance. Based on the previous discussion in *Convective Broadening*, this must be accomplished by an increase in vertical velocity in the convective region, and hence a decrease in  $l_c$ , by mass conservation. This means that, for a given  $l_d$ , the boundary layer fetch increases, and hence  $RH_c$  increases. As a result,  $RH_c$  would approach  $RH_{c,crit}$  at lower  $l_d$ . In other words, there is more relative humidity in the convective region boundary layer at a given domain size when the radiative cooling is higher in the convective region. Hence, convection can be sustained at smaller domain sizes when there is more radiative cooling in the convective region. Therefore we hypothesize that increased radiative cooling in the convective region decreases the lower bound on the spatial scale of the simple model (i.e.  $\Delta h_{trop,eff}$  approaches zero at a lower  $l_d$ ). In the radiative heating regime, similar reasoning can be used to hypothesize that decreased radiative heating must result in less relative humidity in the convective region boundary layer, and hence an increase in the upper bound of the spatial scale of the simple model. The numerical solutions confirm these hypotheses (see Figures 7.8 and 7.9).

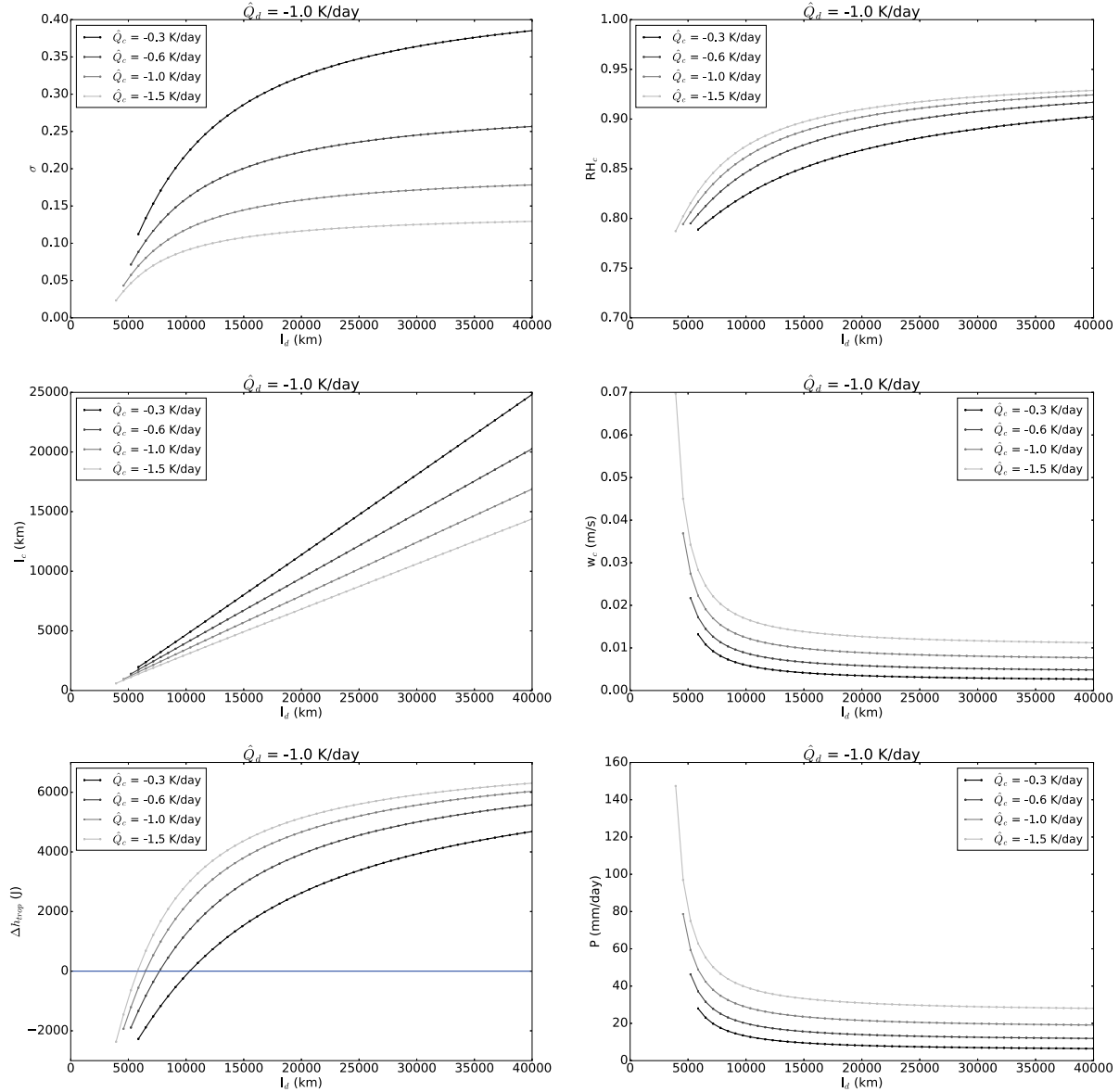


FIGURE 7.8. Solutions of the simple model of the aggregated RCE state for varying  $\hat{Q}_c < 0$ . Darker curves denote stronger net radiative heating rates (weaker radiative cooling) in the convective region. Note that  $\alpha = 0.08$  in all cases. Solutions are plotted as a function of the  $l_d$ , the distance to the outer edge of the dry region. Top left: the convective fractional area,  $\sigma = l_c^2/l_d^2$ . Top right: the relative humidity in the convective region boundary layer,  $RH_c$ . Mid left: the length of the convective region,  $l_c$  (km). Mid right: the vertical velocity in the convective region free troposphere,  $w_c$  (m/s). Bottom left: the tropospheric difference in moist static energy,  $\Delta h_{trop}$ . Bottom right: the surface precipitation,  $P$  (mm/day).

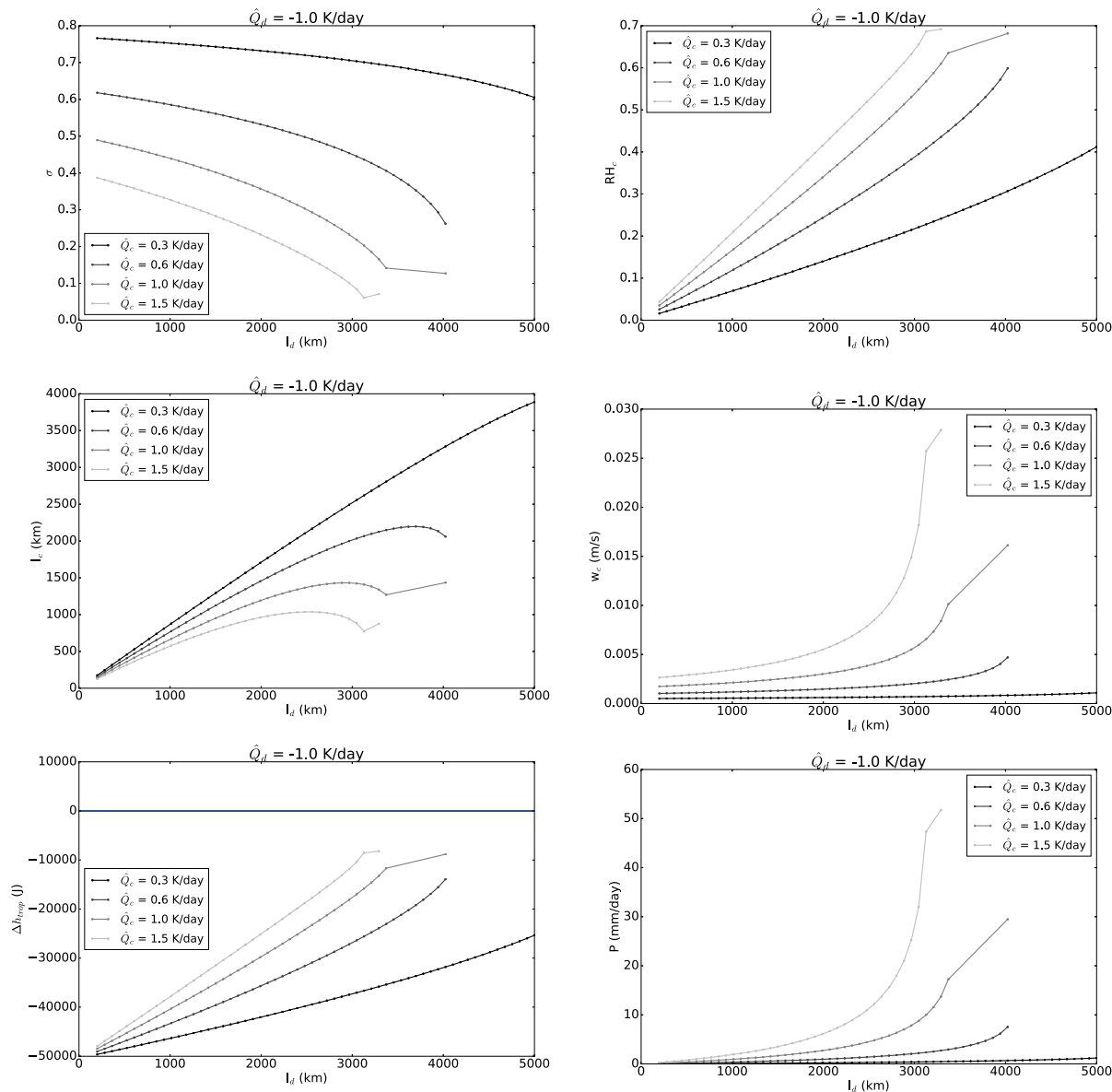


FIGURE 7.9. Solutions of the simple model of the aggregated RCE state for varying  $\hat{Q}_c > 0$ . Darker curves denote stronger net radiative heating rates in the convective region. Note that  $\alpha = 0.08$  in all cases. Solutions are plotted as a function of the  $l_d$ , the distance to the outer edge of the dry region. Top left: the convective fractional area,  $\sigma = l_c^2/l_d^2$ . Top right: the relative humidity in the convective region boundary layer,  $RH_c$ . Mid left: the length of the convective region,  $l_c$  (km). Mid right: the vertical velocity in the convective region free troposphere,  $w_c$  (m/s). Bottom left: the tropospheric difference in moist static energy,  $\Delta h_{trop}$ . Bottom right: the surface precipitation,  $P$  (mm/day).

*Comparison To Simulations.* The simple model solutions are now discussed in the context simulation results. It is important to acknowledge the deficiencies of the simple model before doing so. First, it is clear that the boundary between convection and dry, subsiding region in the simulations is not distinct as it is in the simple model. Capturing all of the effects of convection and various types of clouds on water, mass and energy budgets with a single three-layer column with prescribed radiation is a large simplification. On the other hand, capturing the effects of the dry region in a single column is more justified because there is little convection occurring in the dry region. We do not interpret the simple model solutions as being highly representative of the simulated aggregated RCE state because of the simple representation of the convective region in the simple model. However, we expect that the simple model solutions will pertain more closely to the block-averaged (mesoscale) simulation results because some of the spatial inhomogeneities are averaged out.

We now discuss the radiative cooling solution regime in the context of the simulation results. Recall that the convective region was radiatively cooling in the simulations, so that we do not attempt to compare the simulations to the radiative heating regime. We have seen that the spatial scale of the simple model is bounded below and unbounded above in this regime, but we have not discussed the physical validity of these solutions, beyond the agreement with the sign of the radiative heating rate in the convective region. Recall that these solutions have  $\Delta h_{trop,eff} > 0$ , and in particular,  $\Delta h_{trop} > 0$  for most  $l_d$  (see Figure 7.10, right). From the simulations, however, it is clear that  $\Delta h_{trop} < 0$ , (see Figure 7.16 and Table 7.3), which suggests that the solutions with  $\Delta h_{trop} > 0$  are inconsistent with the simulation results. Furthermore, the solutions with  $\Delta h_{trop} > 0$  correspond to a circulation that has negative *gross moist stability* (GMS), which is inconsistent with the sign of the

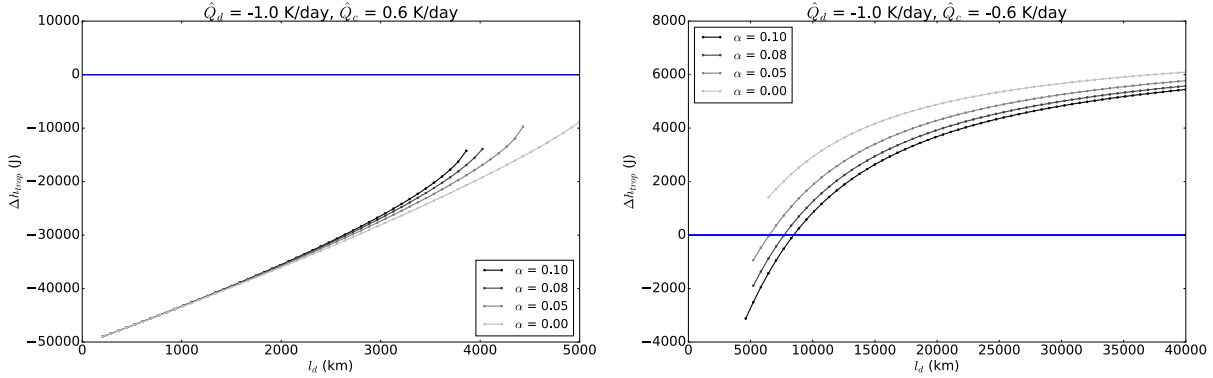


FIGURE 7.10. The tropospheric difference in moist static energy,  $\Delta h_{trop} = h_{BL} - h_{out}$  for the simple model radiative cooling regime solutions (left) and the radiative heating regime solutions (right).

GMS for the convective region in the simulations. The gross moist stability is a measure of the vertically-integrated transport of moist static energy (MSE) out a convectively active region (Neelin & Held, 1987). In the the simulations, we infer that the circulation *exports* MSE out of the convective region so the GMS is positive. We infer that the GMS is positive because there is net energy input into the convective region when considering all net sources and sinks of energy without accounting for the horizontal transport of energy (see Figure 7.11). Therefore, the convective region must export energy in order to maintain a state of energy balance. In the the simple model, however, the convective region can either export or import MSE from the convective region depending on the sign of  $\Delta h_{trop}$ . Previous studies of convective aggregation have found that the import of MSE into the convective region is important in the initiation of the aggregated state (Bretherton et al., 2005; Muller & Held, 2012; Wing & Emanuel, 2013), however during the mature stages of aggregation, the convective region was typically found to export MSE. Furthermore, a positive  $\Delta h_{trop}$  (and hence negative GMS) is largely inconsistent with observations of the tropical atmosphere (Riehl & Malkus, 1958; Neelin & Held, 1987). This suggests that the simple model should

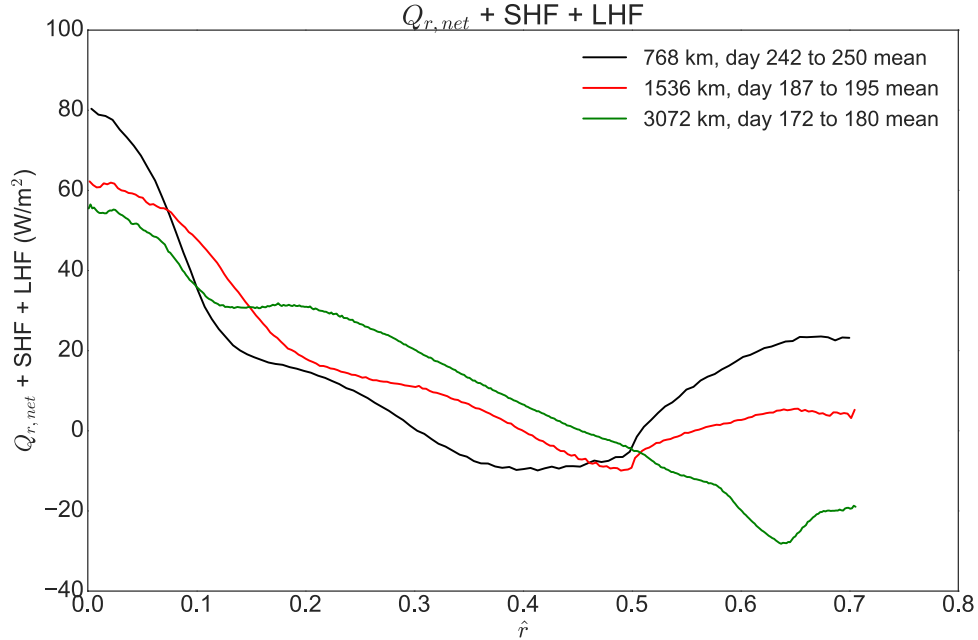


FIGURE 7.11. Radial profiles of the sum of net radiative heating, surface latent heat flux, and sensible heat flux  $Q_{r,net} + LHF + SHF$  ( $\text{W}/\text{m}^2$ ), respectively.  $Q_{r,net}$  is calculated by subtracting the net radiative fluxes at the top of the atmosphere with that at the surface. The x-axis is domain normalized radial distance,  $\hat{r}$ , as defined in the text. A positive value indicates net energy input into the atmospheric column at the indicated value of  $\hat{r}$ .

have positive GMS and hence  $\Delta h_{trop}$  should be negative, so that the solutions are consistent with the simulated aggregated state and the observations of tropical convection.

Not *all* radiative cooling regime solutions correspond to  $\Delta h_{trop} > 0$ , however. In particular, if  $\alpha \neq 0$ , there are solutions with  $\Delta h_{trop} < 0$  (see Figure 7.10, right). In other words, when  $\alpha$  is nonzero, there are solutions which are consistent with the sign of the radiative heating in the convective region, *and* the sign of the GMS from the simulations. This can be seen most clearly with the aid of (82):

$$\omega_c = \frac{g\hat{Q}_c + \alpha g L_v P}{\Delta h_{trop}} \quad (126)$$

Importantly, if  $\Delta h_{trop} < 0$  and  $\hat{Q}_c < 0$ ,  $\omega_c$  can be negative (upward motion) if the surface evaporation term ( $\alpha P$  term) is greater in magnitude than the net radiative cooling in the convective region.

The requirement that  $\Delta h_{trop} < 0$  introduces an additional constraint on  $RH_c$  in the radiative cooling regime, i.e., that  $RH_c$  cannot exceed  $RH_{c,0} = -\frac{\Delta s_{trop}}{L_v q_{sat}}$ . We define  $RH_{c,0}$  as the value of relative humidity in the convective region boundary that yields  $\Delta h_{trop} = 0$ . Note that in our simulations,  $RH_{c,0} \approx 87\%$ . Therefore, in order to have solutions which are consistent with the simulated aggregated state,  $RH_c$  must be in the range:

$$RH_{c,crit} < RH_c < RH_{c,0} \quad (127)$$

$$\frac{-\Delta s_{trop}}{L_v q_{sat} (1 + \frac{\alpha}{1-\alpha})} < RH_c < -\frac{\Delta s_{trop}}{L_v q_{sat}} \quad (128)$$

We refer to these solutions as *physical* solutions, as they are the most physically consistent with the simulation results and observations of the tropical atmosphere. The physical solutions are contrasted with the unphysical solutions (i.e. solutions with  $\Delta h_{trop} > 0$ ) in Figure 7.12). Importantly, from (128), we can see that there are no physical solutions in the radiative cooling regime if  $\alpha = 0$ . This makes sense from an energy balance perspective. If the convective region is constrained to export moist static energy (positive GMS), and the convective region is radiatively cooling, there must be an input of energy from the surface into the convective region in order to maintain a state of energy balance. In the simple model, the surface evaporation term provides the necessary energy input into the convective region. This is consistent with the simulation results as well (see Figure 7.13). Importantly, the latent heat flux provides energy input into the convective region, which exceeds the energy loss by radiative cooling. Note that although the sensible heat fluxes are not small in

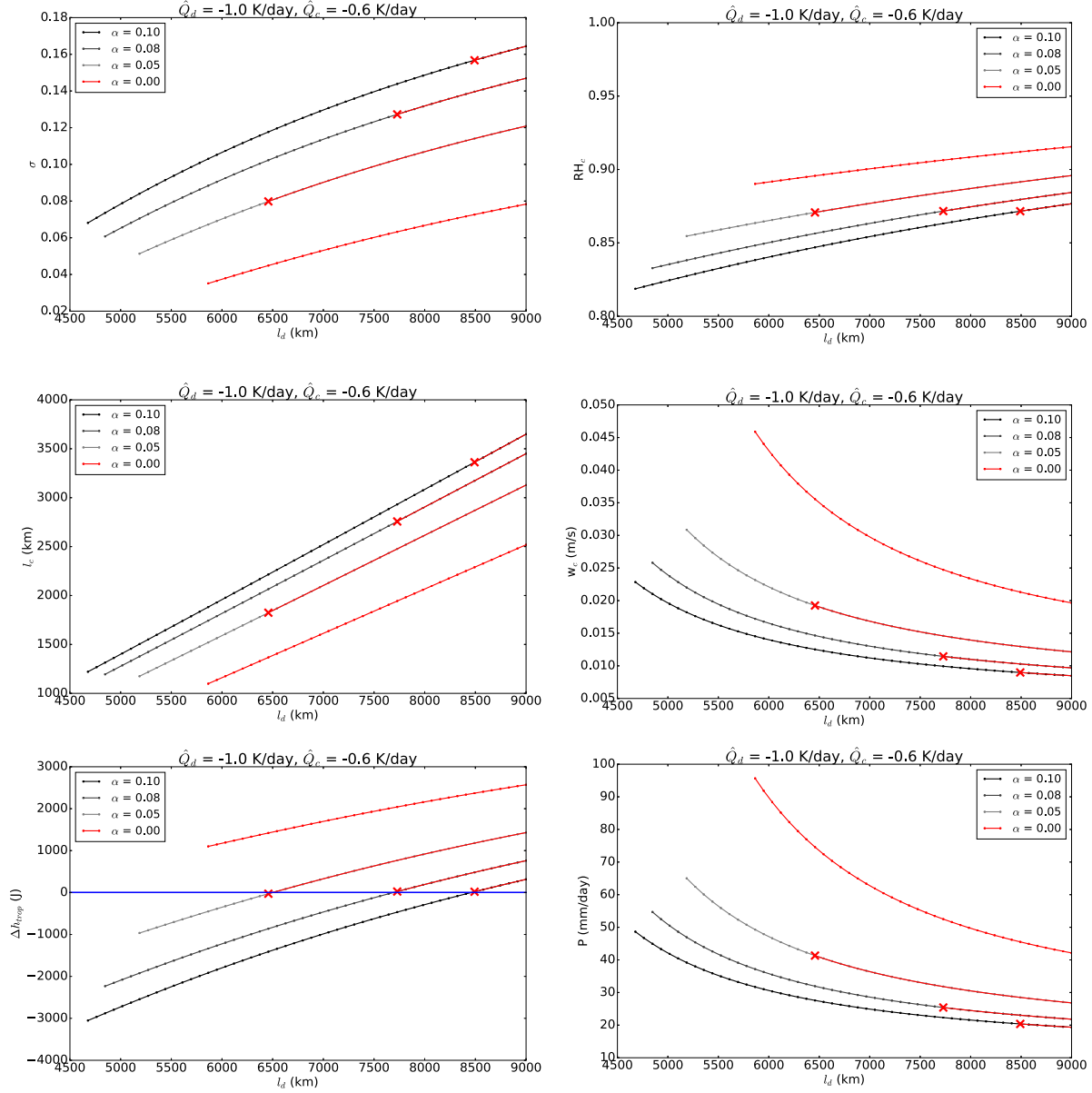


FIGURE 7.12. Solutions of the simple model of the aggregated RCE state for the radiative cooling regime. The solutions are the same as in Figure 7.5, except that physical solutions (i.e. solutions for  $\Delta h_{trop} < 0$ ) are contrasted with unphysical solutions ( $\Delta h_{trop} > 0$ ), by plotting in black and red, respectively. Darker curves denote larger values of  $\alpha$ . The X marker on each curve denotes the domain length at which  $\Delta h_{trop} = 0$  for a given value of  $\alpha$ , i.e., the upper bound on the spatial scale of the simple model. Top left: the convective fractional area,  $\sigma = l_c^2/l_d^2$ . Top right: the relative humidity in the convective region boundary layer,  $RH_c$ . Mid left: the length of the convective region,  $l_c$  (km). Mid right: the vertical velocity in the convective region free troposphere,  $w_c$  (m/s). Bottom left: the tropospheric difference in moist static energy,  $\Delta h_{trop}$ . Bottom right: the surface precipitation,  $P$  (mm/day).

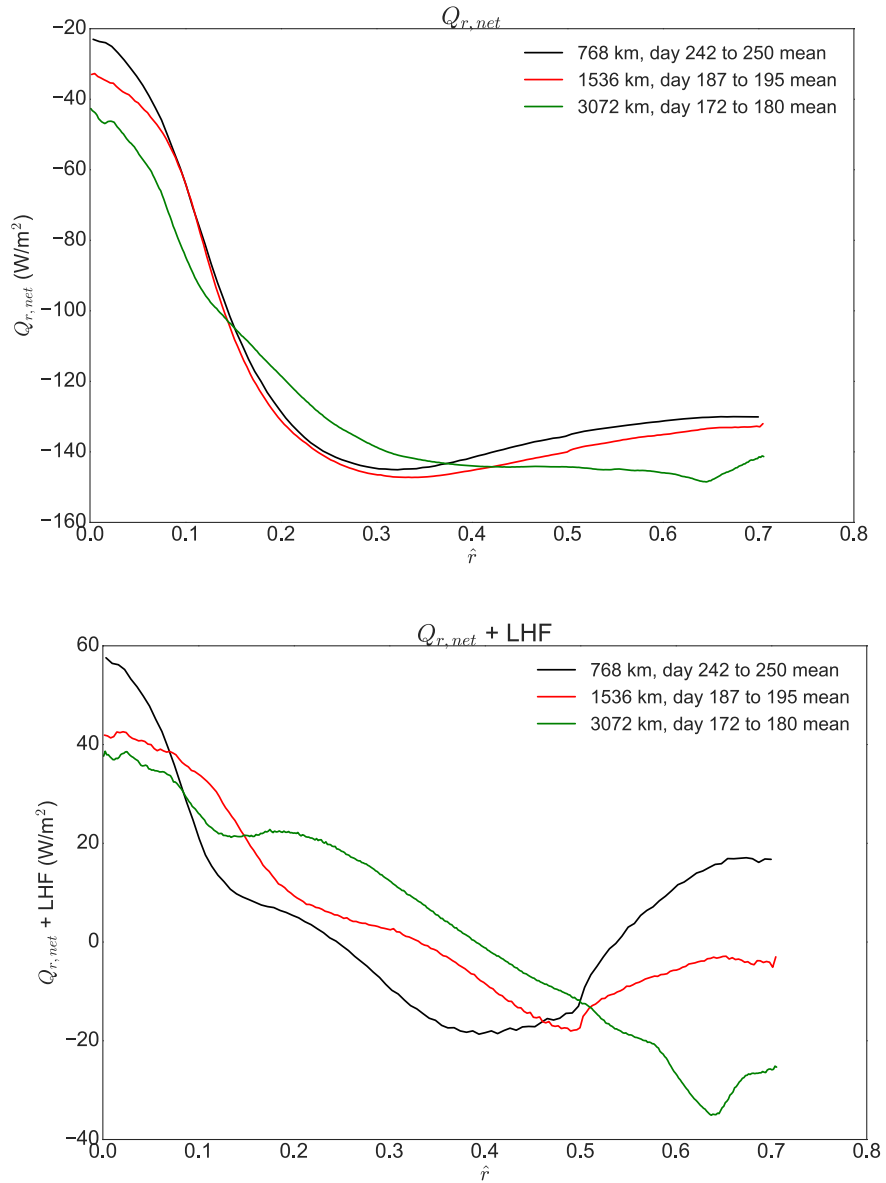


FIGURE 7.13. Radial profiles of the sum of net radiative heating and surface latent heat flux  $Q_{r,net} + LHF$  ( $W/m^2$ ), respectively.  $Q_{r,net}$  is calculated by subtracting the net radiative fluxes at the top of the atmosphere with that at the surface. The x-axis is domain normalized radial distance,  $\hat{r}$ , as defined in the text. A positive value indicates net energy input into the atmospheric column at the indicated value of  $\hat{r}$ .

the convective region (see 7.14), the sensible heat flux does not change the sign of the energy input into the convective region. In other words, the latent heat flux is the primary reason for the energy input into the convective region.

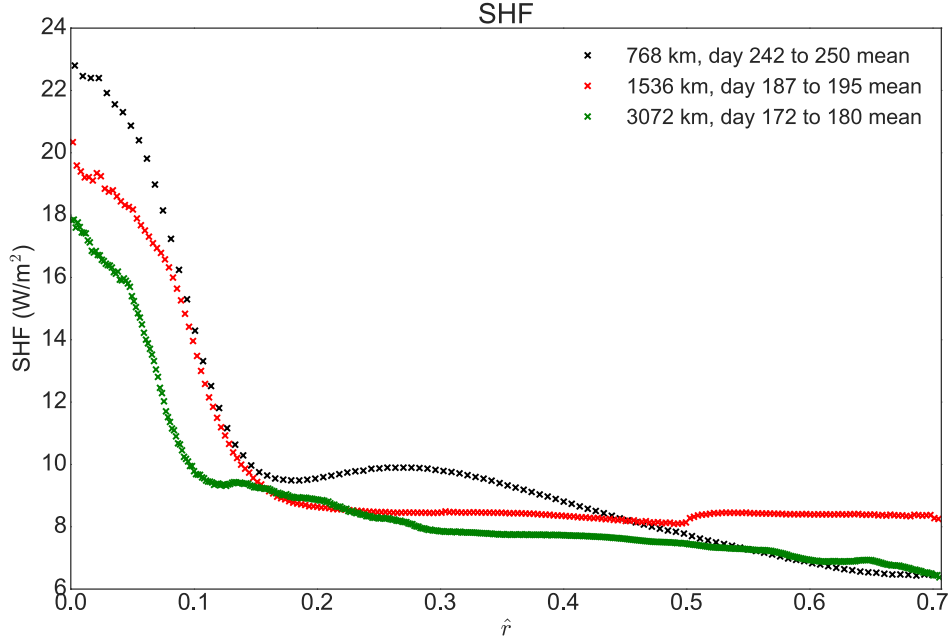


FIGURE 7.14. Radial profiles of the surface sensible heat flux,  $SHF$  ( $\text{W}/\text{m}^2$ ). The x-axis is domain normalized radial distance,  $\hat{r}$ , as defined in the text. A positive value indicates net energy input into the atmospheric column at the indicated value of  $\hat{r}$ .

This suggests that there is an additional physical constraint on the spatial scale of the simple model, which occurs at  $\Delta h_{trop} = 0$ . Therefore, in the radiative cooling regime, the spatial scale of the convective region is bounded below by  $\Delta h_{trop,eff} = 0$  and *physically constrained* above by  $\Delta h_{trop} = 0$ . In other words, the convective region could not expand indefinitely with increasing domain size because at some length scale  $\Delta h_{trop}$  would eventually become positive. Recall that the lower bound can be interpreted as the length scale at which the convective region boundary layer becomes too dry (i.e.  $\Delta h_{trop,eff} < 0$  and hence  $RH_c < RH_{c,crit}$ ), such that the precipitation and hence surface evaporation is too weak to balance the sum of the radiative and adiabatic cooling in the convective region free troposphere.

It is interesting that higher surface evaporation (higher  $\alpha$ ) tends to increase the gross moist stability at a  $l_d$  (i.e. decrease  $\Delta h_{trop}$ ; see Figure 7.12). This is because, as previously discussed, with higher  $\alpha$ , there is a larger addition of water vapor directly into the free troposphere due to turbulent fluxes of water vapor from the convective region boundary layer, so that convection can persist with lower relative humidity in the convective region boundary layer. In other words, with higher  $\alpha$ , the source of the convection is the surface evaporation, rather than the pre-existing humidity in the convective region boundary layer. Importantly, we can see that the higher surface evaporation also increases the upper bound for the spatial scale of the simple model (see Figure 7.12). In other words,  $RH_c$  reaches  $RH_{c,0}$  at a larger domain size when  $\alpha$  is higher. This is because, at a given  $l_d$ ,  $RH_c$  will be lower when  $\alpha$  is higher, which means the boundary layer fetch will be lower when  $\alpha$  is higher (see Figure 7.15). Therefore,  $RH_c$  will reach  $RH_{c,0}$  at a larger  $l_d$ , and hence the upper bound for the spatial scale of the simple model will increase. We can also see that the lower bound of the spatial scale of the simple model decreases with increasing  $\alpha$ . This is because, as previously discussed, convection can be sustained with less relative humidity in the convection region boundary layer when  $\alpha$  is higher. Therefore  $RH_{c,crit}$  decreases with increasing  $\alpha$  (see Figure 7.3), and hence  $RH_c$  will approach  $RH_{c,crit}$  at a lower  $l_d$ .

It is also interesting that the lower bound for the spatial scale of the simple model is around 5000 km, while we have seen that a convective region can in fact exist in the domain at domain lengths less than 5000 km in our simulation results. We suspect that this inconsistency is primarily due to the fact that the simple model boundary layer requires unrealistically high fetch in order to become sufficiently humid. As previously discussed, the boundary layer is unrealistically dry because the free troposphere has very low water

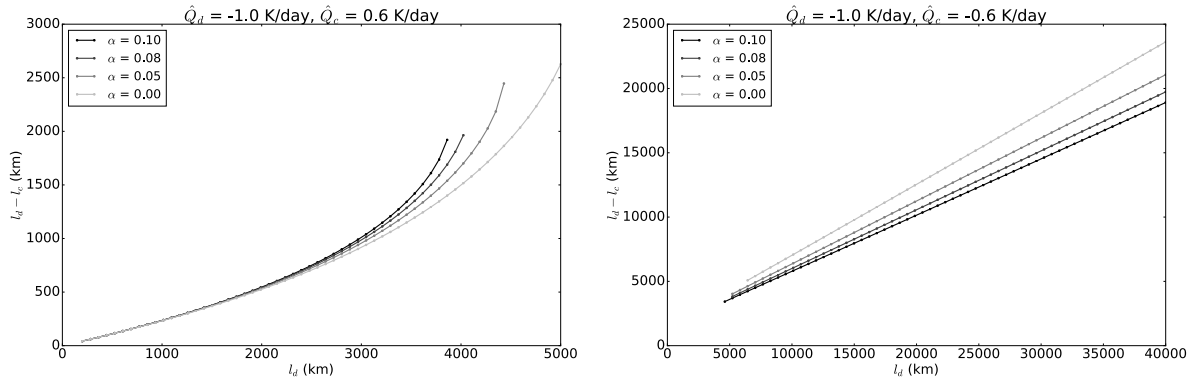


FIGURE 7.15. The dry region boundary layer fetch,  $l_d - l_c$  for the simple model radiative heating regime solutions (left) and the radiative cooling regime solutions (right), for varying  $\alpha$ .

vapor content, given by the water vapor mixing ratio at the outflow layer height, and hence the subsidence drying is unrealistically high. In the simulations, we have seen that there is moisture transport from the convective region into the dry region immediately above the boundary layer, which acts as a moisture supply into the dry region boundary layer. We suspect that the addition of a layer above the boundary layer in the simple model would prevent the boundary layer from becoming too dry, and hence decrease the fetch required for a humid boundary layer. This would tend to decrease the lower bound on the spatial scale of the aggregated RCE state in the simple model, and as a result, we might see more agreement with the spatial scale of the convective region in the simulations.

We now compare the sensitivity of the the simple model to domain size to that of the simulations. Recall that  $\Delta h_{trop}$  increased with increasing  $l_d$  in the simple model. We also found that  $\Delta h_{trop}$  increased with increasing domain size in the simulations (see Table 7.3). An interesting point is that while the increase in  $\Delta h_{trop}$  in the simple model solutions is due to increasing water vapor in the convective region boundary layer, the increase in  $\Delta h_{trop}$  in the simulations is likely due to an increase in water vapor *and* temperature in the convective region boundary layer (see Table 7.3). Another important point is that in the simulations,

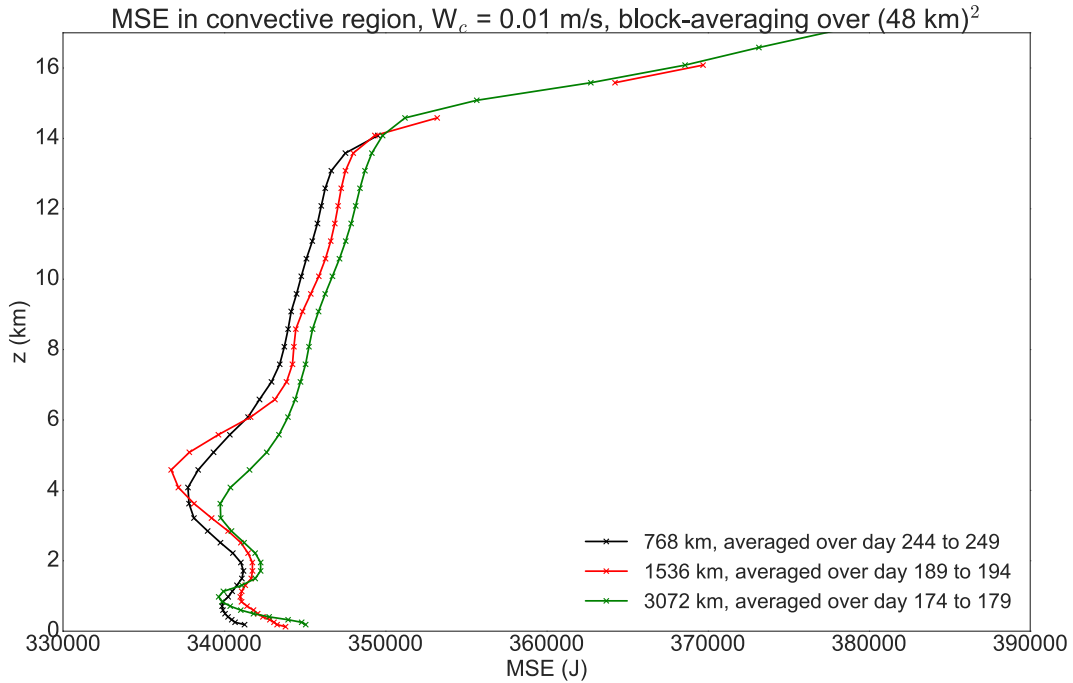


FIGURE 7.16. Vertical profiles of the moist static energy, MSE (J), for the small (black), medium (red), and large (green) domain simulation runs. The MSE profiles are averaged over the last 5 days of the simulation.

the increase in water vapor and temperature in the lower levels leads to deeper convection, which means the MSE at the tropopause is higher, and hence this partially offsets the increase  $\Delta h_{trop}$  due to the increase in MSE in the boundary layer. Evidently, however, the increase in MSE aloft due to the deeper convection is not exactly equal to the increase in MSE in the boundary layer, so that  $\Delta h_{trop}$  still increased with domain size. Recall that we have shown that the horizontal temperature anomaly in the convective region boundary layer is increasing with domain size (see Figure 4.17), and that this has effects on the convective region and surrounding dry region which ultimately favor additional convection in the remote environment. This suggests that the domain length is approaching the natural spatial scale of the aggregated RCE state. It is interesting that both the simple model and the simulations suggest that the upper bound on spatial scale of the convective region is approached with

increasing  $\Delta h_{trop}$ . This suggests that the natural spatial scale of the aggregated RCE state is the scale at which  $\Delta h_{trop}$  in the convective region becomes close to zero.

TABLE 7.4. Dry and Moist Static Energy in Simulated Convective Region

| Domain Width | $s_{BL}$<br>( $10^5$ J) | $s_{out}$<br>( $10^5$ J) | $h_{BL}$<br>( $10^5$ J) | $h_{out}$<br>( $10^5$ J) | $\Delta s_{trop}$<br>( $10^4$ J) | $\Delta q_{v,trop}$<br>(kg/kg) | $\Delta h_{trop}$<br>(J) | $\Delta h_{trop,eff}$<br>(J) |
|--------------|-------------------------|--------------------------|-------------------------|--------------------------|----------------------------------|--------------------------------|--------------------------|------------------------------|
| 768 km       | 3.020                   | 3.474                    | 3.405                   | 3.475                    | -4.549                           | 0.0170                         | -6979                    | -4960                        |
| 1536 km      | 3.023                   | 3.492                    | 3.429                   | 3.493                    | -4.698                           | 0.0177                         | -6432                    | -2956                        |
| 3072 km      | 3.026                   | 3.498                    | 3.437                   | 3.498                    | -4.717                           | 0.0180                         | -6138                    | -600                         |

Finally, recall that the dependence of  $\sigma$  on  $l_d$  depends on whether radiative heating or radiative cooling is prescribed in the convective region. In particular,  $\sigma$  decreased with  $l_d$  in the radiative heating regime, but increased with  $l_d$  in the radiative cooling regime (see Figure 7.17, top left). Recall that, in the simulations, the mesoscale convective fractional area, i.e.  $\sigma_m$ , increased with domain size. Thus, the convective fractional area dependency on domain size in the simulations was captured by the simple model radiative cooling regime solutions. Additionally, the dependence of precipitation and vertical velocity on domain size were also captured by these simple model solutions. In particular, note that the both the precipitation and the vertical velocity decrease with  $l_d$  in the radiative cooling regimes (see 7.17, middle and bottom right), which is consistent with the weaker mesoscale convective updraft and lower surface precipitation that occurred with increasing domain size in the simulations.

It is important to note that  $\Delta h_{trop,eff} > 0$  in the radiative cooling regime, so that we cannot simply use (144) to diagnose the simulation results because  $\Delta h_{trop,eff}$  was diagnosed to be negative in the simulations (see Table 7.3). This would seem to suggest that there would be a net energy unbalance between the energy loss due to radiative cooling ( $\hat{Q}_c$ ), horizontal

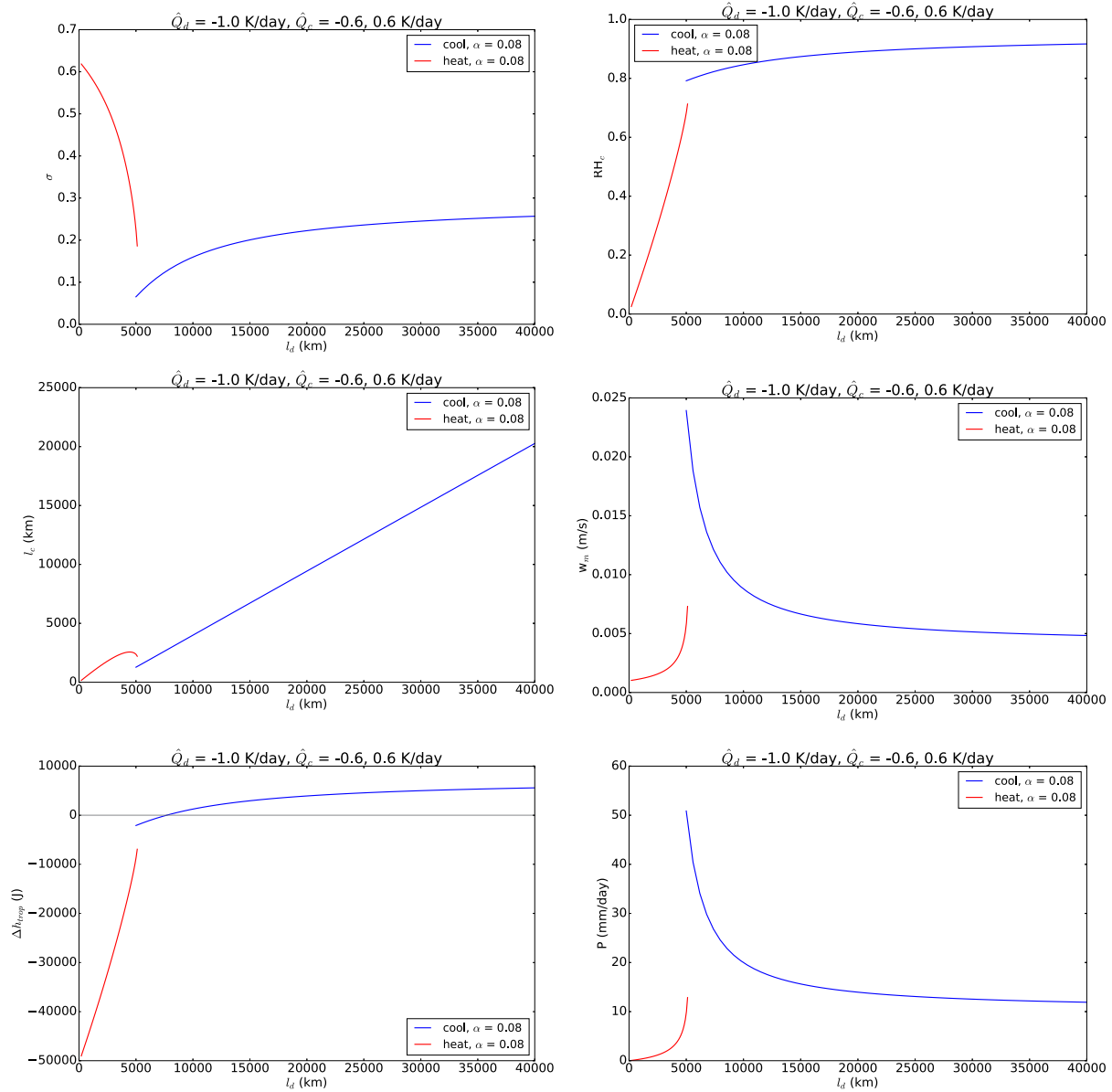


FIGURE 7.17. Solutions of the simple model of the aggregated RCE state for  $\hat{Q}_d = -1.0$  K/day,  $\hat{Q}_c = 0.6$  K/day (red) and  $\hat{Q}_c = -0.6$  K/day (blue). Solutions are plotted as a function of the  $l_d$ , the distance to the outer edge of the dry region. Note that we use  $\alpha = 0.08$  to compute the solutions in this case. Top left: the convective fractional area,  $\sigma = l_c^2/l_d^2$ . Top right: the relative humidity in the convective region boundary layer,  $RH_c$ . Mid left: the length of the convective region,  $l_c$  (km). Mid right: the vertical velocity in the convective region free troposphere,  $w_c$  (m/s). Bottom left: the effective tropospheric difference in moist static energy (defined in text),  $\Delta h_{trop,eff}$ . Bottom right: the surface precipitation,  $P$  (mm/day).

transport of energy ( $\Delta h_{trop}$ ), and energy input by surface evaporation ( $\alpha P$ ). However, it is important to note that the horizontal transport of energy in the simulations is not simply proportional to  $\Delta h_{trop}$  because the convective region has more complex vertical structure as compared to the simple model. As we have previously seen that the latent heat flux in the convective region exceeds the radiative cooling in the convective region, we suspect that there is additional energy input into the convective region at different levels in the vertical. In other words, the horizontal export of energy from the convective region may not be as large as  $\Delta h_{trop}$  would lead us to believe.

*Summary.* In summary, in the simple model, the fraction of the domain occupied by the convective region is primarily influenced by the relative heating rates between the convective region and dry region along with the tropospheric difference in effective moist static energy,  $\Delta h_{trop,eff}$ . The solutions that had radiative cooling and surface evaporation (non-zero  $\alpha$ ) in the convective region were most physically consistent with the simulation results. Specifically, these solutions captured the broadening of the convective region, the weakening of the convective region updraft, as well as the negative and increasing moist static tropospheric energy difference,  $\Delta h_{trop}$ , (i.e. positive gross moist stability), that occurred with increasing domain size in the simulations. The broadening of the convective region in the simple model with increasing domain size was due to an increase in the convective region boundary layer humidity with increasing domain size. Since the rate of energy loss by the convective region free troposphere was invariant with domain size (i.e. the radiative cooling rate is invariant) and the increase in boundary layer humidity resulted in an increase in the supply of energy available for transport into the convective region free troposphere, the vertical velocity decreased in order to conserve energy. Together with the invariant subsidence in the dry region,

the decrease in vertical velocity resulted in an increase of the convective fractional area with increasing domain size, by mass conservation. For  $0 < \alpha < 0.1$ , the spatial scale of these solutions was constrained to be in the range of  $5000 < l_d < 9000$  km. The upper bound on the spatial scale was given by the length scale at which the convective region boundary layer became sufficiently humid, such that  $\Delta h_{trop}$  became positive (i.e. negative gross moist stability). The lower bound on the spatial scale was given by the length scale at which the boundary layer became too dry, such that the precipitation and hence surface evaporation was too weak to balance the sum of the radiative and adiabatic cooling in the convective region free troposphere. The range of the bounds on the spatial scale of the simple model was sensitive to  $\alpha$ , such that higher values of  $\alpha$  increased (decreased) the upper (lower) bound, because convection could be sustained at larger (smaller)  $l_d$  with lower relative humidity in the convective region boundary layer when the surface evaporation in the convective region was higher. The lower bound of approximately 5000 km is likely quite high because the boundary layer requires unrealistically high fetch in order to become sufficiently humid. Importantly, recall that we showed that multiple convective clusters were more likely the form in the domain when the domain size was larger in the simulations. Therefore, overall, the simulation results together with the simple model results suggest that the processes which influence the humidity in the convective region boundary layer and hence the gross moist stability ( $\Delta h_{trop}$ ), such as the surface evaporation, are important for determining the natural spatial scale of the aggregated RCE state.

It is important to note that the processes which determine  $\Delta h_{trop}$  are complicated. In the simulations, it is likely that  $\Delta h_{trop}$  is controlled by many complex processes, such as cold pool induced low-level moisture and temperature perturbations in the convective region, for

example. It is even a challenge to understand  $\Delta h_{trop}$  in our simple model, where  $\Delta h_{trop}$  is determined completely by  $RH_c$ , because  $RH_c$  depends nonlinearly on both  $l_d$  and  $l_c$ . This means that we cannot simply solve for  $RH_c$  in terms of  $l_d$ . Importantly, however, we have seen that all solutions correspond to the convective region boundary layer getting more humid with increasing  $l_d$ . This is essentially because the boundary layer fetch *always* increases with increasing  $l_d$  (see Figures 7.15), so that parcels of air are more wet by the time they reach the convective region edge. In the simulations, we suspect that it is likely that increased boundary layer fetch with increasing domain size also contributes to increasing  $\Delta h_{trop}$ , which may eventually contribute to  $\Delta h_{trop}$  approaching zero and perhaps an upper bound to the convective region. We leave further investigation of the processes which control  $RH_c$  and hence  $\Delta h_{trop}$  in the simulations to future work. Understanding the processes that contribute to increasing  $\Delta h_{trop}$  with increasing domain size in both simulations and simple models of convective aggregation, may prove to be enlightening in terms of understanding the natural spatial scale of the aggregated RCE state.

Finally, recall that our formulation of the convective region in the simple model neglected many important aspects of convection, including convective heat fluxes and multiple cloud types. These aspects could prove to be important in a simple model of the aggregated RCE state, so, in the end, we interpret the results of the simple model in the context of the cloud-resolving simulations with caution.

## 8. CONCLUSIONS & FUTURE DIRECTION

### 8.1. COMPARING THE SIMPLE MODEL TO THE SIMULATIONS

8.1.1. *Spatial Scale of Aggregated RCE.* The solutions of the simple model of the aggregated RCE state that had net radiative cooling and surface evaporation in the convective region were consistent with the simulation results. In particular, these solutions captured the broadening of the convective region, the weakening of the convective region updraft, as well as the negative and increasing moist static tropospheric energy difference,  $\Delta h_{trop}$ , that occurred with increasing domain size in the simulations. Recall that the increase in  $\Delta h_{trop}$  in the simulation was due to both increasing temperature and humidity, while the increase in  $\Delta h_{trop}$  was purely due to an increase in humidity. The broadening of the convective region in the simple model with increasing domain size was due to an increase in the convective region boundary layer humidity with increasing domain size. Since the rate of energy loss by the convective region free troposphere was invariant with domain size and the increase in boundary layer humidity resulted in an increase in the supply of energy available for transport into the convective region free troposphere, the vertical velocity decreased in order to conserve energy. Together with the invariant subsidence in the dry region, the decrease in vertical velocity resulted in an increase of the convective fractional area with increasing domain size, by mass conservation. It is interesting that the convective region broadens with domain size in both the simulations and the simple model, and that this is associated with an increase in  $\Delta h_{trop}$ . This suggests that the mesoscale convective fractional area in the cloud-resolving simulations depends on  $\Delta h_{trop}$  in an important way.

The simple model shows that there is a length scale at which  $\Delta h_{trop}$  will become positive, which would likely limit the spatial scale of the convective region in the simulations because

a convective region with  $\Delta h_{trop} > 0$  (negative GMS) is inconsistent with the simulated aggregated state, and also inconsistent with observations of convectively-active regions such as the rising branch of the Hadley Cell. Therefore, we conclude that the convective region would not expand indefinitely in the simulations because eventually  $\Delta h_{trop}$  would “want” to become positive with increasing domain size, but would be physically constrained because convection cannot be sustained with negative gross moist stability. While  $\Delta h_{trop}$  increased with domain size in the simulations, it is not clear how large the domain size needs to be in order to reach such a state. Recall that we have seen a tendency for an additional convective cluster to form in the domain in the large domain case (3072 x 3072 km), which suggests that we are approaching a domain size at which multiple convective cluster can co-exist in the domain. For a radiative heating rate that is equal to the magnitude of the vertically averaged radiative cooling in the convective region (-0.6 K/day) and  $\alpha = 0.08$ , the simple model suggests that the natural spatial scale of the aggregated RCE state is around 7000 km. As the largest radial distance on a periodic square domain of width  $L$  is  $\frac{L}{\sqrt{2}}$ , in order to accommodate two convective clusters, the domain size would require side length roughly equal to  $2\sqrt{2}(7000)$  km  $\approx 20,000$  km. Of course, this is only an estimate of the spatial scale based on the simple model, which is sensitive to prescribed parameters such as the radiative cooling rate in the convective region, and should be interpreted with caution. In a GCM study of RCE by Silvers et al. (2016), the mean RCE state was found to converge at domain width of around 3000 to 5000 km, and similarly, and a single convective cluster has been shown to appear around a domain width of about 5000 km in the Goddard Earth Observing System Model, Version 5 (GEOS-5) when the domain width is steadily decreased

starting from around 20,000 km (Arnold, 2016). In any case, this motivates CRM simulations with a domain width larger than 3072 km as used in this study.

Finally, we note that in previous studies of convective aggregation, the area of the convective cluster has been shown to scale at about 20% the domain size (Muller & Held, 2012), however, our simple model suggests that this value is not particularly unique. If the radiative heating rates were different, for example, the exact size scaling percentage would be different as well. Furthermore, both the simple model and simulations suggest that the convective fractional area actually *increases* with domain size. It seems likely that mass, water, and energy can be balanced in a variety of ways and the size scaling that we observe in the aggregated RCE state is simply due to the relative heating rates of the dry region and convective region, as well as the tropospheric moist static energy difference.

8.1.2. *Vertical Structure.* It is important to note that a complication in comparing our simple model to the simulation results is that the vertical structure is much more complex in the simulations as compared to the simple model. For example, it is likely that a single prescribed vertically averaged heating rate for the convective region is a large simplification, as the structure of heating in the convective region is far from vertically uniform. This motivates incorporating a more complicated vertical structure into the simple model. Allowing a vertically varying radiative heating rate in the convective region may yield solutions that are more representative of the simulation results. It would be interesting to see how such a vertically varying radiative heating rate would affect the solutions as we have seen that the simple model solutions interestingly divide into two separate regimes that depend on the sign of the convective region heating rate. The vertically varying radiative heating rate

would also be associated with vertically varying velocity in the convective region, which is much more consistent with the simulation results.

Also recall that our simple model has a highly simplified formulation of convection that disregards multiple cloud types, which may detrain at different levels and transport moisture into the dry region. We have seen that the cloud population consists of shallow cumuli, mid-level cumulus congestus and deep convective clouds in the aggregated state, which also have important sensitivities to domain size. For example, the mid-level cumulus activity increases with domain size, whereas the detrainment of clouds immediately above the boundary layer decreases with domain size. The detrainment of mass and moisture at different levels has important effects on the aggregated state, which could prove to be important in a simple model of the aggregated state. For example, if less moisture and mass is detrained immediately above the boundary layer, this is likely associated with less subsidence drying into the boundary layer (as we have seen in the simulations), which may lead to a different radial profile of relative humidity in the dry region boundary layer, and hence a different natural spatial scale for the aggregated state (i.e.  $RH_{c,crit}$  is reached at a different  $l_d$ ). This further motivates the need to introduce more vertical structure to the simple model. In particular, introducing a shallow outflow layer above the boundary layer may be useful in modeling the transport of moisture from the convective region into the dry region.

8.1.3. *Understanding  $\Delta h_{trop}$ .* Our simple model suggests that understanding the processes that determine the tropospheric moist static energy difference in the convective region boundary layer,  $\Delta h_{trop}$ , in more detail may help us understand what determines the natural spatial scale of convective aggregation. In particular, the simple model suggest that understanding the processes that control the relative humidity in the convective region boundary

layer,  $RH_c$ , are key to understanding the spatial scale of the aggregated state. Recall that we showed that the boundary layer fetch increased with increasing domain size in the simple model, so that  $RH_c$  and hence  $\Delta h_{trop}$  increased with domain size. This is ultimately why  $\Delta h_{trop}$  became positive and hence why the spatial scale of the convective region was physically constrained. It is reasonable to believe that increasing boundary layer fetch also contributes to the observed increase in  $\Delta h_{trop}$  with domain size in the simulations. However, understanding the processes that determine exactly how  $\Delta h_{trop}$  varies with domain size is a challenge even in the simple model, because  $RH_c$  is a function of the size of the convective region itself,  $l_c$ . It is important to note that  $RH_c$  is likely under constrained in our simple model, as deep convection is possible with any boundary layer relative humidity in our formulation of the convective region. In reality, deep convection typically only occurs when the boundary layer is sufficiently humid. However, this work suggests that simply prescribing a value of relative humidity in the convective region boundary layer would constrain the convective region in a way that is not consistent with the simulations (as it is clear that  $RH_c$  along with  $\Delta h_{trop}$  are increasing with domain size). Introducing additionally complexity to  $RH_c$  may be an important next step in understanding the processes that control how  $RH_c$  varies with  $l_d$ . For example, it may be sufficient to constrain  $RH_c$  to be greater than 0.75, but then leave  $RH_c$  free to vary radially, so that the radial profile of  $RH_c$  can still vary with  $l_d$ . This would be more consistent with what is observed in our simulations.

Additionally, recall that  $\Delta h_{trop}$  varied with the the turbulent fluxes of water vapor into the convective region free troposphere,  $\alpha$ . In particular, with higher  $\alpha$ ,  $\Delta h_{trop}$  became more negative. In other words, the gross moist stability was larger for higher  $\alpha$ . This is because, with higher  $\alpha$ , there is a larger addition of water vapor directly into the free troposphere

due to turbulent fluxes of water vapor from the convective region boundary layer, so that convection can persist with lower relative humidity in the convective region boundary layer. Additionally, that the range of the bounds of the spatial scale of the simple model increased when  $\alpha$  was higher. In particular, with higher  $\alpha$ , the upper bound for the spatial scale increased. The importance of  $\alpha$  in yielding physical simple model solutions, along with the effect of  $\alpha$  on the spatial scale motivates future cloud-resolving model studies of the turbulent fluxes in the convective region boundary layer, and in particular, how they contribute to moistening of the convective region free troposphere.

8.1.4. *Sensitivity to SST.* It would also be interesting to investigate the sensitivity of the simple model to the prescribed SST. Various studies have shown that convective aggregation does not occur when SSTs are low (e.g. Khairoutdinov & Emanuel, 2010; Wing & Emanuel, 2013), however, it has been shown that convective aggregation can occur in a CRM with long-channel geometry with low SSTs (Wing & Cronin, 2015). In particular, it has been shown that the length scale of the convective region *increases* with decreasing SST, suggesting that the small domains are just too small to support the aggregated RCE state when SSTs are low. In other words, the study by Wing & Cronin implies that the natural spatial scale of the aggregated RCE state decreases with increasing SST. Interestingly, this seems to be supported by our simple model. In particular, if the SST is higher, the relative humidity in the convective region boundary layer would be expected to be higher, and hence we might expect that  $RH_c$  would approach  $RH_{c,0}$  at a lower  $l_d$ . In other words, when the SST is high, less boundary layer fetch required in order to reach high relative humidity and hence for  $\Delta h_{trop}$  to approach zero. It is important to note that changes in SST have other important effects on the aggregated RCE state as well. For example, the subsidence in the dry region is

expected to decrease with increasing SST because the static stability is expected to increase with increasing SST. This would tend to increase spatial scale of the aggregated RCE state because, in order to balance mass, a larger subsiding area would be required with weaker subsidence. The competing effects of the SST on the aggregated RCE state highlights the importance of testing the sensitivity of the simple model to SST.

Before introducing additional complexity into the simple model, however, it would be desirable to diagnose all of the assumed relationships used in the simple model. The simulation results showed that the balance between adiabatic warming and radiative cooling in the dry region was a justifiable assumption in the simple model dry region, however, it is not clear that the assumption that adiabatic cooling balances the sum of condensation warming and radiative cooling in the convective region is valid. Properly diagnosing the simulation results with the simple model could inform future work in terms of how additional complexity should be introduced. For example, it is likely that we cannot simply disregard convective heat fluxes in the convective region.

## 8.2. COMPARISON TO GCMs

One motivation for this work is to bridge the gap between larger scale idealized GCM studies of RCE, and the smaller scale CRM studies of RCE. We have not presented any results in the context of GCM simulations, however, this work can serve as as one piece of a comparison study. In particular, it would be interesting to compare the CRM domain size sensitivities of the aggregated RCE state to that of a GCM. We have shown that the aggregated state in a CRM has interesting sensitivities to domain size, such as enhanced mid-level cumulus congestus detrainment, as a result of an enhancement of deeper convection and

an enhancement of the mid-level stable layer. This is also associated with important effects, such as general broadening of the convective region. These sensitivities suggest that large-scale interactions between deep convection and its environment can have important effects on the convective region itself. It would be interesting to determine whether such domain-size dependent feedbacks exist in a GCM with parameterized convection.

### 8.3. OSCILLATION OF AGGREGATED RCE

Finally, recall that, in our simulations, the aggregated RCE state had a long time period oscillation ( $\sim 25$  to  $30$  day), along with a short time period oscillation ( $< 1$  day). The short time period oscillation is consistent with findings from Naegel (2016), and is thought to be the combined effect of gravity-wave propagation and a “recharge-discharge” mechanism by convectively-generated cold pools. Our simulations support the recharge-discharge mechanism because the short time period oscillation seems to be insensitive to domain size. The gravity wave mechanism would show a sensitivity to domain size because gravity waves require a longer period of time to travel the entire length of the domain when the domain size is larger. The long time period oscillation was associated with a broadening and contracting of the convective region (see Supplementary Materials 3 and 4; animations of the cloud top height, precipitation and precipitable water for the large domain case). The mechanism responsible for the long time period oscillation is unknown and will be investigated in future work.

## 9. REFERENCES

Arnold, N. P., and D. A. Randall (2015), Global-scale convective aggregation: Implications for the Madden-Julian Oscillation, *J. Adv. Model. Earth Syst.*, 7, doi:10.1002/2015MS000498.

Arnold, N. P. (2016), Statistics and Mechanisms of Convective Organization in a 12 km Downscaled Global Reanalysis, Abstract A53E-06 presented at 2016 Fall Meeting, AGU, San Francisco, Calif., 12-16 Dec.

Bony, S., B. Stevens, D. Coppin, T. Becker, K. A. Reed, A. Voigt, and B. Medeiros (2016), Thermodynamic control of anvil-cloud amount, *Proc. Natl. Acad. Sci.*, 119 (32), 8927-8932, doi:10.1073/pnas.1601472113.

Bretherton, C. S., P. N. Blossey, and M. Khairoutdinov (2005), An energy-balance analysis of deep convective convective aggregation above uniform SST, *J. Atmos. Sci.*, 62, 4273-4292.

Bretherton, C. S., and M. F. Khairoutdinov (2015), Convective self-aggregation feedbacks in near- global cloud-resolving simulations of an aquaplanet, *J. Adv. Model. Earth Syst.*, 07, doi:10.1002/2015MS000499.

Chavas, D. R. (2013), Tropical cyclone size in observations and in radiative-convective equilibrium, PhD thesis, Mass. Inst. of Technol., Cambridge, Mass.

Chikira, M. (2014), Eastward-propagating intraseasonal oscillation represented by Chikira-Sugiyama cumulus parameterization. Part II: Understanding moisture variation under weak temperature gradient balance. *J. Atmos. Sci.*, 71, 615-639, doi:10.1175/JAS-D-13-038.1.

Coppin, D., and S. Bony (2015), Physical mechanisms controlling the initiation of convective aggregation in a General Circulation Model, *J. Adv. Model. Earth Syst.*, 7, 2060-2078, doi:10.1002/2015MS000571.

Cotton, W. R., et al. (2003), RAMS 2001: Current status and future directions, *Meteorol. Atmos. Phys.*, 82, 5-29.

Craig, G. C., and J. M. Mack (2013), A coarsening model for self-organization of tropical convection, *J. Geophys. Res. Atmos.*, 118, 8761-8769, doi:10.1002/jgrd.50674.

Davis, C. A. (2015), The formation of moist vortices and tropical cyclones in idealized simulations. *J. Atmos. Sci.*, 72(9), 3499-3516.

Emanuel, K. A. (1986), An air-sea interaction theory for tropical cyclones. Part I: Steady-state maintenance. *J. Atmos. Sci.*, 43, 585605.

Emanuel, K., A. A. Wing, and E. M. Vincent (2014), Radiative-convective instability, *J. Adv. Model. Earth Syst.*, 6, 75-90, doi:10.1002/2013MS000270.

Gill, A. E., (1980), Some simple solutions for heat induced tropical circulation. *Quart. J. Roy. Meteor. Soc.*, 106, 447462.

Grabowski, W. W. (2000), Cloud microphysics and the tropical climate: Cloud-resolving model perspective. *J. Climate*, 13, 23062322.

Grabowski, W. W. (2003), MJO-like coherent structures: Sensitivity simulations using the Cloud-Resolving Convection Parameterization (CRCP). *J. Atmos. Sci.*, 58, 978-997.

Grabowski, W. W. and M. W. Moncrieff (2004), Moisture-convection feedback in the tropics. *Quart. J. Roy. Meteor. Soc.*, 130, 30813104, doi: 10.1256/qj.03.135.

Hartmann, D. L., and K. Larson (2002), An important constraint on tropical cloud-climate feedback, *Geophys. Res. Lett.*, 29(20), 1951, doi:10.1029/2002GL015835.

Held, I. M., R. S. Hemler, and V. Ramaswamy (1993), Radiative-convective equilibrium with explicit two-dimensional moist convection, *J. Atmos. Sci.*, 50(23), 3909-3927.

Hohenegger, C., and B. Stevens (2016), Coupled radiative convective equilibrium simulations with explicit and parameterized convection, *J. Adv. Model. Earth Syst.*, 8,

doi:10.1002/ 2016MS000666.

Houze, R., Jr. (2004), Mesoscale convective systems, *Rev. Geophys.*, 42, RG4003, doi:10.1029/2004RG000150.

Holloway, C. E., and S. J. Woolnough (2016), The sensitivity of convective aggregation to diabatic processes in idealized radiative-convective equilibrium simulations, *J. Adv. Model. Earth Syst.*, 8, doi:10.1002/2015MS000511.

Jeevanjee, N., and D. M. Romps (2013), Convective convective aggregation, cold pools, and domain size, *Geophys. Res. Lett.*, 40, 994-998, doi:10.1002/grl.50204.

Johnson, R. H., P. E. Ciesielski, and K. A. Hart (1996), Tropical inversions near the 0 C level. *J. Atmos. Sci.*, 53, 1838-1855.

Johnson, R. H., T. M. Rickenbach, S. A. Rutledge, P. E. Ciesielski, and W. H. Schubert (1999), Trimodal characteristics of tropical convection, *J. Clim.*, 12, 2397-2418.

Khairoutdinov, M., and K. Emanuel (2010), Aggregation of convection and the regulation of climate. preprints, in 29th Conference on Hurricanes and Tropical Meteorology, pp. P2.69, Am. Meteorol. Soc., Tucson, Ariz.

Khairoutdinov, M. F., and K. A. Emanuel (2013), Rotating radiative-convective equilibrium simulated by a cloud-resolving model, *J. Adv. Model. Earth Syst.*, 5, 816825, doi:10.1002/2013MS000253.

Khairoutdinov, M., and D. Randall (2003), Cloud resolving modeling of the ARM summer 1997 IOP: Model formulation, results, uncertainties, and sensitivities, *J. Atmos. Sci.*, 60, 607-625.

Larson, K., D. L. Hartmann, and S. A. Klein (1999), The role of clouds, water vapor, circulation, and boundary layer structure in the sensitivity of the tropical climate, *J. Climate*, 12(8), 2359-2374.

Lin, B., B. A. Wielicki, L. H. Chambers, Y. Hu, and K.-M. Xu (2001), The Iris hypothesis: A negative or positive cloud feedback? *J. Climate*, 15, 37.

Lindzen, R., M.-D. Chou, and A. Hou (2001), Does the earth have an adaptive infrared iris? *Bull. Amer. Meteor. Soc.*, 82, 4174-32.

Madden, R., and P. Julian (1971), Detection of a 40-50 day oscillation in the zonal wind in the tropical pacific, *J. Atmos. Sci.*, 28, 702-708.

Manabe, S., and R. F. Strickler (1964), Thermal equilibrium of the atmosphere with a convective adjustment. *J. Atmos. Sci.*, 21, 361-385.

Manabe S. and Wetherald, R. T. (1976), Thermal equilibrium of the atmosphere with a given distribution of relative humidity. *J. Atmos. Sci.*, 24,241-259

Matsuno, T. (1966), Quasi-geostrophic motion in the equatorial area. *J. Meteor. Soc. Japan*, 44, 2543.

Mlawer, E. J., S. J. Taubman, P. D. Brown, M. J. Iacono, and S. A. Clough (1997), Radiative transfer for inhomogeneous atmospheres: RRTM, a validated correlated-k model for the longwave, *J. Geophys. Res.*, 102(D14), 16663-16682, doi:10.1029/97JD00237.

Muller, C. J., and I. M. Held (2012), Detailed investigation of the convective aggregation of convection in cloud-resolving simulations, *J. Atmos. Sci.*, 69(8), 2551-2565, doi:10.1175/JAS-D-11-0257.1.

Muller, C., and S. Bony (2015), What favors convective aggregation and why?, *Geophys. Res. Lett.*, 42, 5626-5634, doi:10.1002/2015GL064260.

Naegel, A. (2016), Observations and simulations of the interactions between clouds, radiation, and precipitation. M.S. Thesis, Colorado State University, 88 pp.

Nakazawa T., (1988), Tropical super clusters within intraseasonal variations over the western Pacific. *J. Meteor. Soc. Japan*, 66, 823-839.

Neelin, J. D., and I. M. Held (1987), Modeling tropical convergence based on the moist static energy budget. *Mon. Wea. Rev.*, 115, 312, doi: 10.1175/1520-0493.

Nilsson J, Emanuel K. (1998), Equilibrium atmospheres of a two-column radiative-convective model. *Quart. J. R. Meteorol. Soc.* 125: 2239-2264.

Nolan, D., E. Rappin, and K. Emanuel (2007), Tropical cyclonegenesis sensitivity to environmental parameters in radiative-convective equilibrium, *Q. J. R. Meteorol. Soc.*, 133, 2085-2107.

Pierrehumbert, R. T. (1995), Thermostats, radiator fins and the local runaway greenhouse. *J. Atmos. Sci.*, 52, 1784-1806.

Posselt, D. J., S. C. van den Heever, and G. L. Stephens (2008), Trimodal cloudiness and tropical stable layers in simulations of radiative convective equilibrium. *Geophys. Res. Lett.*, 35, L08802, doi:10.1029/2007GL033029.

Pielke, R. A., et al. (1992), A comprehensive meteorological modeling system-RAMS, *Meteorol. Atmos. Phys.*, 49, 69-91.

Raymond D. (2000), The Hadley circulation as a radiative-convective instability. *J. Atmos. Sci.* 57: 1286-1297.

Raymond, D. J., and X. Zeng (2000), Instability and large-scale circulations in a two-column model of the tropical troposphere. *Quart. J. Roy. Meteor. Soc.*, 126, 3117-3135.

Renno, N. O. (1997), Multiple equilibria in radiative-convective atmospheres. *Tellus A*, 49: 423-438. doi:10.1034/j.1600-0870.1997.t01-3-00002.x

Reed, K. A., B. Medeiros, J. T. Bacmeister, and P. H. Lauritzen (2015), Global radiative-convective equilibrium in the Community Atmosphere Model, version 5, *J. Atmos. Sci.*, 72(5), 2183-2197, doi:10.1175/JAS-D-14-0268.1.

Riehl, H., J. S. Malkus (1958), On the heat balance in the equatorial trough zone. *Geophysica*, 6, 503-538.

Schneider, S. (1972), Cloudiness as a global climatic feedback mechanism: The effects on radiation balance and surface temperatures of variations in cloudiness. *J. Atmos. Sci.*, 29, 1413-1422.

Sherwood, S. C., S. Bony, and J. L. Dufresne (2014), Spread in model climate sensitivity traced to atmospheric convective mixing, *Nature*, 505(7481), 37-42, doi:10.1038/nature12829.

Silvers, L. G., M. Giorgetta, T. Mauritsen, and B. Stevens (2016), Radiative convective equilibrium as a framework for understanding the interaction between convection and its large-scale environment, *J. Adv. Model. Earth Syst.*, doi:10.1002/2016MS000629

Stephens, G. L., S. van den Heever, and L. Pakula (2008), Radiative-convective feedbacks in idealized states of radiative-convective equilibrium. *J. Atmos. Sci.*, 65, 3899-3916

Stone, P. H., and J. H. Carlson (1979), Atmospheric lapse rate regimes and their parameterization. *J. Atmos. Sci.*, 36, 4154-23.

Su, H., C. S. Bretherton, and S. S. Chen (2000), Convective aggregation and large-scale control of tropical deep convection: A modeling study. *J. Atmos. Sci.*, 57, 1797-1816.

Tobin, I., S. Bony, and R. Roca (2012), Observational evidence for relationships between the degree of aggregation of deep convection, water vapor, surface fluxes, and radiation, *J. Clim.*, 25, 6885-6904.

Tompkins, A. M., and G. C. Craig (1998), Radiative-convective equilibrium in a three-dimensional cloud-ensemble model, *Q. J. R. Meteorol. Soc.*, 124(550), 2073-2097, doi:10.1002/qj.49712455013.

Tompkins, A. M. (2000) On the relationship between tropical convection and SST. *J. Climate*, 14, 6336-637.

Tompkins, A. M. (2001), Organization of tropical convection in low vertical wind shears: The role of water vapor. *J. Atmos. Sci.*, 58, 529-545.

Webster, P. J., R. Lukas (1992), TOGA COARE: The Coupled Ocean-Atmosphere Response Experiment, *Bull. Am. Meteor. Soc.*, 73, 1377-1416, 1992.

Wheeler, M., and G. N. Kiladis (1999), Convectively coupled equatorial waves: Analysis of clouds and temperature in the wavenumber-frequency domain. *J. Atmos. Sci.*, 56, 374-399.

Wing, A. A., and K. A. Emanuel (2013), Physical mechanisms controlling convective aggregation of convection in idealized numerical modeling simulations, *J. Adv. Model. Earth Syst.*, 6, 59-74, doi:10.1002/2013MS000269.

Wing, A. A., and T. W. Cronin (2015), convective aggregation of convection in long channel geometry, *Q. J. R. Meteorol. Soc.*, doi:10.1002/qj.2628.

Zhang, C. (2005), Madden-Julian Oscillation, *Rev. Geophys.*, 43, RG2003, doi:10.1029/2004RG000158.

## 10. APPENDIX

In the following, we show that the water budget is balanced in the simple model of the aggregated RCE state, i.e, that the total surface evaporation balances the total precipitation,  $E = \pi l_c^2 P$ , assuming that the mass budget is balanced.

First, recall that the total precipitation  $\pi l_c^2 P$  is given by:

$$\pi l_c^2 P = -\frac{\frac{\omega_c}{g} \pi l_c^2 (RH_c q_{sat} - q_{FA})}{1 - \alpha} \quad (129)$$

$$\pi l_c^2 P (1 - \alpha) = -\frac{\omega_c}{g} \pi l_c^2 (RH_c q_{sat} - q_{FA}) \quad (130)$$

$$\pi l_c^2 P = -\frac{\omega_c}{g} \pi l_c^2 (RH_c q_{sat} - q_{FA}) + \pi l_c^2 \alpha P \quad (131)$$

$$\pi l_c^2 P = P_0 + \pi l_c^2 \alpha P \quad (132)$$

Here,  $P_0 = -\frac{\omega_c}{g} \pi l_c^2 (q_{sat} - q_{FA})$ . Now, note that the total surface evaporation is:

$$E = \pi l_c^2 \alpha P + 2\pi \int_{l_c}^{l_d} (F_q)_s r dr \quad (133)$$

So that:

$$E - \pi l_c^2 P = 2\pi \int_{l_c}^{l_d} (F_q)_s r dr - P_0 \quad (134)$$

Therefore, we just need to show that  $P_0 = 2\pi \int_{l_c}^{l_d} (F_q)_s r dr = E_0$  in order to show that  $E = \pi l_c^2 P$ . We first substitute the turbulent flux of water vapor at the surface,  $(F_q)_s$ , using

the bulk-aerodynamic formula in (134):

$$E_0 = 2\pi \int_{l_c}^{l_d} (F_q)_s r dr = 2\pi \int_{l_c}^{l_d} \rho c_E |u_{BL}| (q_{sat} - q_{BL}) r dr \quad (135)$$

Using the expressions for  $u_{BL}$  and  $q_{BL}$ , (34) and (42), respectively, and  $\hat{z} = \frac{\delta p_{BL}}{c_E \rho g}$  yields:

$$E_0 = -\frac{\pi \rho c_E \omega_d}{\delta p_{BL}} \int_{l_c}^{l_d} 2\hat{z} (q_{FA} - q_{sat}) \left[ r + \hat{z} - (\hat{z} + l_d) e^{\frac{r-l_d}{\hat{z}}} \right] dr \quad (136)$$

$$= -\frac{2\pi \omega_d}{g} \int_{l_c}^{l_d} (q_{FA} - q_{sat}) \left[ r + \hat{z} - (\hat{z} + l_d) e^{\frac{r-l_d}{\hat{z}}} \right] dr \quad (137)$$

After integration, this becomes:

$$E_0 = -\frac{2\pi \omega_d}{g} (q_{FA} - q_{sat}) \left[ \frac{l_d^2 - l_c^2}{2} + \hat{z} (l_d - l_c) - \hat{z} (\hat{z} + l_d) (1 - e^{\frac{l_c - l_d}{\hat{z}}}) \right] \quad (138)$$

$$E_0 = \pi \frac{\omega_d (l_d^2 - l_c^2)}{g} (q_{sat} - q_{FA}) - \frac{2\pi \omega_d \hat{z}}{g} (q_{FA} - q_{sat}) \left[ (l_d - l_c) - (\hat{z} + l_d) (1 - e^{\frac{l_c - l_d}{\hat{z}}}) \right] \quad (139)$$

Now we manipulate  $P_0$  in order to show that it is equivalent to (139). Using the expression for conservation of mass, (49), and the expression for  $RH_c$ , (44) yields:

$$P_0 = -\pi \frac{\omega_c}{g} l_c^2 (RH_c q_{sat} - q_{FA}) \quad (140)$$

$$= \pi \frac{\omega_d (l_d^2 - l_c^2)}{g} \left[ q_{sat} - q_{FA} + \frac{2\hat{z} (q_{FA} - q_{sat})}{l_d^2 - l_c^2} \left[ l_c + \hat{z} - (\hat{z} + l_d) e^{\frac{l_c - l_d}{\hat{z}}} \right] \right] \quad (141)$$

$$= \pi \frac{\omega_d (l_d^2 - l_c^2)}{g} (q_{sat} - q_{FA}) - \frac{2\pi \hat{z} \omega_d}{g} (q_{FA} - q_{sat}) \left[ l_c + \hat{z} - (\hat{z} + l_d) e^{\frac{l_c - l_d}{\hat{z}}} \right] \quad (142)$$

Subtracting (142) from (139) yields:

$$E_0 - P_0 = \left[ (l_d - l_c) - (\hat{z} + l_d) (1 - e^{\frac{l_c - l_d}{\hat{z}}}) \right] + \left[ l_c + \hat{z} - (\hat{z} + l_d) e^{\frac{l_c - l_d}{\hat{z}}} \right] \quad (143)$$

Finally, simplifying (143) yields:

$$\begin{aligned}
 E_0 - P_0 &= \left[ (l_d - l_c - \hat{z} - l_d + (\hat{z} + l_d)e^{\frac{l_c - l_d}{\hat{z}}}} \right] + \left[ l_c + \hat{z} - (\hat{z} + l_d)e^{\frac{l_c - l_d}{\hat{z}}} \right] \\
 &= 0.
 \end{aligned}$$

$$\sigma = \frac{1}{1 - \frac{\hat{Q}_c}{\hat{Q}_d} \left( \frac{\Delta s_{trop}}{\Delta h_{trop,eff}} \right)} \quad (144)$$

$$\omega_c \Delta h_{trop} - g L_v \alpha P = g \hat{Q}_c \quad (145)$$

Therefore,  $E_0 = P_0$  and hence the total surface evaporation balances the total precipitation, i.e.,  $E = \pi l_c^2 P$ , assuming that the mass budget is balanced.